Complex systems methods for detecting dynamical anomalies in past climate variability

D I S S E R T A T I O N

zur Erlangung des akademischen Grades

d o c t o r r e r u m n a t u r a l i u m
(Dr. rer. nat.)
im Fach Physik
Spezialisierung: Theoretische Physik

eingereicht an der
Mathematisch-Naturwissenschaftlichen Fakultät
der Humboldt-Universität zu Berlin

von
Jaqueline Stefanie Lekscha, MSc.

Präsidentin der Humboldt-Universität zu Berlin:
Prof. Dr.-Ing. Dr. Sabine Kunst

Dekan der Mathematisch-Naturwissenschaftlichen Fakultät:
Prof. Dr. Elmar Kulke

Gutachter:

1. Prof. Dr. Dr. h.c. mult. Jürgen Kurths
2. Prof. Dr. Holger Lange
3. Prof. Dr. Martin Rypdal

Tag der mündlichen Prüfung: 10.01.2020

To my grandparents.
You will always be remembered.

Abstract

The climate system is a complex dynamical system exhibiting variability at many different spatial and temporal scales. Thus, to characterise its dynamics, methods from the fields of non-linear dynamics and complex system theory are required. With respect to the recent climate crisis and associated natural and societal impacts, the advancement of the understanding of the Earth's climate is of major importance. Studying palaeoclimate proxy data from archives such as tree rings, lake sediments, speleothems, and ice cores using windowed recurrence network analysis contributes to such an advancement as it offers the possibility to characterise dynamical anomalies in past climate variability.

The first step of windowed recurrence network analysis is the reconstruction of the system's phase space from the measured time series. This is particularly challenging when the available data are non-uniformly sampled and subject to noise. In a second step, the reconstructed higher-dimensional time series is split into windows and for each window, a recurrence network is constructed. The evolution of the system's dynamics is then characterised by network measures such as the network transitivity. Finally, a significance test is applied in order to define dynamical anomalies with respect to a specified null model. However, for windowed analyses, temporal correlations within the results may lead to increased numbers of false positive significant points.

In this thesis, we aim at developing a more reliable framework of windowed recurrence network analysis and windowed scale-specific recurrence network analysis. We identify phase space reconstruction and significance testing as parts of the analysis framework which can still be improved. Hence, in the first part of the thesis, we compare different phase space reconstruction approaches, namely, uniform time delay embedding and derivative embedding for three ways of estimating the derivatives, for non-uniformly sampled noisy data. Also, to tackle the problem of increased numbers of false positive significant points when correlations within the analysis results can not be neglected, we introduce a generalised areawise significance test. This test implements a numerical estimation of the correlations and can be used to identify patches of possibly false positive significant points.

In the second part of the thesis, we apply the developed analysis framework to detect and characterise dynamical anomalies in past climate variability in North and South America. To do so, we study four real-world time series from different archives and start exploring regional similarities and differences in the variability of the climate on both American continents in the last two millennia. We then systematically approach the question whether palaeoclimate proxy time series from different archives are equally well suited for tracking past climate dynamics with windowed recurrence network analysis. By processing different artificial input time series through four proxy system models and comparing the analysis results, we are able to quantify the correspondence between climate input and model output and associated implications for analysing data from the different archives.

With this thesis, we promote the use of non-linear methods for analysing palaeoclimate proxy time series and provide a detailed assessment of potentials and limitations of windowed recurrence network analysis. We also take a first

step towards systematically characterising non-linear climate variability in North and South America and identify future research directions that can complement the results and conclusions of the thesis.

Zusammenfassung

Das Klimasystem ist ein komplexes dynamisches System, das durch Variabilität auf verschiedensten räumlichen und zeitlichen Skalen gekennzeichnet ist und deshalb mit Methoden aus den Bereichen nichtlineare Dynamik und Theorie komplexer Systeme untersucht werden sollte. Angesichts der globalen Klimakrise und den damit verbundenen Folgen für Natur und Gesellschaft ist das Streben nach einem verbesserten Verständnis des Klimasystems dringend notwendig. Die Analyse von Proxy-Zeitreihen aus Paläoklimaarchiven wie zum Beispiel Baumringen, Seesedimenten, Tropfsteinen und Eisbohrkernen mittels gefensterter Rekurrenznetzwerkanalyse ermöglicht die Identifizierung und Charakterisierung dynamischer Anomalien in der Klimavariabilität der Vergangenheit.

Für die gefensterte Rekurrenznetzwerkanalyse muss zunächst der Phasenraum des untersuchten Systems aus der gemessenen Zeitreihe rekonstruiert werden, was insbesondere für unregelmäßig abgetastete und verrauschte Daten eine Herausforderung darstellt. Anschließend wird die eingebettete Zeitreihe stückweise in ein Rekurrenznetzwerk transformiert, dessen Struktur durch Netzwerkmaße wie die Transitivität charakterisiert werden kann. Die zeitliche Entwicklung der Netzwerkmaße lässt Einsichten in die Dynamik des betrachteten Systems zu. Zuletzt erfolgt ein Signifikanztest, der die erhaltenen Werte von denen eines geeigneten Nullmodells abgrenzt und damit dynamische Anomalien in den Daten identifiziert. Allerdings können gerade bei gefensterten Analysen zeitliche Korrelationen innerhalb der Analyseergebnisse zu vermehrten falsch positiven Ergebnissen führen.

Das Ziel der vorliegenden Arbeit ist die Entwicklung einer zuverlässigeren Routine zur gefensterten Rekurrenznetzwerkanalyse und zur gefensterten skalenspezifischen Rekurrenznetzwerkanalyse. Aufbauend auf dem bestehenden methodischen Rahmen identifizieren wir die Bereiche der Phasenraumrekonstruktion und des Signifikanztests als verbesserungsfähig. Deshalb werden im ersten Teil der Arbeit verschiedene Methoden zur Rekonstruktion des Phasenraums aus unregelmäßig abgetasteten, verrauschten Daten verglichen. Dabei betrachten wir insbesondere die Methode der uniformen Zeitverzögerungseinbettung und der differentiellen Einbettung für drei verschiedene Arten der numerischen Schätzung der Ableitungen. Außerdem führen wir einen allgemeinen flächenweisen Signifikanztest ein, der, basierend auf einem ausgewählten Nullmodell, Korrelationen in den Analyseergebnissen numerisch abschätzt, um damit das Problem hoher Raten an falsch positiv signifikanten Ergebnissen zu adressieren.

Im zweiten Teil der Arbeit nutzen wir die entwickelte Methodik, um die nichtlineare Variabilität des Klimas der Vergangenheit in Nord- und Südamerika zu untersuchen. Dazu studieren wir vier reale Zeitreihen verschiedener Proxys und arbeiten regionale Ähnlichkeiten und Unterschiede der Klimavariabilität der letzten zwei Jahrtausende auf den beiden amerikanischen Kontinenten heraus. Außerdem gehen wir auf die Frage der Eignung von Daten verschiedener Paläoklimaarchive zur Charakterisierung der Klimavariabilität mittels gefensterter Rekurrenznetzwerkanalyse ein. Dazu nutzen wir Proxy-System-Modelle und vergleichen die Analyseergebnisse verschiedener künstlich erzeugter Input- und entsprechender Modell-Output-Zeitreihen. Dies ermöglicht eine Bewertung der Stärken und Probleme der Analyse von Daten aus den verschiedenen Archiven.

Mit der Arbeit bringen wir den Einsatz nichtlinearer Methoden zur Analyse von Paläoklima-Zeitreihen voran und zeigen das Potential und die Grenzen der gefensterten Rekurrenznetzwerkanalyse auf. Neben einem ersten Schritt zu einer systematischeren Charakterisierung der Klimavariabilität in Nord- und Südamerika identifizieren wir auch zukünftige relevante Fragestellungen, die die Ergebnisse und Schlussfolgerungen dieser Arbeit komplementieren können.

List of publications

This dissertation is partly based on the following publications. The identifiers P1 - P3 are cited in the text to highlight passages that are connected to these papers. The dissertation partly uses passages from the papers that were written by the author of this thesis. All passages provided by the co-authors were thoroughly rewritten.

P1 **J. Lekscha** and R. V. Donner (2018). Phase space reconstruction for non-uniformly sampled noisy time series. Chaos 28, 085702. DOI: 10.1063/1.5023860.

P2 **J. Lekscha** and R. V. Donner (2019). Areawise significance tests for windowed recurrence network analysis. Proceedings of the Royal Society A 475. DOI: 10.1098/rspa.2019.0161.

P3 **J. Lekscha** and R. V. Donner (in review). Suitability of recurrence network analysis to detect dynamical anomalies in time series from different palaeoclimate proxy archives. Nonlinear Processes in Geophysics Discussion. DOI: 10.5194/npg-2019-41.

Berlin, January 10, 2020

Acknowledgements

First of all, I would like to express my deep gratitude to Prof. Jürgen Kurths who gave me the opportunity to do my PhD in such an inspiring working environment as the Potsdam Institute for Climate Impact Research (PIK). In this respect, a very special thanks also goes to my day-to-day supervisor Reik Donner who not only always supported me during my time at PIK but also left me the freedom to follow my own plans and ideas.

I thank my colleagues and friends at PIK with whom I had a great time during the last three and a half years – with and without cake. In particular, I thank Catrin, Reik, Jasper, Max, Forough, Catrin, Hauke, Christian, Anton, and Frederik for great discussions and for proofreading parts of my thesis. Your valuable comments helped a lot improving the manuscript! Thank you also to my other colleagues, especially Frank and Bedartha, for good collaborations. Additionally, I want to thank Gabi and Till for making my life at PIK so much easier by providing assistance in all organisational matters.

I am very grateful to *Studienstiftung des deutschen Volkes* and the CoSy-CC^2 junior research group led by Reik Donner for the financial support and for the great events that they enabled me to participate. Particularly the network provided by the *Studienstiftung* offered the opportunity to take part in many interesting discussions about diverse scientific, societal, and personal matters and to make new friends.

Last but not least, I thank my friends and my family, especially my parents and my brother, for their unconditional support in every respect and for always believing in me. Without you, I would never have made it.

Contents

List of Figures

List of Tables

List of frequently used abbreviations and mathematical symbols

Frequently used abbreviations

AR(1)	autoregressive process of order 1
dLp	discrete Legendre polynomials
GWN	Gaussian white noise
iAAFT	iterative amplitude-adjusted Fourier transform
LIA	Little Ice Age
LMR	last millennium reanalysis
MCA	Medieval Climate Anomaly
MoTaBaR	moving Taylor Bayesian regression
ODE	ordinary differential equation
tde	time delay embedding
wRNA	windowed recurrence network analysis
wssRNA	windowed scale-specific recurrence network analysis

Frequently used mathematical symbols

$\mathcal{L}$	average shortest path length
m	dimension of reconstructed phase space
RR	recurrence rate of a recurrence plot or network
s	scale
t	time
$\mathcal{T}$	network transitivity
τ	delay time for time delay embedding
W	window width of sliding window analyses

Chapter 1.

Introduction

The Earth's climate is a highly complex dynamical system driven by the latitudinally heterogeneous absorption of solar radiation (Lucarini et al., 2014; Hartmann, 2016). It exhibits both high-dimensional chaotic internal and forced external variability at many different spatial and temporal scales (Dijkstra, 2013; Bradley, 2015f). Studying past climate dynamics does not only advance our understanding of the climate system but also provides a historical context to recent climate change and associated future impacts (Crowley, 2000; Mann, 2007). Most notably, palaeoclimate data analysis enables the calibration and validation of general circulation models that are currently the basis of climate projections (Schneider and Mastrandrea, 2007). In this respect, using non-linear methods from the field of complex systems to explore palaeoclimate data from the last two millennia offers the possibility to gain further insight into past climate variability. Particularly regions such as South America which have been less intensively studied in reconstructions of past climate conditions require further attention.

1.1. Complex systems methods

Classifying and characterising the dynamics of complex systems is an important task of non-linear time series analysis with applications in various fields such as medicine, finance, and climate (Kantz and Schreiber, 2004; Abarbanel et al., 1993; Grassberger et al., 1991). In particular, the detection of dynamical anomalies offers the possibility to gain substantial insights into the dynamics of the underlying system (Kantz and Schreiber, 2004; Dijkstra, 2013).

The advance of this field started with the introduction of the concept of phase space reconstruction in the early 1980s allowing to infer information on the higher-dimensional dynamics of a system from a measured univariate time series (Takens, 1980; Packard et al., 1980; Bradley and Kantz, 2015). Since then, non-linear time series analysis has become a very active field of research and a multitude of sophisticated methods to characterise system dynamics has emerged (e. g. Kantz and Schreiber, 2004; Bradley and Kantz, 2015; Marwan et al., 2007; Zou et al., 2019). As increasing amounts of data are collected and stored, processing and categorising big data sets has become an important task in time series analysis and linear and non-linear machine learning algorithms have been developed for this purpose (Hastie et al., 2001; Jaeger and Haas, 2004; Alpaydin, 2014; Pathak et al., 2017). However, the problem of how

to optimally deal with short, non-uniformly sampled, or noisy time series is an equally important problem that also received considerable attention (Broomhead and King, 1986; Rehfeld et al., 2011; Jacob et al., 2016; Lange et al., 2018).

This problem is especially relevant in the context of palaeoclimate data analysis. There, recurrence based methods and complex networks have been proven, among many others, to be valuable tools (Eckmann et al., 1987; Marwan et al., 2007; Newman, 2003; Gao et al., 2016). Also their combination with a sliding window approach, windowed recurrence network analysis (wRNA), has been used to gain insights into past climate variability (Donges et al., 2011a; Donges et al., 2015a; Eroglu et al., 2018). In particular, this latter framework is able to deal with relatively short time series and provides an analytical relationship between the analysis results and the dimensionality of the system's dynamics (Marwan et al., 2009; Donner et al., 2011b; Zou et al., 2019).

Despite much research, there is still room for improvement when handling such imperfect data, in particular, the problem of phase space reconstruction has not yet been solved satisfactorily. Also, due to the complexity of the developed methods, objective criteria for choosing the analysis parameters, the introduction of robustness tests, and the improvement of significance tests are required. The latter is especially important when dealing with sliding window approaches. Due to the possible overlap of the windows, temporal correlations between the analysis results may lead to sequences of significant points instead of isolated significant points independent of whether those points are true or false positives (Maraun et al., 2007). The resulting increased numbers of significant points need to be corrected for in order to reliably interpret the obtained results.

1.2. Past climate variability

Systematic climate records are only available for a very limited time span as compared to the Earth's history (Bradley, 2015a). Hence, information on past climate conditions have to be inferred indirectly by studying palaeoclimate proxy archives such as tree rings, lake sediments, speleothems, or ice cores. Much work has been dedicated to relate measured proxy variables from the archives to climate variables (Bradley, 2015f). Depending on the location, tree ring width for example has been found to respond to temperature or moisture availability via the principle of limiting factors (Fritts, 1976) and serves as a good proxy for studying the recent past (St. George, 2014; St. George and Esper, 2019). Lake sediments offer a variety of proxy variables reflecting changes in air temperatures or precipitation via complicated processes within the lake and its basin (Cohen, 2003). Isotope fractions in speleothems can, for example, be used to infer information on hydrologic changes (Wong and Breecker, 2015; Lechleitner et al., 2018), while isotope fractions from polar and tropical ice cores have already provided insights into variations of temperature over many different time scales (Jouzel, 2013; Thompson et al., 2013).

Of course, the relations between proxies and climate variables are simplifications of the complex processes within the archives. However, due to a growing understanding of those processes, more proxy variables are developed and their interpretation is improved. Still, this interpretation often remains difficult and debated (Bradley, 2015f). Relations to past temperature or precipitation amounts are often inferred by defining transfer functions between the proxy variable and the climate variable based on modern instrumental data. These transfer functions assume a stationary relationship between the proxy and the climate variable which can generally not be guaranteed and is often even unlikely (Bradley, 2015a). Thus, applying the dynamical systems perspective in form of non-linear time series analysis to such proxy data offers complementary insights to reconstructions of past climate conditions.

1.3. Content and structure of the thesis

In this thesis, we aim at promoting the use of complex systems methods for studying past climate variability. In particular, we focus on wRNA as a tool to detect and characterise dynamical anomalies in time series from different palaeoclimate proxies. Windowed recurrence network analysis relies on the concept of recurrences in the phase space of a dynamical system, a very fundamental physical concept (Poincaré, 1890). In a first step, the phase space has to be reconstructed from a measured time series. The resulting higher-dimensional time series is divided into several possibly overlapping windows. For each window, the time series is transformed into a recurrence network which is then characterised by network measures such as the network transitivity. The relation of the network measures to the dynamics of the underlying system is used to study the evolution of the system's dynamics (Donner et al., 2011b). Dynamical anomalies are defined by applying a significance test which relates the results to those obtained from a suitable null model.

The thesis is divided into two parts. In the first part, we adapt and extent the framework of wRNA in order to improve its reliability. In the second part, we assess the potentials and limitations of wRNA for inferring information on past climate variability from time series of different palaeoclimate archives with a particular focus on North and South America and the last two millennia.

To be precise, in the first part of the thesis, we start by introducing the theoretical foundations required for further developing the analysis framework of wRNA in chapter 2. This particularly concerns the concepts of phase space reconstruction, recurrence plots, complex networks, recurrence networks, scale-specific recurrence networks, and significance testing. Then, in chapter 3, we contribute to a better understanding of the role that phase space reconstruction plays for the framework by comparing the performance of different phase space reconstruction approaches for non-uniformly sampled and noisy data. In chapter 4, we introduce a generalised areawise significance test that complements a classical pointwise significance when intrinsic correlations between the analysis results lead to patches of false positive points. Chapter 5 summarises the developed analysis framework.

In the second part of the thesis, we apply the framework of wRNA in order to start exploring past climate variability on both American continents. For this, in chapter 6, we analyse four real-world data sets from different palaeoclimate proxies and compare non-linear dynamical anomalies in past climate variability in North and South America. In chapter 7, we then systematically study how well time series from different palaeoclimate archives reflect dynamical anomalies in past climate variability. For this, we employ proxy system models and compare the results of wRNA for model in- and output of different artificial climate input time series with well-known properties. The insight from the second part are summarised in chapter 8.

Finally, in chapter 9, we present the main conclusions and contributions of this thesis and provide an outlook into future research that could be of particular interest for complementing the results obtained in this thesis.

Part I.

Development of analysis framework

The first part of the thesis deals with the development of an analysis framework of windowed recurrence network analysis and windowed scale-specific recurrence network analysis. In chapter 3, building on the theoretical foundations presented in chapter 2, we study the potentials and limitations of phase space reconstruction for non-uniformly sampled noisy time series by comparing derivative embedding to uniform time delay embedding. Then, a generalised areawise significance test is introduced and applied in combination with windowed recurrence network analysis and windowed scale-specific recurrence network analysis in chapter 4. Finally, we summarise the results and provide an overview over the developed analysis framework in chapter 5. This framework is used in the second part of the thesis to characterise dynamical anomalies in palaeoclimate time series, but it is equally well applicable to time series from many different areas.

Chapter 2.

Theoretical foundations

In this chapter, we present the theory relevant for the analysis framework by reviewing and discussing existing concepts of non-linear time series analysis. We particularly focus on reconstructing the higher-dimensional phase space of a system from a univariate measured time series, recurrence network analysis, and significance testing using surrogate data. These concepts are further developed and analysed in the following chapters of this first part of the thesis.

2.1. Non-linear time series analysis

The analysis of observed data plays an important role in many fields of science such as medicine, economics, and earth system analysis (Schreiber, 1999). Usually, the aim is to extract physically meaningful information from the data and, if possible, to classify it with respect to a suitable reference data set. In this context, the concept of system invariants has proven to be particularly useful (Abarbanel et al., 1993). System invariants are properties of the system that are independent of the exact initial conditions and the resolution of the available data.

Traditional methods of time series analysis mostly comprise linear methods with focus on estimating the autocorrelation, or equivalently, the power spectral density of the data (Kantz and Schreiber, 2004). For example, the identification of resonant frequencies in the power spectrum is used for system classification as those frequencies are linear system invariants. However, this set of techniques cannot be used to reliably distinguish deterministic chaotic dynamics from stochastic processes. Thus, in many applications, more sophisticated methods are required. The development of such methods started in the 1980s when there was increased interest in studying and characterising phenomena that exhibit dissipative chaotic dynamics such as turbulence in fluid mechanics (Eckmann and Ruelle, 1985). Assuming that the underlying dynamical system can generally be described by a set of ordinary or partial differential equations, non-linear approaches to estimate system invariants such as generalised fractal dimensions, Lyapunov exponents, or entropies from observed, often univariate time series became increasingly available and popular (Bradley and Kantz, 2015).

The basis for estimating these system invariants is the reconstruction of the higher-dimensional phase space of the underlying dynamical system from the measured, univariate time series. Packard et al. and Takens introduced time delay embedding

and derivative embedding to achieve this task (Packard et al., 1980; Takens, 1980). In section 2.3, we give a detailed review of the theory behind phase space reconstruction with a particular focus on practical implications of the available approaches.

After having obtained the reconstructed higher-dimensional time series representing the system dynamics, the density of points in the phase space can be used to estimate system invariants (Abarbanel et al., 1993). Commonly considered system invariants for detecting and characterising chaos are dimension estimates (Farmer et al., 1983). In this context, generalised dimensions D_q, with q being an integer, are particularly often studied. D_0, for example, is called the box-counting dimension and gives an estimate of the volume that the attractor fills in phase space, D_1 is the information dimension that takes into account the scaling of the information with the box-size, and D_2 is the correlation dimension which depends on the probability of two points being in the same part of the phase space (Grassberger, 1983; Hentschel and Procaccia, 1983).

As the generalised dimensions characterise the system attractor without taking into account time information, studying system invariants that characterise the dynamic evolution of the system gives complementary information. In this respect, global Lyapunov exponents which measure the exponential divergence of trajectories in each dimension of the phase space are used most prominently (Abarbanel et al., 1993; Kantz and Schreiber, 2004). This exponential divergence is characteristic for chaotic systems and closely related to the unpredictability of the future evolution of a chaotic system. This, in turn, can be viewed as information loss and thus expressed in terms of information theoretic measures such as entropies, in particular, the Kolmogorov-Sinai entropy (Pesin, 1977).

More recently, network based approaches of time series analysis such as recurrence network analysis, which combines the concept of recurrence plots (Eckmann et al., 1987) with the theory of complex networks (Newman, 2010), have gained increasing interest and have been successfully used to classify system dynamics (Marwan et al., 2009; Donner et al., 2010b). In particular, the network transitivity has been shown to correspond to a generalised notion of a fractal dimension (Donner et al., 2011b). In section 2.4, we provide a detailed introduction into recurrence network analysis.

Significance tests are, independent of the applied method, an important part of time series analysis especially relevant for interpreting the obtained results. A common approach to infer significance is to choose a null model and create surrogate data in accordance with it. Confidence bounds on the analysis results can then be obtained by analysing the surrogate data sets with the same method as the original data (Schreiber and Schmitz, 2000). Section 2.6 is concerned with the approach of significance testing using surrogate data.

There are many more interesting aspects of non-linear time series analysis such as prediction and causality inference from observed data that cannot be covered within the scope of the thesis. For the same reason, detailed description and mathematical definitions of topics and quantities not directly related to this thesis are omitted. Extensive reviews on non-linear time series analysis techniques and their implementations can, among others, be found in Eckmann and Ruelle (1985), Grassberger

et al. (1991), Abarbanel et al. (1993), Abarbanel (1996a), Schreiber (1999), Kantz and Schreiber (2004), and Bradley and Kantz (2015).

2.2. Model systems

Before going into the details of phase space reconstruction, recurrence network analysis, and significance testing, we here present two paradigmatic model systems, the Lorenz and the Rössler system, that will be used throughout the first part of the thesis in order to test and illustrate the application of the developed methods.

2.2.1. Lorenz system

In 1963, Lorenz presented a set of deterministic ordinary differential equations (ODEs) for finite systems to idealise forced dissipative hydrodynamic systems (Lorenz, 1963)

$$\begin{aligned}\dot{x}(t) &= a_L(y(t) - x(t)) \\ \dot{y}(t) &= x(t)(b_L - z(t)) - y(t) \\ \dot{z}(t) &= x(t)y(t) - c_L z(t).\end{aligned} \tag{2.1}$$

This set of ODEs is a truncated version of the equations presented by Saltzman used to study finite amplitude convection (Saltzman, 1962). The x-component is proportional to the intensity of the convective motion, the y-component measures the horizontal temperature variation, and the z-component is proportional to the distortion of the vertical temperature profile (Sparrow, 1982). The model parameters, a_L, b_L, and c_L, are dependent on the ratio between thermal and viscous convection, the ratio between the Rayleigh number and the critical Rayleigh number, and the scale of the convective cell, respectively (Abarbanel et al., 1993). There are two non-linearities present in the equations. The system has a steady-state solution at $x = y = z = 0$ corresponding to a state of no convection. The criterion for the onset of convection is given as $b_L \geq 1$, then, two additional steady-state solutions exist. For $a_L < c_L + 1$, the steady convection is always stable, while for $a_L > c_L + 1$, the steady convection is unstable for sufficiently high Rayleigh numbers.

Lorenz studied the system for $a_L = 10$, $b_L = 28$, and $c_L = 8/3$ with initial conditions $(x_0, y_0, z_0) = (0, 1, 0)$. Figure 2.1 displays the attractor for this set of parameters showing the typical butterfly-like structure. The point of no convection lies at $(0, 0, 0)$ and the two points of steady convection are at $(\pm 6\sqrt{2}, \pm 6\sqrt{2}, 27)$. This model has been found to describe, for example, irregular spiking behaviour of laser systems (Rössler, 1976) and certain aspects of chemical reactions (Poland, 1993).

2.2.2. Rössler system

As the qualitative behaviour of the dynamics of the Lorenz system is hard to capture, in 1976, Rössler introduced a simpler set of deterministic ODEs exhibiting similar

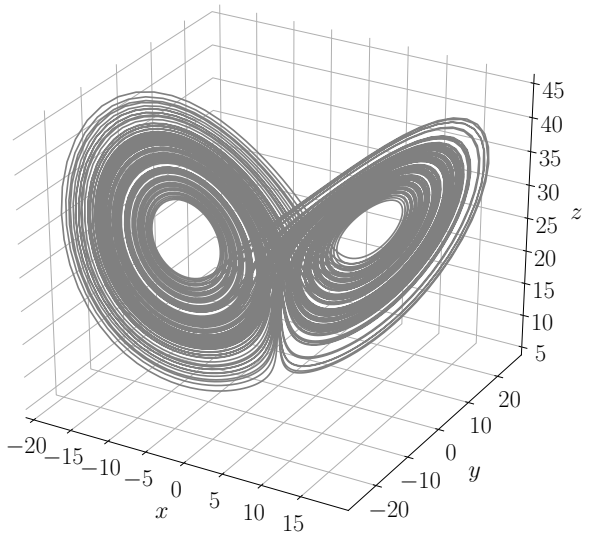

Figure 2.1.: Attractor of the Lorenz system with parameter choices and initial conditions corresponding to those used in Lorenz (1963) (see text).

dynamics to the Lorenz system (Rössler, 1976)

$$\begin{aligned}\dot{x}(t) &= -y(t) - z(t)\\ \dot{y}(t) &= x(t) + a_R y(t)\\ \dot{z}(t) &= b_R + z(t)(x(t) - c_R).\end{aligned} \tag{2.2}$$

He studied the behaviour of the system using $a_R = 0.2$, $b_R = 0.2$, and $c_R = 5.7$ as values of the parameters and initial conditions $(x_0, y_0, z_0) = (0, -6.78, 0.02)$. This system has only one non-linearity and exhibits a single spiral as visualised in figure 2.2. It can be seen as a two-dimensional oscillator (x, y) combined with a switching-type subsystem (z) and corresponds to a three-dimensional example of a horseshoe map (Rössler, 1976). As it follows a general principle of spiral-type chaos, it has applications in many fields, such as astrophysics, chemistry, biology, and economy (Rössler, 1976).

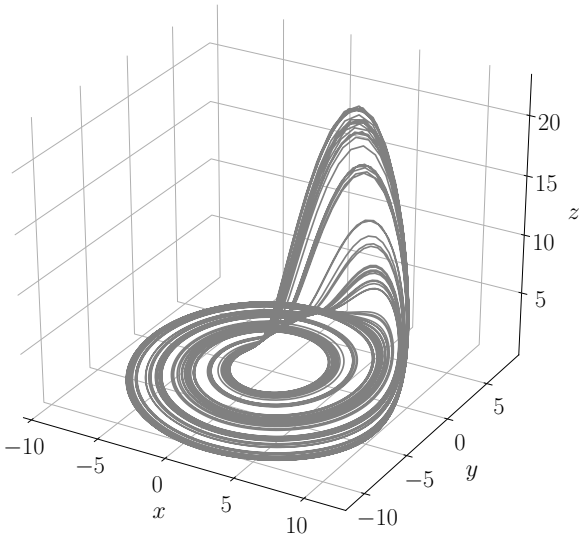

Figure 2.2.: Attractor of the Rössler system with parameter choices and initial conditions corresponding to those used in Rössler (1976) (see text).

2.3. Phase space reconstruction

We now turn to the problem of reconstructing the phase space of a dynamical system from experimentally measured, usually univariate, data on which most of the non-linear methods mentioned in section 2.1 rely. In theory, delayed versions of the measured time series or its derivatives can be used to obtain an attractor in the reconstructed phase space that is topologically equivalent to the attractor in the original system's phase space if the dimension of the reconstructed phase space is high enough (Takens, 1980; Packard et al., 1980). In the following, we review the theory behind the embedding theorems and particularly focus on the challenges that occur when trying to reconstruct the phase space of dynamical systems for non-perfect data, i. e., if the available data set is finite, has finite resolution, is contaminated with noise, and is possibly also non-uniformly sampled.

2.3.1. Embedding theorems

We consider a dynamical system $\vec{s}(t)$ in $\mathbb{R}^d$ whose time evolution is denoted by $\phi_T(\cdot)$. That is, the evolution from time t_0 to time $t_0 + T$ reads $\vec{s}(t_0 + T) = \phi_T(\vec{s}(t_0))$. The aim is to characterise dynamical properties of this system when only a univariate measured time series $x(t) = g(\vec{s}(t))$ is available and both $\phi_T(\cdot)$ and the measurement function $g(\cdot)$ that maps the points from $\vec{s}(t)$ to the univariate time series $x(t)$ are unknown.

Hence, we want to find a map $\Phi : \mathbb{R}^1 \to \mathbb{R}^m$ from the one-dimensional measured time series to an m-dimensional space such that the reconstructed m-dimensional system is an embedding of the original d-dimensional system. If Φ is an embedding,

this means that the dynamics of the embedded system are smooth and equivalent to the dynamics of the original system. This also implies that there is a smooth one-to-one coordinate transform with a smooth inverse between the two systems and thus, that $\vec{s}(t)$ and $\Phi(x(t))$ are diffeomorphic. In other words, the surface of the map Φ must not contain self-intersections such that mappings are unique and the dependence on the obtained states is smooth.

Building on the Whitney embedding theorem which states that $2D_0 + 1$ independently measured quantities form an embedding (Whitney, 1936), Takens proved that for a univariate, infinite set of noise-free, uniformly sampled data with infinite precision, the time delay map

$$\Phi_{\text{tde}} : x(t) \to \vec{x}(t) = \{x(t), x(t-\tau), \ldots, x(t-(m-1)\tau)\} \tag{2.3}$$

and the derivative map

$$\Phi_{\text{de}} : x(t) \to \vec{x}(t) = \left\{ x(t), \frac{dx(t)}{dt}, \ldots, \frac{d^{m-1}x(t)}{dt^{m-1}} \right\}. \tag{2.4}$$

are embeddings under generic conditions if the dimension m of the reconstructed space obeys the relation $m \geq 2D_0 + 1$ with D_0 being the box-counting dimension of the system (Takens, 1980). That is, when studying the system dynamics by using time delay embedding or derivative embedding of a univariate time series, it is possible to characterise the dynamical invariants of the original system. From an intuitive point of view, this can be understood by recalling that for non-linear systems, all variables are generically connected such that every variable contains information about the whole system and no disconnected subspace of the system dynamics can develop when applying a smooth coordinate transform (Abarbanel, 1996b).

Embeddings were also studied by Mañé (Mañé, 1981) and the embedding theorems were further developed by Sauer et al. (Sauer et al., 1991). Additionally, theorems for non-uniformly sampled time series have been developed assuming that the sampling generating function is dependent on the system's state (Sauer, 1994; Sauer, 1995; Huke and Broomhead, 2007). We will not go into the details here, instead, we will focus on how to perform phase space reconstructions in practice where most of the underlying assumptions of the Takens embedding theorem are not met.

2.3.2. Practical challenges

Any measured time series is subject to noise and has a finite amount of data with finite precision. In some cases, the sampling intervals are non-equal. Additionally, the box-counting dimension D_0 of the original system is generally not known and it can neither be verified whether the manifold of the original system is smooth nor whether the measurement function fulfils the required conditions (Bradley and Kantz, 2015).

This leads to the problem that not all phase space reconstructions as, for example, obtained by time delay embedding for varying delay times and embedding dimensions, or, by derivative embedding for various ways of estimating the derivatives, are actually

embeddings. That is, the choices of the embedding method and the corresponding embedding parameters play an important role for the equivalence between the original and the reconstructed phase space and, thus, for the further evaluation of the system's dynamical properties. In fact, for some data, a proper reconstruction of the system's phase space may not be possible (Casdagli et al., 1991).

The practical problem of phase space reconstruction is an active field of research and there is a large body of literature tackling the challenge of estimating embedding parameters from a measured time series. Accordingly, a plethora of more or less heuristic approaches to choose the embedding parameters is available. We here try to give an overview of the available methods without any claim to be complete and review those concepts that we think are most useful in some more detail. Still, we stress that there is most probably not one single optimal reconstruction of a system given a measured univariate time series as already argued in Grassberger et al. (1991).

Estimating the delay time

The choice of the delay time τ for time delay embedding has been studied extensively. The embedding theorems do not give any hints on how the delay time should be chosen as in theory, all values of τ, except for multiples of the system's periods for periodic systems, are equally well suited. This is because for infinitely long time series, any value of τ (except for multiples of the period of periodic systems) can resolve any system-inherent time scale (Sauer et al., 1991). In practice, the delay time τ should be chosen such that the resulting coordinates of the reconstructed higher-dimensional time series are as independent as possible but at the same time still contain relevant information (Abarbanel, 1996a). Choosing the delay time too small causes the different coordinates to be dependent such that the attractor stays closely to the identity line of the reconstructed space which is referred to as redundancy. On the other hand, choosing the delay too large introduces unnecessary randomness to the reconstructed attractor which has been termed irrelevance (Casdagli et al., 1991; Rosenstein et al., 1994).

To ensure independence of coordinates, various approaches have been put forward. The simplest is to choose the time delay corresponding to the first root of the autocorrelation function ac of the measured time series $x(t)$

$$ac(l) = \frac{\sum_{i=1}^{N-l} \left(x(t_i) - \langle x(t)\rangle\right)\left(x(t_{i+k}) - \langle x(t)\rangle\right)}{\sum_{i=1}^{N} \left(x(t_i) - \langle x(t)\rangle\right)^2} \tag{2.5}$$

where l is the time lag in multiples of the average sampling time $\langle dt\rangle$ and $\langle x(t)\rangle$ is the average value of x taken over the set of observations. This approach is often used due to its simplicity but legitimate critiques consist in recognising that this approach only ensures linear independence of subsequent coordinates in the reconstructed phase space. As it does not account for non-linear correlations and does not ensure that non-subsequent coordinates are independent, other approaches may be more appropriate (Casdagli et al., 1991).

Fraser and Swinney suggest to use the first minimum of the lagged average mutual information $I(x(t); x(t+l))$ as a criterion for general statistical independence of the coordinates (Fraser and Swinney, 1986). Assuming that $x(t)$ only takes discrete values x_j, $j = 1, \ldots, J$, and $x(t+l)$ only takes discrete values y_q, $q = 1, \ldots, Q$, the mutual information can be expressed as

$$I(x(t); x(t+l)) = \sum_{j=1}^{J} \sum_{q=1}^{Q} P(x_j, y_q) \log \left(\frac{P(x_j, y_q)}{P(x_j) P(y_q)} \right) \tag{2.6}$$

where $P(x, y)$ is the joint probability distribution of x and y and $P(x)$ denotes the marginal probability distribution of $P(x, y)$ with respect to x (Shannon and Weaver, 1949). In practice, the probability distributions can be estimated by binning the data and calculating histograms. The mutual information can be interpreted as the difference between the entropy of $x(t)$ and the conditional entropy of $x(t)$ after observing $x(t+l)$, that is, as the average information stored within $x(t)$ about $x(t+l)$. Theoretical justification why the first minimum of this quantity is appropriate for choosing the time delay of time delay embedding is provided by Liebert and Schuster (Liebert and Schuster, 1989). They also relate the mutual information to the correlation integral and so, provide an algorithm for easier evaluation of the criterion. Still, this approach only ensures independence between the first two coordinates of the reconstructed system and is thus only valid for two-dimensional reconstructions.

For higher-dimensional reconstructions, there is no a priori justification for using the same delay τ for all dimensions of the reconstruction. In fact, one can expect the delay times of the higher-dimensional coordinates to be smaller than the delays for the lower-dimensional coordinates, as, in this way, the different scaling regimes of the underlying dynamical system can be better reproduced (Grassberger et al., 1991). This is why Grassberger et al., among others, suggest to use non-uniform delay times τ_k for the different coordinates of the delay reconstruction (Grassberger et al., 1991). In particular, they suggest to use the mutual information conditioned on the already chosen coordinates to estimate the delays for the higher-dimensional coordinates of the reconstructed system. As the numerical estimation of high-dimensional histograms for the computation of the corresponding entropies is complex and susceptible to noise, the practical applicability of this approach has still to be evaluated.

For simplicity, in this thesis, we either use the first root of the autocorrelation function, equation (2.5), or the first minimum of the mutual information, equation (2.6), to estimate the delay time for uniform time delay embedding. Figure 2.3 shows the lagged autocorrelation function and the mutual information for the x- coordinate of the two model systems introduced in section 2.2 and corresponding choices of the model parameters. We observe that the results for the first root of the autocorrelation and the first minimum of the mutual information give very different results for the Lorenz system ($\tau = 675 \langle dt \rangle$ for the first root of the autocorrelation and $\tau = 16 \langle dt \rangle$ for the first minimum of the mutual information) which might be related to the two different time scales of the dynamics of this system (rotation within one wing

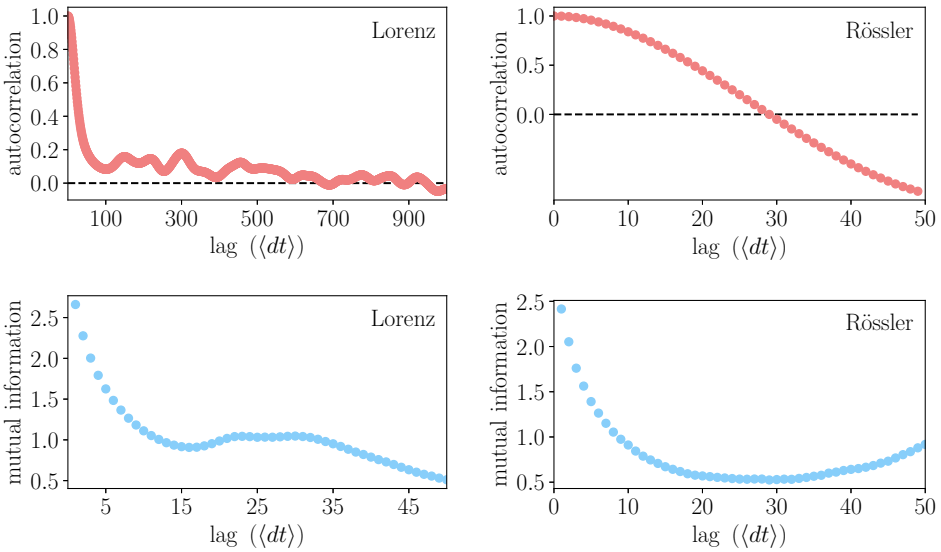

Figure 2.3.: Lagged autocorrelation function (top) and mutual information (bottom) for the Lorenz (left) and the Rössler (right) systems.

and switching between wings). For the Rössler system, the results agree for the two approaches of estimating the delay time ($\tau = 29\,\langle dt \rangle$). The average sampling times $\langle dt \rangle$ are in this case $\langle dt \rangle = 0.01$ for the Lorenz and $\langle dt \rangle = 0.05$ for the Rössler system.

Estimating the embedding dimension

In applications, the actual dimension of the underlying dynamical system is generally not known, thus, the estimation of the minimum required dimension to obtain an embedding is of great importance. When choosing the dimension too small, the attractor cannot unfold in the reconstructed space leading to spurious effects in the following analyses, while choosing the dimension too large causes many computations of dynamical invariants that scale with the dimension to become inefficient.

The most often studied and applied criterion to choose the embedding dimension is based on neighbourhood relations between points in reconstructed phase spaces of different dimensions. The method of false nearest neighbours was introduced by Kennel et al. and checks whether two points that are nearest neighbours in dimension m are still nearest neighbours in dimension $m + 1$ (Kennel et al., 1992). If this is not the case, the attractor has not fully unfolded in dimension m and the points are classified as false neighbours. As in higher dimensions, even nearest neighbours may be far apart, sets of nearest neighbours with a distance comparable to the attractor size (estimated, for example, as the standard deviation of the time series) are also counted as false neighbours. For noise-free conditions, the dimension in which the

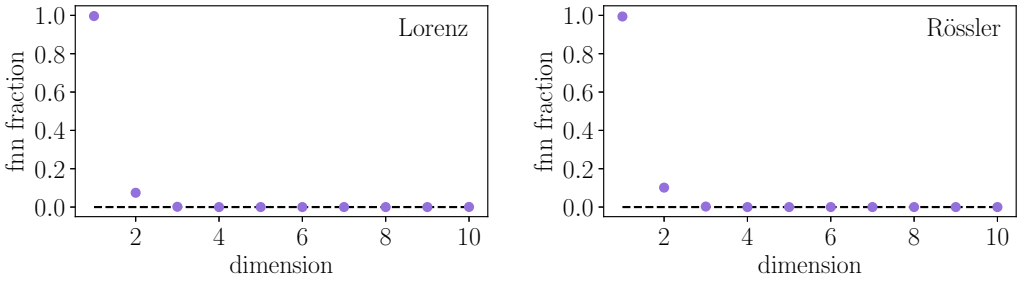

Figure 2.4.: Fraction of false nearest neighbours (fnn) for the Lorenz (left) and the Rössler (right) systems using the algorithm by Kennel et al. (1992) and correcting for autocorrelation effects (Fredkin and Rice, 1995).

fraction of false nearest neighbours goes to zero is used as estimate of the minimum required embedding dimension.

There are many corrections and adjustments for this approach trying to solve the problem of discriminating stochastic and chaotic signals, for example, by a probabilistic reformulation of the criterion and by surrogate data tests (Hegger and Kantz, 1999). Moreover, it has been noted that nearest neighbours due to temporal correlations should be excluded by introducing a temporal exclusion window and only taking points outside this window into account as potential candidates for nearest neighbours (Theiler, 1986; Fredkin and Rice, 1995). A similar reasoning is followed in the suggestion to rather identify false strands than false neighbours (Kennel and Abarbanel, 2002). Also, an approach that avoids the choice of parameters such as the thresholds for defining when a nearest neighbour counts as false neighbour has been put forward (Cao, 1997).

Figure 2.4 shows the fraction of false nearest neighbours for the two model systems calculated using the algorithm presented in Kennel et al. (1992) adjusted to correct for spurious autocorrelation effects within the time series by introducing a temporal exclusion window (Fredkin and Rice, 1995). According to this criterion, both the Lorenz and the Rössler system can be embedded in a three-dimensional space when using time delay embedding for delay times $\tau = 16\,\langle dt \rangle$ for the Lorenz and $\tau = 29\,\langle dt \rangle$ for the Rössler system.

Unified approaches

Another line of argument suggests that the choices of delay time and embedding dimension should not be considered as separate problems. Rather, the product $\tau(m-1)$ is assumed to play an important role for the quality of the reconstruction (Kugiumtzis, 1996). Many approaches that try to combine the estimation of the two parameters in a single procedure have been introduced and are particularly useful for choosing non-uniform delay times for the different coordinates.

A geometric approach that relies on neighbourhood relationships between inner and boundary points on the attractor in the reconstructed higher-dimensional phase space, the wavering product, is introduced in Liebert et al. (1991). Garcia and Almeida suggest to combine the method of false nearest neighbours with an adjusted version of the false nearest neighbour algorithm to iteratively determine the different delay times and the embedding dimension (Garcia and Almeida, 2005b). Other procedures rely on the fill factor and compare volumes and structures of parallelepipeds spanned by the reconstructed attractor for varying delay times and embedding dimensions or rely on the spreading of trajectories (Buzug and Pfister, 1992). Judd and Mees see the problem of finding a good reconstruction as a modelling problem and use the minimum description length principle to find global non-uniform time delay embeddings and local variable embeddings (Judd and Mees, 1998).

One approach to simultaneously estimate non-uniform delay times and the embedding dimension that we find particularly promising has been suggested by Pecora et al. and relies on a continuity statistic (Pecora et al., 2007). Based on the idea of independent coordinates, the authors test whether there is a continuous function that maps the already reconstructed coordinates to a potential additional coordinate associated with a certain delay time. Given the null hypothesis that there is no such function, a set of fiducial points is randomly drawn from the attractor in dimension m and the k nearest neighbours are determined. Then, the distances between the fiducial point and the k nearest neighbours are calculated in the one-dimensional space of the potential additional coordinate. The continuity statistics counts how many of the neighbours are closer than a threshold ϵ in this subspace. Using the binomial distribution, it is possible to derive the number of points l that have to be closer than ϵ for a given confidence level $1 - \alpha$ such that the null hypothesis can be rejected. ϵ is decreased until the null hypothesis can no longer be rejected and this procedure is repeated for various values of k. The minimum value of ϵ at which the null hypothesis can be rejected is then averaged over the different fiducial points. When calculating this average as a function of the delay time of the potential additional coordinate, the maxima of this function correspond to delays at which the potential additional coordinate is maximally independent of the previous m coordinates. When repeating this iteratively for the higher dimensions, a criterion for the minimum required embedding dimension is that the average value of ϵ stays low for all delays. Additionally, the authors suggest an undersampling statistic that can be used to check whether the continuity statistic can be reliably applied to the available data. Still, objective criteria for the choice of the exact maximum of the averaged ϵ that corresponds to the optimal delay time and for determining the minimum required embedding dimension are, to our knowledge, so far missing.

Derivative reconstructions

To avoid the problem of estimating the delay time for time delay embedding, an alternative approach for phase space reconstruction is to use derivative embedding. From a conceptual point of view, this approach seems to be more meaningfully related

to the underlying dynamics of the system which are assumed to be governed by a set of differential equations. Also, this approach can be seen as a linear transformation of time delay embedding with minimum delay. In practice, the problem is to robustly estimate the derivatives from the available data. In particular, for high dimensional reconstructions, noise amplification is a severe limitation of the approach (Mindlin and Gilmore, 1992).

Various approaches for derivative estimation in the context of phase space reconstruction have been suggested. They range from simple finite differences

$$\left.\frac{dx(t)}{dt}\right|_{t=t_i} \approx \frac{x(t_{i+1}) - x(t_i)}{dt} \tag{2.7}$$

to polynomial and fixed-interval Kalman filtering with possibly additional correction filters and some of them have been found to perform better in terms of time series forecasting than uniform time delay embedding (Xu et al., 2008).

Figure 2.5 displays three dimensional reconstructions from the x-component of the attractors of the two model systems for uniform time delay embedding with delay times $\tau = 16\,\langle dt \rangle$ for the Lorenz and $\tau = 29\,\langle dt \rangle$ for the Rössler system, corresponding to the first minima of the mutual information (compare figure 2.3), and using derivative embedding when estimating the derivatives with simple finite differences (equation (2.7)). We find that all reconstructions preserve the geometry of the original attractors (compare figures 2.1 and 2.2) and that, at least in this case of uniformly sampled noise-free data, derivative embedding is more powerful as it avoids the estimation of the delay time and, from a visual point of view, seems to reproduce the structure of the original attractor slightly better.

In chapter 3, we study different approaches for estimating the derivatives from non-uniformly sampled noisy time series and compare the results of the corresponding derivative reconstructions to those of uniform time delay reconstructions.

Other approaches

Besides time delay embedding and derivative embedding, various other approaches for phase space reconstruction have been suggested. One of them brought forward in order to deal with finite, noisy experimental data is that of singular spectrum analysis (Broomhead and King, 1986). In this approach, the embedded data are decomposed into orthonormal eigenvectors that span the reconstruction space. The dimensionality of this space is set by choosing only eigenvectors with sufficiently large eigenvalues. Still, the optimal delay time has to be estimated and also, there is generally no clear cut-off at which eigenvalues can be considered to be no longer relevant when studying strange attractors (Kugiumtzis, 1996). The relation between time delay embedding, derivative embedding, and singular spectrum analysis has been studied in detail and it has been found that the discrete Legendre polynomials bridge the methods of derivative embedding and singular spectrum analysis (Gibson et al., 1992).

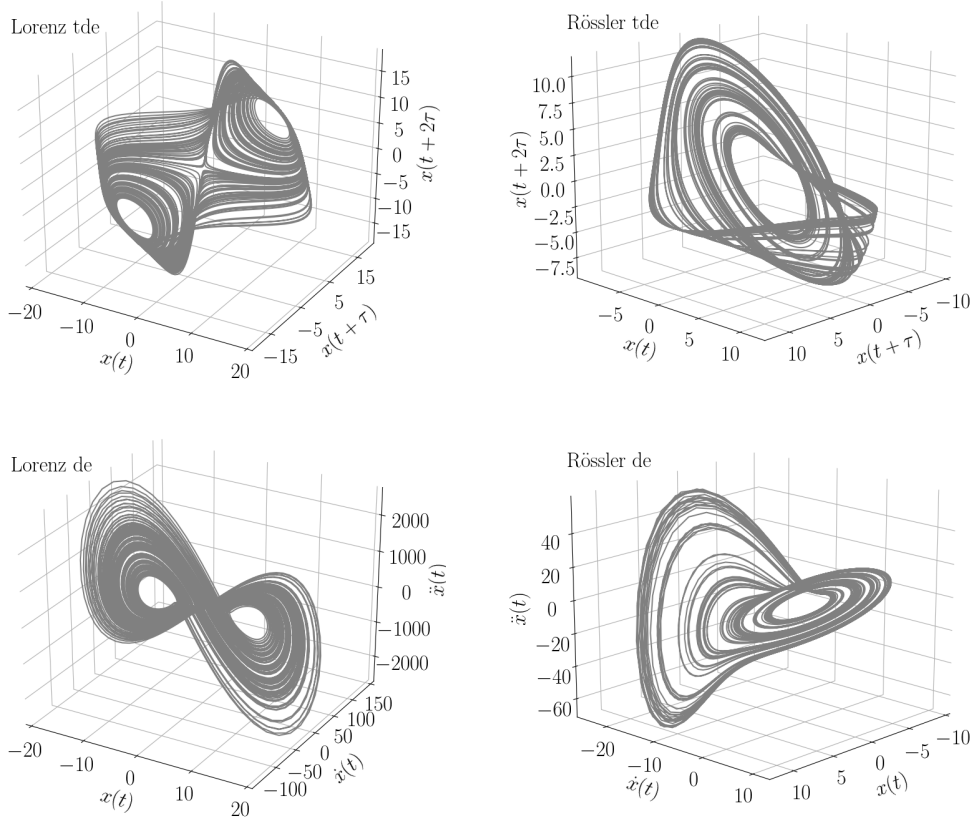

Figure 2.5.: Attractors reconstructed from the x-component of the Lorenz (left) and Rössler (right) systems for time delay embedding (tde) with the delay time estimated according to the first minimum of the mutual information (top) and for derivative embedding (de) using simple finite differences to estimate the derivatives (bottom).

A more systematic approach to study the influence of measurement noise on attractor reconstruction is pursued by Casdagli et al. (Casdagli et al., 1991). They note that opposed to the ideal case of perfect data, where a single original state is consistent with the measured state, in the case of noise, there are several original states consistent with the measured state. They derive a probability distribution for the original state given the measurements using Bayes' theorem. By judging the quality of the reconstruction based on the mean square error of the predictability, they find that coordinate transforms from the delay embedding to, e. g., singular spectrum reconstructions or derivative reconstructions cannot reduce the noise of the reconstruction but may be used to reduce the required dimension of the reconstruction. In particular, they find that non-linear coordinate transforms are preferred over linear ones and suggest a local singular value decomposition to provide the optimal coordinate transform for reducing the dimensionality of the system's reconstructed phase space.

To avoid the problem of determining the embedding dimension, an infinite dimensional time delay embedding was proposed by Hirata and Aihara that instead, introduces a scaling factor to weight the different dimensions (Hirata and Aihara, 2017). Huerter et al. perform local phase space reconstructions for sets of dimensions which can be useful for identifying lower-dimensional regions of a higher-dimensional system and thus, classifying its complexity (Huerta et al., 1995).

Recently, reservoir computing, a class of machine learning, has been shown to be useful for reproducing a system's attractor and calculating dynamical invariants such as Lyapunov exponents (Pathak et al., 2017). It has been argued that this setting can also be used for attractor reconstruction (Lu et al., 2018) but as training data of the high-dimensional reconstruction or the original system are required, this approach does not seem to be well suited when only a univariate measured time series is available.

Another interesting situation occurs when not only a single univariate time series is available, but a multivariate set of measurements can be assessed (Vlachos and Kugiumtzis, 2009). For this case, the term multivariate embedding has been coined and some of the presented approaches generalise to this situation, such as the ones presented in Garcia and Almeida (2005a) and Pecora et al. (2007).

The theory of observability offers an interesting perspective on phase space reconstruction. It has been found that the choice of the observable is related to the quality of the phase space reconstruction by linking the observability matrix of a system to the Jacobian which, in turn, can be seen as a map from the reconstructed to the original system (Aeyels, 1981; Letellier et al., 1998; Letellier et al., 2005; Aguirre and Letellier, 2005; Carroll, 2018). Thus, not every measured time series is equally suitable for performing a phase space reconstruction. Different measures for quantifying the observability of possibly univariate time series data have been developed and tested on various model systems (Aguirre et al., 2008; Aguirre and Letellier, 2011). For the Rössler system with parameters $(a_R, b_R, c_R) = (0.398, 2.0, 4.0)$, the y-coordinate has for example found to be slightly better suited for reconstruction with differential embedding than the x-coordinate, while an observability statistic employing time delay embedding ranks them equally well (Aguirre and Letellier, 2011). For the Lorenz

system with parameters as specified in section 2.2, the z-coordinate usually exhibits the best observability properties. However, this coordinate is not well suited for reconstructions as it can not resolve the symmetry of the attractor. Due to the local definition of the observability matrix, this problem is not taken into account by the observability statistic. The x- and y-coordinates show similar observability properties and, depending on the applied statistic, one or the other performs better (Aguirre et al., 2008).

Finally, we emphasise that most of the different approaches presented here require many possibly subjective parameter choices that critically determine whether the reconstructed system and the original system are diffeomorphic. Thus, to ensure qualitatively good phase space reconstructions, more research on objective criteria to determine reasonable ranges of the corresponding parameters given the measured data should, in our opinion, be conducted in the future.

2.4. Recurrence network analysis

In 1890, Henri Poincaré established recurrences as a fundamental property of dynamical systems (Poincaré, 1890). Based on this property, powerful tools to study the behaviour of a variety of dynamical systems have been developed (Marwan et al., 2007; Zou et al., 2019). Here, we introduce the framework of recurrence network analysis that has proven to constitute a versatile method of time series analysis by bringing together the concepts of recurrence plots and complex networks.

2.4.1. Recurrence plots

Recurrence plots were introduced by Eckmann et al. to obtain a graphical representation of the dynamics of a system (Eckmann et al., 1987). Given a time series $\vec{x}(t) = \{\vec{x}(t_i)\}_{i=1}^{N}$ for times t_i with $i \in [1, N]$ that represents the dynamics of an associated system in its original or reconstructed phase space, the recurrence matrix $\mathbf{R}$ is defined to have entries equal to one if two points $\vec{x}(t_i)$ and $\vec{x}(t_j)$ are recurrent, i. e., close in phase space, and zero otherwise. More formally, the entries are given as

$$R_{i,j}(\epsilon) = \theta\left(\epsilon - \|\vec{x}(t_i) - \vec{x}(t_j)\|\right) \tag{2.8}$$

with $\theta(\cdot)$ being the Heaviside function and ϵ being a threshold setting the maximum distance between two points to be considered recurrent. Distances in phase space are measured with respect to a norm $\|\cdot\|$ which can be, for example, the Euclidean, the Manhattan, or the maximum norm. By construction, this matrix is binary and symmetric.

The recurrence plot is the graphical visualisation of the recurrence matrix and can be obtained by plotting the ones as black dots on a white background. Exemplary recurrence plots for Gaussian white noise, the motion on a circle, the Lorenz, and the Rössler system are shown in figure 2.6.

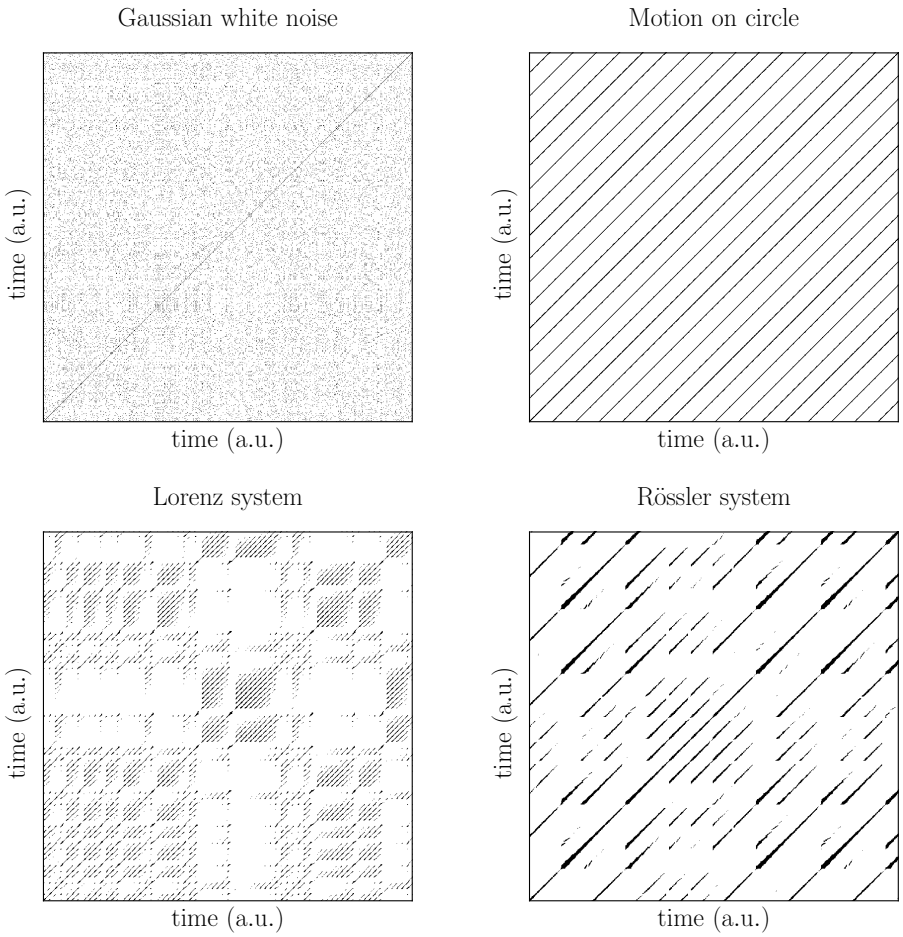

Figure 2.6.: Recurrence plots of Gaussian white noise, the motion on a circle, the Lorenz system, and the Rössler system for a fixed recurrence rate of $RR = 0.05$.

The line structure of the recurrence plot allows to deduce dynamical properties of the system under study. The length of sequences $\{(i, j), (i + 1, j + 1), \ldots, (i + k, j + k)\}$ (i. e., diagonal lines parallel to the main diagonal), for example, is inversely related to the largest Lyapunov exponent (Eckmann et al., 1987) as in this case, trajectories starting at i and j, respectively, stay close together for $k + 1$ time steps. Thus, long diagonal lines correspond to periodic dynamics with the period equalling the vertical distance between the lines, while short, interrupted diagonal lines indicate chaotic dynamics.

To objectively characterise the dynamics of a system from a recurrence plot, recurrence quantification analysis has been developed (Webber and Zbilut, 1994; Marwan et al., 2002) and applied in many contexts (e. g. Giuliani and Manetti, 1996; Marwan et al., 2002; Marwan et al., 2003; Lange and Boese, 2015; Flach et al., 2016). Based on the distribution of vertical and diagonal lines of different lengths, a set of complexity measures, such as for example the degree of determinism, the average diagonal line length, or the entropy, has been suggested. Notably, the recurrence rate, that is, the density of recurrent points, is closely related to the definition of the correlation sum that can be used to estimate the correlation dimension D_2 (Marwan et al., 2007). We will not go into the details of recurrence quantification analysis, a detailed review can be found, for example, in Marwan et al. (2007).

2.4.2. Complex networks

Complex networks have gained increasing attention as tools for non-linear time series analysis (Gao et al., 2016; Zou et al., 2019). Opposed to more classical network approaches that play important roles in many fields such as transportation, sociology, and ecology, complex networks in time series analysis represent dynamical statistical dependencies between observations expressed as functional networks. Thus, the theory of complex networks (see for example Albert and Barabási (2002), Newman (2003), and Newman (2010)) can be employed as tool for time series analysis.

Complex networks are graphs, that is, objects consisting of a set of vertices $\mathcal{V}$ and edges $\mathcal{E}$. Each vertex is labelled by an integer $i \in [1, N]$ and edges represent connections between pairs of vertices. A network is characterised by its adjacency matrix $\mathbf{A}$ where

$$A_{i,j} = \begin{cases} 1 & \text{if } i \text{ and } j \text{ are connected} \\ 0 & \text{otherwise.} \end{cases} \tag{2.9}$$

This form of a binary, symmetric adjacency matrix represents an unweighted, undirected network. If additionally, self-loops are not allowed (i. e., edges are only drawn for $i \neq j$), it is generally referred to as a simple graph. There are various extensions for weighted, directed networks, but in this thesis, we are only considering simple graphs.

From the adjacency matrix, it is possible to calculate different network measures that give information about local or global structural properties of the network. The most basic local network property is the degree k_i of a vertex i

$$k_i = \sum_{j=1}^{N} A_{i,j} \tag{2.10}$$

representing the number of neighbours of vertex i. The local clustering coefficient C_i of a vertex i

$$C_i = \frac{1}{k_i(k_i-1)} \sum_{j,k=1}^{N} A_{i,j}A_{j,k}A_{k,i} \tag{2.11}$$

indicates how many of the neighbours of this vertex are mutually connected compared to all possible mutual connections (Watts and Strogatz, 1998).

The edge density ρ is a global network measure given as the average of the normalised degrees of all vertices

$$\rho = \frac{1}{N(N-1)} \sum_{i,j=1}^{N} A_{i,j}. \tag{2.12}$$

Additionally, the degree distribution $p(k)$, containing information about the occurrences of vertices of specific degrees, is often used to classify networks. The global clustering coefficient $\mathcal{C}$ is defined as the average of the local clustering coefficients

$$\mathcal{C} = \frac{1}{N}\sum_{i=1}^{N} C_i = \frac{1}{N}\sum_{i=1}^{N} \frac{\sum_{j,k=1}^{N} A_{i,j}A_{j,k}A_{k,i}}{k_i(k_i-1)} \tag{2.13}$$

which can be interpreted as the mean per-node fraction of closed triangles in the network (Watts and Strogatz, 1998). A closely related quantity to estimate the fraction of triangles in a network is the network transitivity $\mathcal{T}$ given as (Barrat and Weigt, 2000; Newman, 2001; Boccaletti et al., 2006)

$$\mathcal{T} = \frac{\sum_{i,j,k} A_{i,j}A_{j,k}A_{k,i}}{\sum_{i,j,k} A_{i,j}A_{k,i}}. \tag{2.14}$$

The difference between the global clustering coefficient and the network transitivity is that using the global clustering coefficient corresponds to giving equal weight to all vertices in the network, thus, possibly underestimating the fraction of triangles when vertices with very high and very low connectivity are present within the network, while using the network transitivity corresponds to giving equal weight to all triangles in the network (Donner et al., 2011b).

Paths within the network consist of a sequence of edges that links two vertices i and j. When denoting the length of the shortest path between the two vertices as

$l_{i,j}$, we can compute the average shortest path length $\mathcal{L}$ as

$$\mathcal{L} = \frac{1}{N(N-1)} \sum_{i,j=1}^{N} l_{i,j}. \tag{2.15}$$

All those network measures have been used to classify networks of different kinds. The degree distributions of random graphs as introduced by Erdös and Rényi (Erdös and Rényi, 1959), for example, follow a Poisson distribution and are characterised by a low average shortest path length and a low value of the clustering coefficient, while regular lattices are rather characterised by a higher average shortest path length and a higher clustering coefficient. Many real-world networks possess a so-called small-world behaviour that manifests as a low average shortest path length and a high clustering coefficient (Watts and Strogatz, 1998; Barrat and Weigt, 2000). Networks whose degree distribution follows a power-law for high degrees are called scale-free networks (Barabási and Albert, 1999).

2.4.3. Recurrence networks

There are three major approaches how to transform a time series into a network: visibility graphs, transition networks, and proximity networks (Donner et al., 2011a). Visibility graphs use the convexity of observations to establish edges between pairs of vertices that are not separated by an observation of larger magnitude. This class of networks has been shown to provide a test for time series irreversibility (Lacasa et al., 2012). Transition networks are characterised by discrete states and corresponding transition probabilities. Proximity networks are networks that are based on some kind of proximity relationship between observations. We here focus on recurrence networks as a special class of the proximity networks that makes use of the recurrence properties of the system (Marwan et al., 2009; Donner et al., 2010b; Donner et al., 2015).

To be more precise, the adjacency matrix of a recurrence network is obtained by reinterpreting the underlying recurrence matrix of a system (equation (2.8)) as adjacency matrix of the network

$$A_{i,j}(\epsilon) = R_{i,j}(\epsilon) - \delta_{ij} \tag{2.16}$$

where the Kronecker delta δ_{ij} excludes self loops. That is, the vertices of the network correspond to the times t_i and are associated with the states of the system in phase space $\vec{x}(t_i)$. Two vertices are linked by an edge if their distance in phase space is smaller than the threshold ϵ. Thus, the network contains geometric information about the system's attractor that can be quantified using the network measures introduced in subsection 2.4.2.

Figure 2.7 shows exemplary recurrence networks of the Lorenz and the Rössler systems introduced in section 2.2. The threshold ϵ was set adaptively by choosing a fixed recurrence rate of $RR = 0.05$ (corresponding to the edge density $\rho = 0.05$

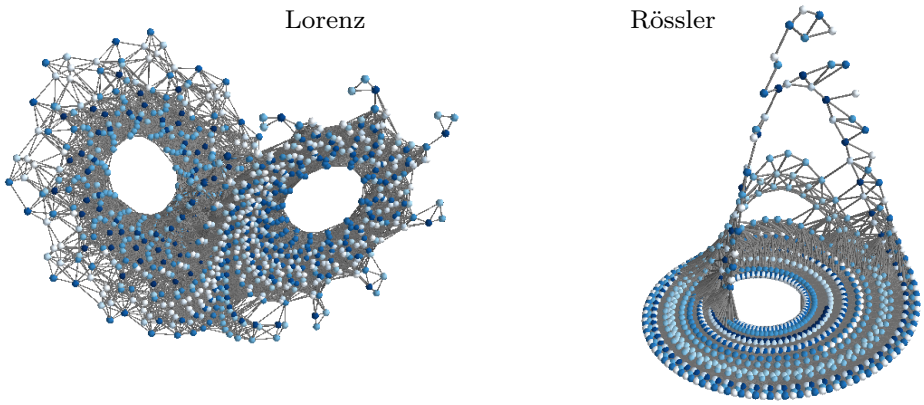

Figure 2.7.: Recurrence network representation of the Lorenz system (left) and the Rössler system (right) with parameter choices given in section 2.2 for a fixed recurrence rate of $RR = 0.05$. Time evolution goes from light blue to dark blue.

in the network). As expected, the network structure preserves the geometry of the underlying attractors.

In particular, the information obtained from a recurrence network is complementary to that from a recurrence plot as no dynamic information is taken into account. That is, the network properties remain the same when relabelling the vertices, while the recurrence plot makes use of the time-ordering of the time series. Both concepts do not require a regular sampling in the time domain, the requirement for obtaining reliable results is rather that the relevant phase space of the system is sufficiently covered with data points (Zou et al., 2019). Still, non-uniform sampling poses challenges for the reconstruction of the system's phase space as seen in section 2.3 and further discussed in chapter 3. As the reconstruction is usually required for recurrence network analysis when only a univariate time series is measured, regular sampling of the data is of advantage.

Recurrence networks have been mostly used to either classify systems or to detect dynamical anomalies in non-stationary time series by applying a sliding window approach (Marwan et al., 2009; Donner et al., 2011a). For system classifications, different approaches, such as studying subgraphs, using network measures like the network transitivity, and more sophisticated classifications based on a complexity-entropy plane, can be pursued (Xu et al., 2008; Donner et al., 2011b; Wiedermann et al., 2017). As we particularly focus on the sliding window approach in this thesis, we describe it in more detail in subsection 2.4.4.

The network transitivity $\mathcal{T}$ (equation (2.14)) has been shown to be particularly useful for characterising system dynamics as it can be related to a generalised fractal dimension (Donner et al., 2011b). For a random geometric graph in an integer-dimensional space, the expected network transitivity of a recurrence network is an

analytical function that decays exponentially with dimension m. This result is exact when using the maximum norm and approximate for other norms. From those considerations, upper and lower transitivity dimensions can be derived as (Donner et al., 2011b)

$$D_{\mathcal{T}}^{u} = \max_{\epsilon \in \mathrm{E}} \frac{\log(\mathcal{T}(\epsilon))}{\log(3/4)} \tag{2.17}$$

$$D_{\mathcal{T}}^{l} = \min_{\epsilon \in \mathrm{E}} \frac{\log(\mathcal{T}(\epsilon))}{\log(3/4)} \tag{2.18}$$

where E is a suitable set of values of the threshold. To obtain the relation between the network transitivity and the dimensionality of a system in practical applications, constructing one network for one value of ϵ usually suffices (Zou et al., 2019)

$$D_{\mathcal{T}} = \frac{\log(\mathcal{T})}{\log(3/4)}. \tag{2.19}$$

Additionally, as stable estimates of network properties can already be obtained from networks of 100 vertices (Donges et al., 2011a; Donges et al., 2011b), the relation can be used to classify time series of short length and also in the sliding window approach.

For estimating a reasonable value of the threshold ϵ to construct the recurrence network, different approaches have been suggested (e. g. Eroglu et al., 2014; Kraemer et al., 2018). The threshold has a great influence on the resulting measures of the network as for example shown in Donner et al. (2010a) and Donner et al. (2010b). Generally, a high threshold leads to a sparse network with possibly many unconnected network components, while a low threshold leads to a highly connected network that possibly prevents characteristic small-scale structures to be detected. Thus, a good threshold should balance the effects of not having many disconnected components and unveiling those small-scale structures.

If the analysed time series has a high sampling rate, spurious autocorrelations might obscure the estimation of the network properties which can be corrected for example by downsampling the time series or by applying Theiler windows (Theiler, 1986). If the time series has quantified uncertainties, the framework proposed by Goswami et al. can be applied to directly incorporate these uncertainties in the analysis (Goswami et al., 2018). Also, the effect of noise on the network has been studied and the attractor as quantified by the recurrence network has been shown to be robust under the addition of noise (Jacob et al., 2016).

There is a large additional body of literature dealing with the properties of recurrence networks. For example, an analytical framework for recurrence networks has been developed (Donges et al., 2012). Also, hypothesis testing using recurrence networks has been studied (Jacob et al., 2018) and various extensions such as inter-system and joint recurrence networks (Feldhoff et al., 2012; Feldhoff et al., 2013), multiplex recurrence networks (Eroglu et al., 2018), weighted recurrence networks (Jacob et al., 2019), and scale-specific recurrence networks (section 2.5) exist. Those approaches

have recently been reviewed in detail in Zou et al. (2019).

2.4.4. Windowed analysis

A major part of the thesis is concerned with detecting dynamical anomalies in time series. For this, we perform recurrence network analysis with a sliding window approach to obtain both geometric and dynamic information. This windowed approach has already been successfully applied to gain information about dynamical anomalies in various time series (e. g. Donges et al., 2011a; Donges et al., 2011b; Donges et al., 2015a).

In a first step, we split the (possibly embedded) time series $\vec{x}(t)$ of length N into windows of size W with offset dW. Thereby, we obtain $(N - W)/dW$ slices of the time series. For each slice, we construct a recurrence network by computing the adjacency matrix (2.16) using maximum norm

$$\|\vec{x}\|_\infty = \max_{k=1,\ldots,m} \left\{ x^{(k)} \right\} \tag{2.20}$$

where m is the (embedding) dimension of the time series $\vec{x}(t)$. The threshold is set adaptively by fixing the recurrence rate to $RR = 0.05$ following the recommendations in Donner et al. (2010a). Then, for each recurrence network, we calculate network measures like the network transitivity (2.14) or the average shortest path length (2.15). Thus, we end up with a time series of the network measure where the times associated to the values of the network measure correspond to the latest time covered by the slice, i. e., we consider the network measure to quantify the dynamics of the preceding W time points. For constructing recurrence networks from time series and calculating the network measures, we use the python package *pyunicorn* (Donges et al., 2015b).

Figure 2.8 shows exemplary results of the network transitivity and the average shortest path length of the windowed recurrence network analysis (wRNA) for window width $W = 200$ for a non-stationary Rössler system with time varying parameter $b_R(t) = b_{R,0} + \Delta b_R(t - t_0)$ with $b_{R,0} = 0.02$ and $\Delta b_R = 0.001$, while the parameters a_R and c_R are fixed to $a_R = 0.2$, $c_R = 5.7$. More details on this system and an interpretation of the obtained results can be found in chapters 3 and 4.

It should be noted that the results of the wRNA depend on the choice of the window width W. Currently, the choices of W are heuristically motivated and future work should be devoted to develop an objective, theoretically grounded estimation procedure for reasonable choices of the window width (Zou et al., 2019). In this thesis, we will pursue the approach to repeat the analysis for various choices of the window width to check the results for robustness with respect to this analysis parameter.

Also, as discussed above, recurrence network analysis itself does not require a regular sampling of the data. Still, non-uniformly sampled observation times pose a challenge for the interpretation of the results for windowed analyses. If the network transitivity of a slice is obtained for a fixed number of observations, different time periods are covered within the slices. If the results are obtained for a fixed period of time, a different number of observations is present within each slice. This is why

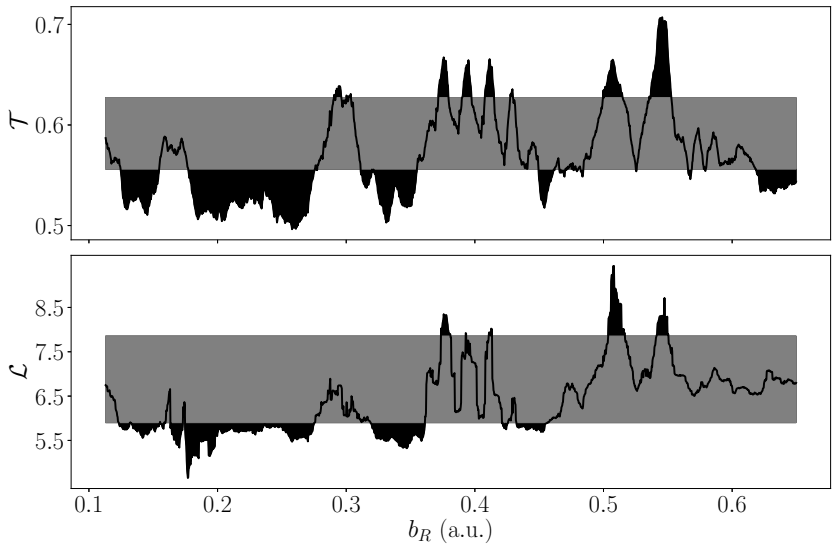

Figure 2.8.: Windowed recurrence network analysis ($W = 200\,\langle dt \rangle$, $RR = 0.05$) of the non-stationary Rössler system (top: network transitivity $\mathcal{T}$, bottom: average shortest path length $\mathcal{L}$) reconstructed from the x-component using time delay embedding for delay time $\tau = 5\,\langle dt \rangle$ and embedding dimension $m = 3$. The grey bars denote confidence bounds derived from random shuffling surrogates (see section 2.6).

we here only use uniformly sampled or to uniform sampling interpolated time series when applying the sliding window approach.

2.5. Scale-specific recurrence network analysis

In some cases, it is useful to study the dynamics of the different time scales of the system separately. In such cases, we use scale-specific recurrence network analysis which is an extension of traditional recurrence network analysis where the time series is filtered before it is transformed into a network. This approach has already been successfully applied for classifying various systems (Gao et al., 2015; Xiang et al., 2012; Chen and Yang, 2012; Deng, 2014; Yi et al., 2013; Yin and Shang, 2016).

It should be noted that this type of approach has sometimes been termed multi-scale recurrence network analysis. With regard to other established multi-scale methods such as multi-scale entropy that combine information from different time scales rather than separating them, we think that for the analysis presented here, where we separately analyse the different time scales of the system, the term scale-specific recurrence network analysis is more appropriate.

To be precise, we use the continuous wavelet transform W_Ψ to filter the time series before applying wRNA. That is, given the time series $\vec{x}(t)$ representing the studied

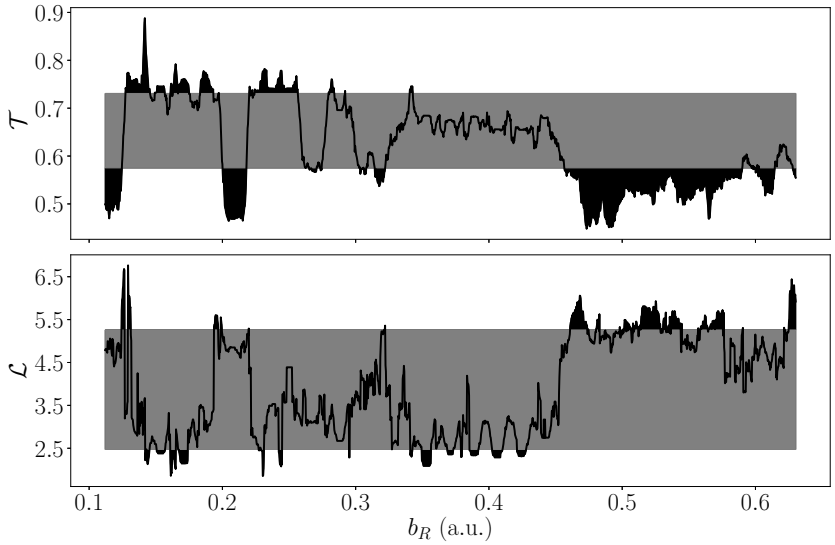

Figure 2.9.: Same as in figure 2.8 but for wssRNA at a scale of $s = 8.2$.

system, each component of the time series is filtered separately with respect to the wavelet Ψ for different scales s and times b (Torrence and Compo, 1998)

$$W_\Psi x(t)[b,s] = \int \frac{1}{\sqrt{s}} \overline{\Psi}\left(\frac{t-b}{s}\right) x(t) dt \tag{2.21}$$

with the bar denoting the complex conjugate. As wavelet, we use the complex Morlet wavelet

$$\Psi(t) = \frac{1}{\sqrt{\pi B}} \exp\left(\frac{-t^2}{B}\right) \exp\left(2\pi \mathrm{i} C t\right), \tag{2.22}$$

where B is the bandwidth and C is the center frequency of the wavelet. Those parameters are closely related to the resolution of the analysis and should be chosen data- and application-dependent. One way to fix the parameters is, for example, to match them to the main frequency and bandwidth of the analysed data. Also, it should be noted that the wavelet and its corresponding centre frequency determine the relation between the scales of the wavelet transform and the frequencies present within the data. In particular, the scale s can be approximated as the dimensionless fraction of the centre frequency of the wavelet and the frequency of the data, or, equivalently, the analysed frequency of the data is given as the centre frequency divided by the scale (Torrence and Compo, 1998). In this thesis, we fix the parameters to be $B = 2.0\,(\langle dt \rangle)^{-1}$ and $C = 1.0\,(\langle dt \rangle)^{-1}$, that is, the analysed frequencies can be approximated as the inverse of the scales.

We then use the real part of the filtered signal for each component as filtered time series. To account for edge effects, we cut the first and the last

$$N_c = \frac{\text{supp}\,(\Psi) - 1}{2}$$

points. The support of the wavelet $\text{supp}\,(\Psi)$ depends on the implementation of the wavelet and is a function of the scale s. We use the python package *pywt* for performing the wavelet transform. In this case, the support of the wavelet is given as $\text{supp}\,(\Psi) = 16s + 1$.

For each considered scale s, we perform the windowed analysis as outlined in subsection 2.4.4. The window width of the analysis is chosen dependent on the corresponding scale as

$$W = \max\,(100, \text{supp}\,(\Psi)) \tag{2.23}$$

because at least 100 nodes are required to calculate reliable network measures from a recurrence network (Donges et al., 2011a; Donner et al., 2015).

Exemplary results of windowed scale-specific recurrence network analysis (wssRNA) for the non-stationary Rössler system for a scale of $s = 8.2$ can be found in figure 2.9.

2.6. Significance testing and surrogate data

When characterising the dynamics of a system using non-linear methods, the question whether the results could also have been obtained from an underlying linear or stochastic process naturally arises. To assess the meaning of the results and give well-grounded interpretations, a significance test is required.

2.6.1. Hypothesis testing

For this, first, a null hypothesis against which the observations are tested and a confidence level $s = 1 - \alpha$ at which the test is performed have to be specified. Second, a discriminating statistic that is used to characterise the original system is applied to the original data and compared to the expected behaviour of the statistic under the validity of the null model (Theiler et al., 1992). After the test, the null hypothesis is either accepted or rejected with respect to the specified confidence level. Accepting the null hypothesis means that the value of the statistic for the original data is compatible with the expected results for the null hypothesis, while rejecting it means that the value for the original system differs significantly from those expected under the null hypothesis. During this procedure, two types of errors may occur. Type I errors indicate that the null hypothesis is rejected even though it is actually true. Thus, we refer to this type of errors as false positives. The probability of a type I error is given as α. Type II errors, on the other hand, denote the situation that the null hypothesis is accepted although it is false, i. e., we refer to such errors as false negatives (Rice, 2007).

An alternative way to describe the test results is using the p-value of the statistic for the original time series. The p-value gives the probability that the resulting statistic was obtained by a realisation of the null model. Thus, p-values smaller than α denote results that differ significantly from the expected values of the statistic under the null hypothesis and like this, lead to a rejection of the null hypothesis.

In case that the significance test is applied repeatedly, the probability that some of the results are falsely classified as positives increases with the number of tests (Miller, 1981). This problem is known as multiple testing and should be corrected for. A simple way to do so is to divide the α or, equivalently, the p-value by the number of tests that are applied and use this as the new threshold for the results to be significant. Additionally, more sophisticated approaches to tackle the problem of multiple testing have been put forward (Holm, 1979; Hochberg and Benjamini, 1990; Westfall and Young, 1993).

2.6.2. Surrogate data

A crucial step for significance testing is choosing the null model and deriving the expected distribution of the discriminating statistic for it. As this is generally not possible analytically, we here use the method of surrogate data, that is, we perform a Monte Carlo simulation of the discriminating statistic. In a first step, N_s surrogate data sets are created according to the chosen null model. Then, for each surrogate data set, the statistic is calculated and the results are used to approximate the expected distribution of the statistic for the given null model (Theiler et al., 1992).

There are various choices of null models and, depending on the original data and the applications, different null models might be better suited. In climate applications, autoregressive processes of order 1 (AR(1) processes) are for example often used as null model (e. g. von Storch and Zwiers, 1999; Løvsletten and Rypdal, 2016). We here present the null models and corresponding surrogate data creation routines that are used throughout the thesis.

The simplest case is the one of an uncorrelated stochastic process with normal distribution, that is, of Gaussian white noise (GWN). The probability density function of this process is given as

$$p_G(x) = \frac{1}{\sqrt{2\pi}\sigma} \exp\left(\frac{(x-\mu)^2}{2\sigma^2}\right), \tag{2.24}$$

where μ denotes the mean and σ the standard deviation of the distribution. To create sets of surrogate data of length N with respect to this null model, the mean and standard deviation are chosen according to the mean and standard deviation of the original data and N samples are drawn from the resulting distribution.

Another case is that of a short-term correlated stochastic process. For this, we consider an AR(1) process

$$s(t+1) = c + \rho s(t) + \epsilon_t \tag{2.25}$$

where c is the offset (drift term), ρ is the scaling factor, and ϵ_t is a Gaussian random variable with probability distribution (2.24), zero mean, and constant standard deviation σ_{ϵ_t}. The model parameters and the initial condition $s(0)$ are fitted to the original data and then, realisations with respect to these parameters are used as surrogate data sets.

An alternative possible null model are random shuffling surrogates where the original time series is shuffled such that the resulting surrogate time series has exactly the same amplitude distribution as the original time series but is otherwise random. In particular, the correlation structure of the original time series is not preserved. Mathematically, this can be expressed as

$$s(t_i) = x(t_{\pi(i)}) \tag{2.26}$$

for $i \in [1, N]$ and $\pi(\cdot)$ a random permutation on the indices.

Sometimes, it is useful to use surrogate data that not only preserve the amplitude distribution but also the (linear) correlation structure of the original data. For this case, we use iterative amplitude-adjusted Fourier transform (iAAFT) surrogates (Schreiber and Schmitz, 1996). Given, the set of original data $\{x_n = x(t_n)\}$ for $n \in [1, N]$, we first store a copy of the original data sorted in ascending magnitude in the set $\{c_n\}$, calculate the Fourier amplitudes of the original data

$$|S_k| = \left| \frac{1}{\sqrt{N}} \sum_{n=1}^{N} x_n \exp\left(\frac{2\pi \mathrm{i} k n}{N}\right) \right|, \tag{2.27}$$

and create an initial set of random shuffling surrogates $\{r_n^{(0)} = x_{\pi(n)}\}$. Then we iteratively replace the Fourier amplitudes of $\{r_n^{(j)}\}$ by the original Fourier amplitudes to obtain $\{s_n^{(j)}\}$ and rank-order the $\{s_n^{(j)}\}$ to get $\{r_n^{(j+1)}\}$ with the original amplitudes stored in $\{c_n\}$.

To be precise, to get from $\{r_n^{(j)}\}$ to $\{s_n^{(j)}\}$, we apply a Fourier transform to the $\{r_n^{(j)}\}$ as

$$R_k^{(j)} = \frac{1}{\sqrt{N}} \sum_{n=1}^{N} r_n \exp\left(\frac{2\pi \mathrm{i} k n}{N}\right) \tag{2.28}$$

and replace the Fourier amplitudes by the original amplitudes $|S_k|$ while keeping the phases $R_k^{(j)} / \left|R_k^{(j)}\right|$

$$s_n^{(j)} = \frac{1}{\sqrt{N}} \sum_{k=1}^{N} \frac{R_k^{(j)}}{|R_k^{(j)}|} |S_k| \exp\left(-\frac{2\pi \mathrm{i} k n}{N}\right). \tag{2.29}$$

To get the $\{r_n^{(j+1)}\}$ from the $\{s_n^{(j)}\}$, we perform a rank ordering of the $\{s_n^{(j)}\}$ and write the corresponding original amplitudes as saved in $\{c_n\}$ to the new iteration

$$r_n^{(j+1)} = c_{\mathrm{rank}(s_n^{(j)})}. \tag{2.30}$$

For large $j \geq f$, the iteration converges to a fixed point (Schreiber and Schmitz, 2000). Whether to use $\{r_n^{(f)}\}$ or $\{s_n^{(f)}\}$ as final surrogate data set depends on the application, though $\{s_n^{(f)}\}$ should be preferred when linear correlations are present within the data (Schreiber and Schmitz, 2000).

All those null models correspond to different null hypotheses on the process underlying the original data, i. e., the studied system. The different null models share some of the structure of the original data. In the case of GWN, this concerns the mean and the standard deviation of the amplitude distribution of the data, for the random shuffling surrogates this is the exact amplitude distribution, and for the iAAFT surrogates, both the amplitude distribution and the linear correlation structure are preserved. For the AR(1) model, the model parameters were chosen depending on the original data. A rejection of the null hypothesis thus signifies deviations from the underlying null model and, correspondingly, that there is more structure in the original data than in the surrogate data (Schreiber and Schmitz, 2000).

Chapter 3.

Phase space reconstruction for non-uniformly sampled noisy time series

In this chapter, we systematically study the performance of different approaches for phase space reconstruction when the available data are non-uniformly sampled and contaminated with noise. In particular, we compare uniform time delay embedding to derivative embedding for different methods to estimate the derivatives. To assess the quality of the reconstructions, we use the relation between recurrence network measures and the geometry of the attractor of the underlying system. By studying the well-known paradigmatic Lorenz and Rössler system, we can compare network measures obtained for the reconstructed attractors to those of the original attractors for varying noise levels and shapes of the sampling interval distribution. We additionally study the implications of the different reconstruction approaches when analysing a non-stationary Rössler system using windowed recurrence network analysis (wRNA).

This chapter is based on, and closely follows, publication P1.

3.1. Introduction

The reconstruction of a system's higher-dimensional phase space from experimentally measured data is required when the dynamics of the underlying dynamical system are expected to be higher-dimensional than the dimension of the measured time series. The quality of this phase space reconstruction may significantly influence the results of further analyses, in particular, when the available data are non-uniformly sampled and subject to noise. As discussed in section 2.3, the problem of finding a proper phase space reconstruction for a given time series is still a remaining challenge in non-linear time series analysis and subject of ongoing research.

Time delay embedding, on the one hand, is not well defined for non-uniformly sampled data as the choice of any delay time requires the data to be sampled as multiples of that delay time. In the case of non-equal sampling intervals, this requirement cannot be met and the interpolation of the data is unavoidably leading to errors in the subsequent analyses (Rehfeld et al., 2011). Also, the estimation of the embedding parameters relies on concepts such as the autocorrelation or the mutual information of the data which are usually defined for uniformly sampled data

even though, in some cases, estimators that can deal with non-uniform sampling are available (Rehfeld et al., 2011; Rehfeld and Kurths, 2014).

Derivative embedding, on the other hand, does not suffer from these conceptual difficulties. Instead, the robust estimation of higher-order derivatives for noisy data is a major challenge that so far prevented a wide-spread use of this approach in real-world applications.

A systematic comparison of derivative embedding for different ways of estimating the derivatives and the comparison of these methods to uniform time delay embedding is still lacking for non-uniformly sampled noisy time series. We here aim at filling this gap and providing valuable insight into the potentials and limitations of the different approaches. As we are particularly interested in the influence of the different phase space reconstructions on the results of a subsequent recurrence network analysis, we use the relation between the network measures of recurrence networks and the geometry of the attractor of the underlying dynamical system to quantify the quality of the reconstructions. We first introduce the different approaches for estimating derivatives from non-uniformly sampled noisy time series and the analysis framework in sections 3.2 and 3.3. Then, we present the results obtained for the different approaches in section 3.4 and summarise the conclusions in section 3.5.

3.2. Estimating derivatives

We consider a univariate time series $x_i = x(t_i)$ for $i \in [1, N]$ with possibly non-uniform sampling intervals $\Delta t_i = t_{i+1} - t_i$ and aim at estimating the derivatives

$$\left.\frac{d^j x(t)}{dt^j}\right|_{t=t_i} \equiv \frac{d^j}{dt^j} x_i \tag{3.1}$$

for all times t_i up to some order $j_{\max}$.

3.2.1. Central differences

The most intuitive approach for doing so, is to use central differences as approximations of the derivatives. In the case of uniform sampling, the central difference quotient is given as

$$\frac{d}{dt} x_i \approx \frac{x_{i+1} - x_{i-1}}{2\Delta t}. \tag{3.2}$$

It is possible to generalise this formula to the case of non-uniformly sampled data

$$\frac{d}{dt} x_i \approx \frac{\Delta t_{i-1}^2 x_{i+1} - (\Delta t_{i-1}^2 - \Delta t_i^2) x_i - \Delta t_i^2 x_{i-1}}{\Delta t_{i-1} \Delta t_i (\Delta t_{i-1} + \Delta t_i)}. \tag{3.3}$$

This expression reduces to equation (3.2) when $\Delta t_i = \Delta t_{i-1}$, i. e., if the data are uniformly sampled.

The above expression can be derived by approximating the values of the neighbouring points of x_i using a Taylor expansion up to second order

$$x_{i-1} \approx x_i - \Delta t_{i-1} \frac{d}{dt} x_i + \frac{\Delta t_{i-1}^2}{2} \frac{d^2}{dt^2} x_i, \tag{3.4}$$

$$x_{i+1} \approx x_i + \Delta t_i \frac{d}{dt} x_i + \frac{\Delta t_i^2}{2} \frac{d^2}{dt^2} x_i. \tag{3.5}$$

Then, the term with the second derivatives is eliminated from this system of equations. Equation (3.3) is obtained by solving for $\frac{d}{dt} x_i$. To approximate higher order derivatives, equation (3.3) can be applied iteratively.

3.2.2. Discrete Legendre polynomials

Another approach for estimating derivatives uses the relation between the discrete Legendre polynomials $r_{j,p,n}^{(i)} = r_{j,p}(\Delta t_{i,n})$, where $\Delta t_{i,n} = t_{i+n} - t_i$, and the derivatives of a time series (Gibson et al., 1992)

$$\frac{d^j}{dt^j} x_i \approx \frac{j!}{c_{j,p}(\Delta t_{i,n})} \sum_{n=-p}^{p} r_{j,p,n}^{(i)} x_{i+n} \tag{3.6}$$

with the normalisation given by

$$c_{j,p}(\Delta t_{i,n}) = \sum_{n=-p}^{p} (\Delta t_{i,n})^j r_{j,p,n}^{(i)}. \tag{3.7}$$

That is, the jth derivative at x_i is proportional to a weighted sum of the p neighbouring points of x_i to each side with the weights corresponding to the discrete Legendre polynomials that can be calculated using the recursive relation

$$r_{j,p,n}^{(i)} = \frac{1}{c_j p^j} \left[\Delta t_{i,n}^j - \sum_{k=0}^{j-1} r_{k,p,n}^{(i)} \sum_{l=-p}^{p} \Delta t_{i,l}^j r_{k,p,l}^{(i)} \right] \tag{3.8}$$

for $2p \geq j$ and $r_{0,p,n}^{(i)} = 1/c_0$. The constants c_j can be determined from the conditions

$$\sum_{n=-p}^{p} (r_{j,p,n}^{(i)})^2 = 1. \tag{3.9}$$

Equation (3.6) is derived in appendix A.1.

For $p \to \infty$, the discrete Legendre polynomials converge to the ordinary Legendre polynomials. In the opposite limit of p being as small as possible, the approach corresponds to a central difference quotient. That is, the choice of the number of neighbouring points p that are taken into account for estimating the derivatives,

controls the smoothing of the data which can be useful when dealing with noisy time series.

The exact choice of p should depend on the maximum order $j_{\max}$ up to which derivatives are estimated. Gibson et al. provide a heuristic to estimate the optimal value of p and note that another possible approach could be choosing p such that $2p+1$ points cover approximately a quarter of an oscillation of the time series (Gibson et al., 1992).

The numerical calculations of derivatives within the framework of discrete Legendre polynomials have been performed using an adapted version of the algorithm for generalised Legendre coordinates available in the python package *pyunicorn* (Donges et al., 2015b).

3.2.3. Moving Taylor Bayesian Regression

A third approach to locally estimate derivatives is to use the framework of moving Taylor Bayesian regression (MoTaBaR) introduced in Heitzig (2013). As input, the method requires a measured time series of N data points $\{x_i\}_{i=1}^N$ and corresponding uncertainty estimates that may represent, for example, measurement errors or time uncertainties. Additionally, prior beliefs about the variability of the function f underlying the time series and its derivatives up to order $j-1$ have to be specified. If no such information is available, non-informative priors can be used (Heitzig, 2013). Then the method combines a local Taylor approximation of the time series around some time of interest ξ, taking into account N_{mtb} points, with Bayesian updating in order to derive posterior distributions of the function's values and the values of its derivatives. The posterior mean and variance are then used as final estimators for those quantities. Like this, the method can also be used to interpolate data, can incorporate measurement uncertainties, and gives uncertainty estimates of the results.

To be more precise, we here assume that the argument and measurement errors (denoted as γ_i and ϵ_i, respectively) are Gaussian and that no prior information about the variability of the function f and its derivatives is available. The measured values $\{x_i\}_{i=1}^N$ can be related to the derivatives $\varphi^\alpha = \frac{d^\alpha f(\xi)}{dt^\alpha}$ by a local Taylor expansion

$$x_i = \sum_{\alpha=0}^{j-1} T_{i,\alpha}\varphi^\alpha + r_i + \epsilon_i. \tag{3.10}$$

Here, the $T_{i,\alpha}$ are given as

$$T_{i,\alpha} = \frac{(t_i - \gamma_i - \xi)^\alpha}{\alpha!}, \tag{3.11}$$

while the Taylor residual r_i is given as

$$r_i = T_{i,j}\psi_i, \tag{3.12}$$

$$\psi_i = \frac{d^j}{dt^j} f(\xi + \lambda_i(t_i - \gamma_i - \xi)) \tag{3.13}$$

for $\lambda_i \in [0, 1]$. As we have non-informative priors, the prior variance is $\Sigma_\varphi^{-1} = 0$ and the prior mean of ψ is $\mu_\psi = 0$. The posterior mean $\tilde{\mu}_\varphi$ and variance $\tilde{\Sigma}_\varphi$ of f and its derivatives can be estimated as follows:

(i) For $\alpha < j$, calculate $T_{i,\alpha}$ for all i from t, γ and ξ by making use of equation (3.11).

(ii) Based on the prior belief about $(\Sigma_\psi)_{i,k}$, calculate $(\Sigma_r)_{i,k}$ as

$$(\Sigma_r)_{i,k} = T_{i,j} \, (\Sigma_\psi)_{i,k} \, T_{k,j}.$$

(iii) Calculate $W = (\Sigma_r + \Sigma_\epsilon)^{-1}$.

(iv) Obtain the posterior variance and mean of φ as

$$\tilde{\Sigma}_\varphi = (T'WT)$$
$$\tilde{\mu}_\varphi = \tilde{\Sigma}_\varphi(T'Wx).$$

When knowing the distribution of the argument errors $\rho(\gamma|t)$, it is possible to obtain the final estimators $\hat{\varphi}$ and $\hat{\Sigma}_\varphi$ by integrating over all possible argument errors. A more general description and a link to a python implementation of the method are available in Heitzig (2013).

3.3. Analysis procedure

To study the behaviour of the different phase space reconstruction approaches for non-uniformly sampled noisy data, we consider the two model systems introduced in section 2.2. For the Lorenz system, we use the canonical parameters $a_L = 10$, $b_L = 28$, $c_L = 8/3$ and initial conditions $(x_0, y_0, z_0) = (-8.0, 8.0, 27.0)$, while for the Rössler system, we study a slightly adjusted set of parameters $a_R = 0.15$, $b_R = 0.2$, $c_R = 10.0$ and initial conditions $(x_0, y_0, z_0) = (0.5, 0.0, 0.0)$ that also lead to a chaotic solution.

In a first step, we create high-resolution uniformly sampled reference solutions by numerically integrating the respective set of differential equations with sampling rate $dt = 0.001$ for times in the interval $[0, 100]$ for the Lorenz and in the interval $[0, 300]$ for the Rössler system and discarding the first $50,000$ data points to account for transients. Thus, we end up with reference time series of length $N_{\text{ref}} = 250,000$ and $N_{\text{ref}} = 50,000$ data points, respectively. This choice of integration times corresponds to about 40 oscillations being present in each time series.

In a second step, for each model system, we create $N_{\text{R}} = 500$ non-uniformly sampled noisy realisations of length $N = 500$ from the x-coordinate of the reference time series where the choice of $N = 500$ was motivated by the limited data availability in real-world applications. As in such applications, sampling interval distributions can

often be approximated by gamma distributions, the realisation of the non-uniform sampling is achieved by drawing $N-1$ sampling intervals from a gamma distribution

$$p_\Gamma(t) = t^{k-1}\frac{\exp(-t/\theta)}{\theta^k \Gamma(k)} \tag{3.14}$$

with θ being the scale and k being the shape parameter of the distribution. The non-uniformly sampled time series is obtained by rounding the drawn sampling intervals to be multiples of the reference sampling rate dt, cumulatively adding the rounded $N-1$ time intervals to $t_0 = 50.0$, and choosing the corresponding values of the x-coordinate. Then, we add Gaussian white noise (equation (2.24)) of mean μ and standard deviation σ to the data

$$x_i \to x_i + \eta_i \tag{3.15}$$

where η_i is the Gaussian random variable. It should be noted that the average sampling rate $\langle dt \rangle$ of these realisations is different from the sampling rate dt which was used to numerically solve the sets of ordinary differential equations.

The N_R realisations of the non-uniformly sampled noisy time series corresponding to a certain shape of the sampling interval distribution and a certain noise level are then used as basis to quantify the quality of different phase space reconstruction approaches. First, we perform a linear and a cubic spline interpolation, and then, reconstruct the phase space of the model systems using uniform time delay embedding for the two interpolations and derivative embedding for the non-uniformly sampled and the two interpolated data sets using central differences, discrete Legendre polynomials, and MoTaBaR to estimate the derivatives for varying embedding dimensions $m \in [3, 5]$. For MoTaBaR, we additionally consider non-uniform input but uniform output using the internal interpolation routine of the method. As for derivative embedding, the values of the higher-dimensional coordinates are of larger magnitude, we also consider the case where each coordinate is normalised to have zero mean and unit variance.

For all those different reconstructions, we transform the time series into a recurrence network by using the maximum norm to calculate distances in phase space and a fixed recurrence rate $RR = 0.05$ to set the recurrence threshold adaptively. We then calculate the network transitivity and the average path length of the corresponding networks and compare it to the network transitivity and average path length obtained from a (x, y, z) reference solution of $N = 500$ points with regular sampling and the sampling time corresponding to the average sampling time $\langle dt \rangle$ of the non-uniformly sampled realisations. The relative distance of the network measures obtained for the different reconstructions to the reference network measures, $\Delta\mathcal{T}$ and $\Delta\mathcal{L}$, respectively, is given as

$$\Delta\mathcal{T} = \frac{|\mathcal{T}_\mathrm{ref} - \mathcal{T}|}{\mathcal{T}_\mathrm{ref}}, \qquad \Delta\mathcal{L} = \frac{|\mathcal{L}_\mathrm{ref} - \mathcal{L}|}{\mathcal{L}_\mathrm{ref}}. \tag{3.16}$$

The mean and the standard deviation of $\Delta\mathcal{T}$ and $\Delta\mathcal{L}$ for the N_{R} realisations can be used to quantify the quality of the different phase space reconstruction approaches.

3.4. Results

We now present the results of the analysis described in section 3.3 when varying the noise level and the shape parameter of the gamma distribution that controls the distribution of the non-uniform sampling intervals. Based on these results, we analyse a non-uniformly sampled noisy non-stationary version of the Rössler system using wRNA for the different phase space reconstruction approaches in order to study the implications of the results when applying the windowed version of the method.

3.4.1. System classification using recurrence network measures

To evaluate the relative distances of the network measures (3.16) between the reference solution and the different phase space reconstructions, we follow the analysis procedure described in section 3.3 for fixed scale parameter $\theta = 8.0$ and varying shape parameter $k \in [0.25, 2.0]$ of the gamma distribution. The mean of the white noise that is added to the non-uniformly sampled time series is given as $\mu = 0$, while the standard deviation σ is varied in the interval $[0.25, 2.0]$.

In order to compare the performance of the different phase space reconstruction approaches, we first, for each approach, need to decide which embedding parameters to use, whether to use the non-uniformly sampled data or one of the interpolated sampling realisations of the data, and, for derivative embedding, whether to scale the coordinates to unit variance or not. We here summarise the results of this step, a more detailed assessment of the corresponding choices can be found in appendix A.2.

For time delay embedding, we use the linearly interpolated data because this is the most commonly used interpolation approach in applications even though in some cases, spline interpolations can improve the results (see appendix A.2). The delay time is chosen as $\tau = 2\,\langle dt \rangle$ for the Lorenz and as $\tau = \langle dt \rangle$ for the Rössler system which is in accordance with the first root of the corresponding autocorrelation functions.

For derivative embedding with central differences, we find that the results for the cubic spline interpolated data when all coordinates are rescaled to unit variance perform best. When estimating the derivatives using the discrete Legendre polynomials, we also find that the cubic spline interpolation in combination with scaling the coordinates to unit variance gives the best results, except for the Rössler case, where the scaling does not improve the results. This may be related to the fact that the z-coordinate of the Rössler system possesses variations of larger magnitude than those in the x- and y-coordinates and thus, is better reproduced in the unscaled case. Concerning the number of points p that are taken into account to each side for estimating the derivatives, we get optimal performance for $p = 4$ for embedding dimension $m = 3$ and $p = 6$ for embedding dimensions $m = 4$ and $m = 5$. For estimating the derivatives using the MoTaBaR framework, the internal interpolation routine combined with scaling the coordinates to unit variance performs best. This

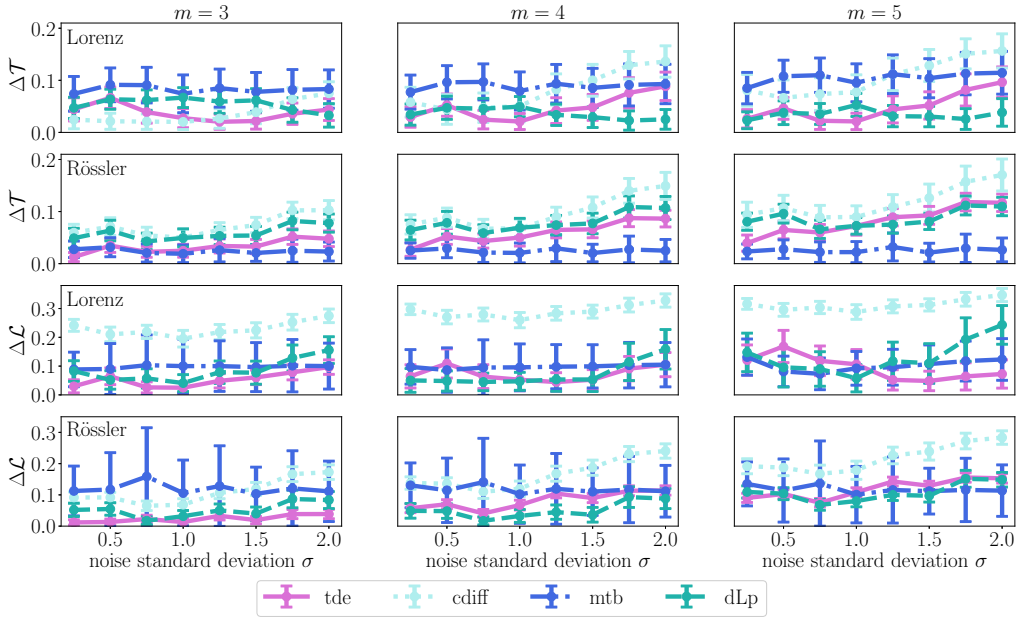

Figure 3.1.: Mean (points) and standard deviation (errorbars) of $\Delta\mathcal{T}$ and $\Delta\mathcal{L}$ of the $N_{\mathrm{R}} = 500$ realisations as a function of the standard deviation σ of the noise for the Lorenz and the Rössler system and increasing embedding dimension for different attractor reconstructions and fixed value of the shape parameter ($k = 1.0$). Purple solid lines: time delay embedding (tde) for $\tau = 2\,\langle\Delta t\rangle$ (Lorenz) and $\tau = \langle\Delta t\rangle$ (Rössler) and linear interpolation. Light blue dotted lines: central differences (cdiff) scaled to unit variance for cubic spline interpolation. Dark blue dash-dotted lines: MoTaBaR (mtb) based derivative estimates scaled to unit variance and internally interpolated. Cyan dashed lines: discrete Legendre polynomials (dLp) for $p = 4$ ($m = 3$) and $p = 6$ ($m = 4, 5$) for cubic spline interpolation scaled to unit variance (Lorenz) and without scaling (Rössler). Adapted from P1, with the permission of AIP Publishing.

method is relatively robust when varying the number of points N_{mtb} that are taken into account for performing the local Taylor approximation. Thus, we here only consider the case $N_{mtb} = 20$.

After having made those choices, we can compare the different approaches with each other. Figure 3.1 shows the results of the performance of the different phase space reconstruction approaches for the two network measures, the two model systems, and varying embedding dimension dependent on the standard deviation of the noise that was added to the time series before performing the reconstructions. The shape parameter of the gamma distribution is fixed to $k = 1.0$. When increasing the standard deviation of the noise, we expect to get worse results, that is, larger values of $\Delta\mathcal{T}$ and $\Delta\mathcal{L}$. The same holds for higher embedding dimensions because of noise amplification which is particularly relevant for derivative embedding.

For time delay embedding, we observe the expected behaviour for higher noise

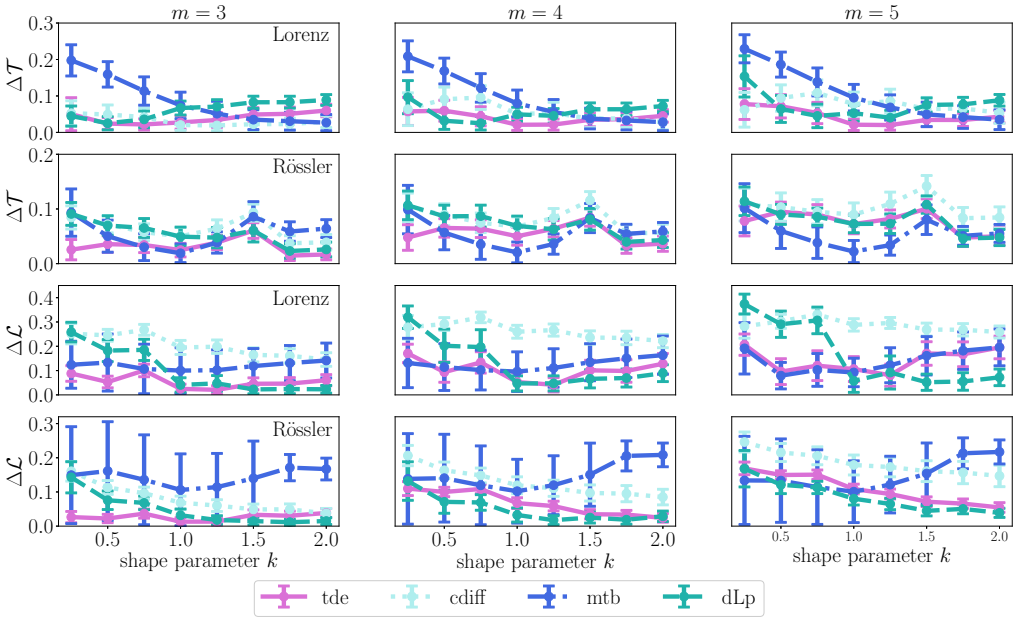

Figure 3.2.: Same as in Fig. 3.1 but for the dependence on the shape parameter k of the sampling interval distribution and fixed noise level ($\sigma = 1.0$). Adapted from P1, with the permission of AIP Publishing.

levels in many cases but see also, that this approach generally performs well, in particular, for the average path length in embedding dimension $m = 3$ and for $m = 5$ for the Lorenz system. For derivative embedding with central differences, we also see the expected trend for higher noise levels and note, that this approach does generally not perform as good as the others. When estimating the derivatives with the discrete Legendre polynomials, we observe the expected trend for high noise levels in some cases, while in other cases, particularly for the transitivity of the Lorenz system and the average path length of the Rössler system, the performance is relatively constant up to high values of the standard deviation of the noise. For MoTaBaR, the mean performance is relatively constant with respect to varying the noise level, but we note a higher variability within the realisations manifested in terms of a higher standard deviation. Also, this approach performs particularly well for the transitivity of the Rössler system.

Figure 3.2 shows the results analogously to the results in figure 3.1 but for varying shape parameter k and constant standard deviation of the added noise, given as $\sigma = 1.0$. We expect to observe decreasing values of $\Delta\mathcal{T}$ and $\Delta\mathcal{L}$ for higher values of the shape parameter as for those choices, the gamma distribution is more centred and thus, the sampling intervals are closer to uniform sampling.

For time delay embedding, we again observe a good performance and sometimes identify the expected trend, while for derivative embedding with central differences, the trend is not particularly visible. Also, this method performs in most cases worse

than the other methods when varying the shape parameter with an exception being the performance for the transitivity of the Lorenz system for embedding dimension $m = 3$. When estimating the derivatives using the discrete Legendre polynomials, the expected behaviour is often visible and particularly pronounced for the average path length of the Lorenz system. For derivative embedding with MoTaBaR, we often see the trend very clearly, but for the average path length, the performance gets worse for large values of the shape parameter, indicating that this method is best suited for intermediate values of k.

Overall, we find that time delay embedding based on linearly interpolated data performs quite well, even though, in some cases, it is outperformed by derivative embedding with the discrete Legendre polynomials or the MoTaBaR framework. Estimating the derivatives with the central difference quotient generally yields worse performance, thus, for derivative embedding, more sophisticated approaches for estimating the derivatives should be preferred. For MoTaBaR, we observe a high standard deviation for the N_{R} different realisations indicating a particular sensitivity to noise and the distribution of the sampling intervals. Thus, we identify the discrete Legendre polynomials to be the most reliable method for derivative embedding of non-uniformly sampled noisy data.

Also, we note that the differences to the reference network measures are generally smaller for the network transitivity than for the average shortest path length, which is one of the reasons, apart from the analytically obtained relation between the network transitivity and the dimensionality of the system dynamics (equation (2.19)), why in the following, we focus on the network transitivity.

3.4.2. Implications for windowed analyses

To compare the impact of the different phase space reconstruction approaches on wRNA, we study the non-stationary Rössler system with fixed parameters $a_R = 0.2$, $c_R = 5.7$ and time varying parameter $b_R(t) = b_{R,0} + \Delta b_R(t - t_0)$ with $b_{R,0} = 0.02$ and $\Delta b_R = 0.001$. To obtain a high resolution reference solution, we integrate the system for times $t \in [0, 630]$ with resolution $dt = 0.01$ and discard the first 3000 points to account for transients with respect to the chosen initial conditions $(x_0, y_0, z_0) = (0.5, 0.0, 0.0)$. Analogously to the analysis procedure described in section 3.3, we then draw non-uniform sampling intervals from a gamma distribution with $\theta = 8.0$ and $k = 1.0$ to obtain a non-uniformly sampled time series of length $N = 2000$ with average sampling rate $\langle dt \rangle$. Finally, we add Gaussian white noise with zero mean and unit standard deviation to the time series.

In order to compare the different phase space reconstruction approaches, we first subsample the high resolution reference solution to have $N = 2000$ points and perform a windowed analysis for the original (x, y, z)-Rössler system as described in subsection 2.4.4 for window widths in $W \in [100, 300]$ with steps $\Delta W = 1$ and offset $dW = 1$. The top panel of figure 3.3 shows the results for the network transitivity where the hatched areas within the contour lines denote analysis results that have been found to show significant anomalies by applying a pointwise significance test

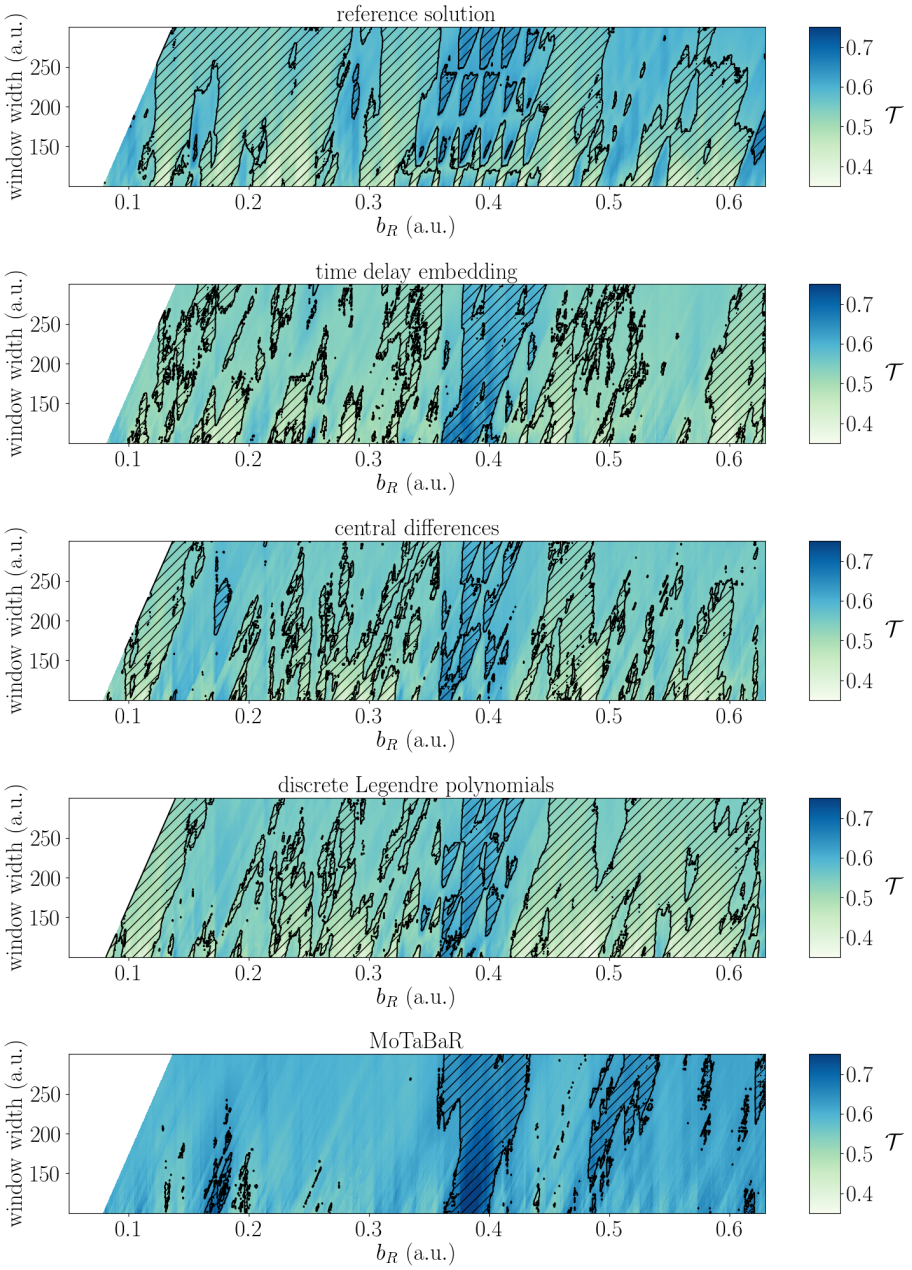

Figure 3.3.: Windowed recurrence network analysis of the noisy, non-uniformly sampled non-stationary Rössler system with significant values of the network transitivity (hatched areas) as derived from random shuffling surrogates (section 2.6) for different phase space reconstruction approaches. From top to bottom: original (x, y, z) Rössler system, time delay embedding, derivative embedding with central differences, discrete Legendre polynomials, and MoTaBaR.

based on random shuffling surrogates with confidence level $s = 0.95$ as described in section 2.6.

We then perform three-dimensional phase space reconstructions from the noisy non-uniformly sampled x-component of the Rössler system by using time delay embedding for linearly interpolated data with delay time $\tau = 5 \langle dt \rangle$ corresponding to the first root of the autocorrelation function of the non-stationary time series, for derivative embedding with central differences, with discrete Legendre polynomials for $p = 4$, and with MoTaBaR for $N_{mtb} = 20$. Analogously to the findings from subsection 3.4.1, we use cubic spline interpolation for the central differences and for the discrete Legendre polynomials, while for MoTaBaR, we use the internal interpolation routine. Also, the coordinates are scaled to have unit variance for all derivative embeddings. The same windowed analysis as for the reference solution is performed and the results for the network transitivity are shown in the lower panels of figure 3.3.

We find that particularly derivative embedding with central differences and discrete Legendre polynomials but also time delay embedding can reproduce the variability of the network transitivity reasonably well. Also, the significantly higher values of the network transitivity around $b_R = 0.4$ are reproduced by all approaches. The results obtained with the MoTaBaR reconstruction generally show much higher values of the network transitivity and do not agree well with the reference results. This is possibly related to the high standard deviation from the mean of the different realisations that was observed for the stationary systems for this approach indicating that the quality of the results is very sensitive to the exact distribution of the sampled time points and the noise.

3.5. Discussion and conclusions

Phase space reconstruction is an important part of non-linear time series analysis. In fact, many methods are based on this concept and their successful application depends on the quality of the available reconstruction. As in real-world applications the mathematical assumptions behind the embedding theorems are not fulfilled, the choice of the phase space reconstruction approach and the corresponding embedding parameters is of great importance. This is particularly true if the data are noisy or non-uniformly sampled. In this chapter, we have studied different approaches of phase space reconstruction by applying them to two paradigmatic model systems and comparing attractor properties of the original and the reconstructed systems for varying embedding dimensions, noise levels, and distributions of the sampling intervals based on recurrence network measures that are related to the attractor geometry. We used the insights to also consider implications of the choice of the reconstruction approach for wRNA.

We did not find any indications that there is one optimal method for phase space reconstruction. The optimal choice of the reconstruction approach and the embedding parameters rather depends on the properties of the studied data. Time delay embedding suffers from conceptual problems for non-uniformly sampled data.

Still, we found that first interpolating the non-uniformly sampled data back to regular sampling using linear interpolation performs well, in some cases, using cubic spline interpolation can further improve the results. Also for wRNA, we found that this approach can reproduce the variability of the network measures of the original system. Nevertheless, independent of the reconstruction approach, interpolating the time series can only give reasonable results if the average sampling rate resolves the relevant time scales of the system's dynamics.

Derivative embedding does not suffer from conceptual problems for non-uniformly sampled data but the robust estimation of higher-order derivatives for noisy data is a challenge. To asses whether this approach can be an alternative to time delay embedding, we compared different methods of estimating derivatives for phase space reconstructions. When estimating the derivatives with central differences, we found that scaling the coordinates to unit variance and the use of cubic spline interpolation yield the best results. But still, this method generally performs worse than the other methods and is, as expected, very sensitive to noise. For the windowed analysis, we observed a good performance of this method. To improve the robustness against noise, we considered the estimation of derivatives using discrete Legendre polynomials. We found that this method performs good in many cases and that again, scaling to unit variance and using cubic spline interpolation should be preferred. Also, the choice of the number of neighbouring points p to each side taken into account for estimating the derivatives should depend on the dimension of the reconstruction, that is, the highest order of the derivatives that needs to be estimated. Finally, we also considered the framework of MoTaBaR for derivative estimation. In some cases, this approach performed good when applying the internal interpolation routine and scaling the coordinates to unit variance, but we also observed higher standard deviations within the different realisations than for the other approaches. This reveals a high sensitivity to the distribution of the sampling intervals and noise that possibly explains the poor performance of the method for the windowed analysis.

Thus, derivative embedding, in particular when using discrete Legendre polynomials to estimate the derivatives, can be an alternative for time delay embedding for non-uniformly sampled and noisy data. In chapter 6, we explore the different phase space reconstruction approaches for analysing real-world palaeoclimate data sets. To further contribute to a better understanding of the dependence of the quality of the phase space reconstruction on the data properties, also the approach of non-uniform time delay embedding has to be taken into account. Future work in this direction is discussed in chapter 9.

Chapter 4.

Areawise significance tests for windowed recurrence network analysis

In this chapter, we generalise the concept of an areawise significance test as introduced in Maraun et al. (2007) for wavelet analysis such that it can be applied in combination with any other analysis approach. This generalised areawise significance test identifies patches of possibly false positive significant points in a classical pointwise significance test by numerically estimating correlations between analysis results which is particularly relevant when applying sliding window approaches. In this case, temporal correlations within the time domain may lead to sequences of significant points instead of isolated significant points. When additionally applying the same analysis for varying analysis parameters, patches of significant points in the (time, parameter)-plane occur independent whether they are true or false positives. By studying the non-stationary Rössler system using windowed recurrence network analysis (wRNA) and windowed scale-specific recurrence network analysis (wssRNA), we demonstrate the potential of the generalised areawise significance test and further contribute to the development of a reliable framework of wRNA.

This chapter is based on, and closely follows, publication P2.

4.1. Introduction

The concepts of detecting and characterising anomalies play an important role in non-linear time series analysis with applications in fields ranging from medicine over finance to climate (Kantz and Schreiber, 2004; Abarbanel et al., 1993; Grassberger et al., 1991). However, the exact definition of an anomaly is not always evident. Indeed, in many applications, anomalies are defined with respect to the properties of sets of surrogate data. That is, a null model is chosen, surrogate data are created, the analysis procedure is applied to the surrogate data sets, confidence bounds are derived from percentiles of the distribution of the surrogate results, and analysis results outside the confidence bounds are referred to as anomalies (compare section 2.6).

In the case of a windowed analysis, or when the same analysis is repeated while varying one or more of the analysis parameters, such as the window width or the embedding delay, multiple testing corrections and possible correlations within the analysis results need to be considered (Miller, 1981; Maraun et al., 2007). Windowed analyses with largely overlapping windows, for example, lead to temporal correlations

of the analysis results which we refer to as intrinsic correlations in the time domain. They manifest as sequences of significant points instead of isolated significant points independent of whether these points are true or false positives. When additionally varying one of the analysis parameters, the same is true within the domain of the results for these parameters, i. e., patches of significant points are observed instead of isolated significant points, which is not taken into account by classical pointwise significance tests. Maraun et al. developed an areawise significance test that can be used to identify such patches of false positive significant points in the wavelet spectrogram and the wavelet coherence by using the reproducing kernel of the wavelet to quantify the intrinsic correlations of the analysis results in the time and the scale domain (Maraun et al., 2007).

A direct generalisation of such an analytic assessment of the intrinsic correlations is not possible because most methods do not possess an equivalent to the wavelet reproducing kernel. Nevertheless, many methods are subject to intrinsic correlations such that a general way to estimate those correlations, along with the introduction of a generalised areawise significance test that can be combined with a larger set of methods, is of great importance to reliably identify anomalies in time series. This necessity has already been recognised, for example, in Franke and Donner (2017) in the context of visibility graphs but, so far, a generalised areawise significance test is lacking.

Here, we put forward a numerical approach that can be used to estimate intrinsic correlations between the results of an arbitrary analysis method. We combine the test with wRNA and wssRNA in order to correct for high rates of significant points when applying a pointwise significance test (as, for example, observed in figure 3.3). Thus, we aim at developing a routine that highlights the most important features in the data and thereby, improves the interpretation of the analysis results for real-world applications.

We first introduce the general idea of the areawise significance test and its formal definition in section 4.2. Then, by studying the non-stationary Rössler system, we apply the test in combination with wRNA and wssRNA in section 4.3. Finally, in section 4.4, we present the main conclusions and provide a short outlook to other possible fields of application and to modifications of the test.

4.2. Areawise significance tests

As argued above, applying sliding window approaches or repeating analyses for varying analysis parameters may lead to patches of false positive significant points within the analysis results due to intrinsic correlations. To correct for this, an areawise significance test can be applied on top of the pointwise significance test. In the case of the areawise test for the wavelet spectrogram introduced in Maraun et al. (2007), a pointwise significant point is areawise significant if it lies within a patch of pointwise significant points that is larger than the reproducing kernel of the wavelet at the corresponding scale. Thus, patches that are smaller than the reproducing kernel of

the wavelet are identified as resulting from random fluctuations and are sorted out by the areawise test.

This idea of the areawise test can be generalised straightforwardly by replacing the concept of the wavelet reproducing kernel with the more universal concept of a decorrelation length of the intrinsic correlations. The main problem is to quantify the scale of decay of the intrinsic correlations, i. e., to estimate the decorrelation length. We here put forward a numerical approach to do so consisting of the following steps:

- First, the domains in which the analysis and the pointwise significance test are repeatedly applied are identified (e. g., the time domain for windowed analyses).
- Second, for each domain, the parameters on which the intrinsic correlations depend, are identified.
- Third, a null model against which the areawise significance test is applied is chosen.
- Fourth, the scale of decay of the intrinsic correlations is numerically estimated by calculating the decorrelation lengths in each domain as a function of the parameters identified in the second step by using surrogate data sets created according to the null model specified in the previous step.
- Finally, the areawise significance test is performed as follows: For each pointwise significant point, get the decorrelation lengths corresponding to the analysis parameters at that point and check whether all neighbouring points within the range of the decorrelation lengths are also pointwise significant. The point is areawise significant if this is the case, otherwise it is not areawise significant.

To be precise, we denote the time series that we want to analyse as $\vec{x}(t)$ and identify the domains d_i, $i = 1, \ldots, n$ as the domains in which the analysis is repeatedly applied (e. g., the time domain for windowed analyses). In the following, we only consider the case $n = 2$ but a generalisation to more domains is straightforward. The analysis results of the time series $\vec{x}(t)$ are stored in the matrix $\mathbf{Q} = (Q_{k_1,k_2})$ with $k_1 \in [1, N_1]$ and $k_2 \in [1, N_2]$ where $N_{1,2}$ is the number of parameter values analysed in the corresponding domain. The vectors $\vec{P}^{(j)} = \left(P_1^{(j)}, \ldots, P_{N_j}^{(j)}\right)$ $(j = 1, 2)$ contain the corresponding values of the analysis parameters. The results of the pointwise significance test of the analysis results are given in a binary matrix $\mathbf{S}^{\mathrm{pw}}$ with $S^{\mathrm{pw}}_{k_1,k_2} = 1$ if the result Q_{k_1,k_2} is pointwise significant and $S^{\mathrm{pw}}_{k_1,k_2} = 0$ if it is not pointwise significant.

Then, we identify the parameters p_j, $j = 1, \ldots, N_p$, on which the intrinsic correlations depend. We here restrict ourselves to the case $N_p = 1$ and denote $p_1 = p$. Again, the test can easily be generalised to higher values of N_p.

Before numerically assessing the intrinsic correlations, we need to choose a null model. From this null model, N_{s} sets of surrogate data are created and analysed over the range of analysis parameters $\vec{P}^{(1)}$ and $\vec{P}^{(2)}$. The decorrelation length can then be determined for each domain d_i by calculating correlations between the analysis

results for different analysis parameters and choosing the value of the parameter at which the correlations fall below $1/\mathrm{e}$ as a preliminary estimate of the decorrelation length l_{d_i}. By repeating this procedure for different values of the parameter p, we obtain the decorrelation lengths as a function of this parameter. Fitting the mean of the different realisations with respect to a linear model

$$l_{d_i} = m_{d_i} p + n_{d_i}, \tag{4.1}$$

gives the final estimate of the decorrelation length as a function of p in the corresponding domain d_i where the m_{d_i} denote the slope and the n_{d_i} the intercept of the linear fits. We stress that even though there is no particular reason to prefer a linear model over a more general fitting model, we here only consider this linear model for the sake of simplicity and, because, in many cases, it seems to capture the behaviour of the decorrelation lengths reasonably well (compare section 4.3).

A pointwise significant point in $\mathbf{Q}$ corresponding to $S^{\mathrm{pw}}_{k_1,k_2} = 1$ is said to be areawise significant, i. e., has the entry $S^{\mathrm{aw}}_{k_1,k_2} = 1$ in the areawise significance matrix $\mathbf{S}^{\mathrm{aw}}$, if the relation

$$\sum_{i=k_1-(l_{d_1}/2-1)}^{k_1+(l_{d_1}/2-1)} \sum_{j=k_2-(l_{d_2}/2-1)}^{k_2+(l_{d_2}/2-1)} S^{\mathrm{pw}}_{i,j} = (l_{d_1}-1)(l_{d_2}-1), \tag{4.2}$$

holds. That is, a point is areawise significant if all points within the rectangle of side lengths $l_{d_1}-1$ and $l_{d_2}-1$ centred at the point Q_{k_1,k_2} are pointwise significant. We use this rectangular shape because it has the least implicit assumptions about the decay of correlations in the different domains. In fact, the rectangular shape corresponds to the case where the decays of correlations in d_1 and d_2 are mutually independent. If an analytical treatment of the decay of correlations is available, the information can in principle be used for determining an alternative shape to define the environment of neighbouring points that have to be pointwise significant for the considered point to be areawise significant.

For this type of areawise significance test, it is possible to derive confidence levels of the test by using surrogate data. For the confidence levels, we use the opposite point of view as Maraun et al. who first choose a confidence level $1-\alpha_{\mathrm{aw}}$ and then scale the reproducing kernel of the wavelet such that the number of pointwise significant points A_{pw} and the number of areawise significant points A_{aw} are related by $A_{\mathrm{aw}} = \alpha_{\mathrm{aw}} A_{\mathrm{pw}}$ (Maraun et al., 2007). Here, we estimate the decorrelation lengths as specified above for the chosen null model and then apply the areawise significance test to analysis results obtained from data corresponding to the null model. The average fraction of areawise and pointwise significant points in the surrogate results is then used to determine the areawise confidence level s_{aw} as

$$s_{\mathrm{aw}} = 1 - \left\langle \frac{A_{\mathrm{aw}}}{A_{\mathrm{pw}}} \right\rangle. \tag{4.3}$$

That is, our approach is fully data-driven and neither fixes the number of resulting areawise significant points nor requires to manually set an areawise confidence level. The total confidence level of the analysis s_{tot} is then given as the product of the pointwise and the areawise confidence levels $s_{\text{tot}} = s_{\text{pw}} s_{\text{aw}}$.

4.3. Results for the non-stationary Rössler system

We now apply the areawise significance test in combination with wRNA and wssRNA to study the non-stationary Rössler system already introduced in chapter 3. That is, we consider the system defined by the set of ordinary differential equations (2.2) with fixed parameters $a_R = 0.2$ and $c_R = 5.7$, time varying parameter $b_R(t) = b_{R,0} + \Delta b_R(t - t_0)$ with $b_{R,0} = 0.02$ and $\Delta b_R = 0.001$, and initial conditions $(x_0, y_0, z_0) = (0.5, 0.0, 0.0)$. The reference solution is obtained by integrating the system for times $t \in [0, 630]$ with resolution $dt = 0.1$. We then discard the first 300 points and take every third point of the x-component to get the final time series of length $N = 2000$. For the analysis, we normalise the time series to have zero mean and unit variance.

The resulting time series as a function of the time-varying parameter b_R and the corresponding bifurcation diagram are shown in figure 4.1. To obtain the bifurcation diagram, for every value of b_R, we integrated the system for $10,000$ time steps and, for the last $2,500$ time steps, recorded the values of the x-component when the sign of the y-component changed from positive to negative. Like this, the bifurcation diagram characterises the dynamics of the stationary Rössler system for the corresponding values of the parameter b_R, while the time series of the x-component represents the transient Rössler system and thus, does not necessarily always reproduce the dynamics of the stationary system. Still, we use this bifurcation diagram as reference and compare the results of our analysis framework to it.

That is, we expect to observe episodes of more and less chaotic dynamics as marked by the vertical lines in the bifurcation diagram in terms of significantly low and high values of the network transitivity. We particularly emphasise that detected significant anomalies do not denote transition regimes between more and less chaotic dynamics. This is because we use random shuffling surrogates for the pointwise significance test which, due to the random shuffling, consist of state vectors representing both types of dynamics. Hence, only periods that are characterised by either more or less chaotic dynamics will be identified as significant.

4.3.1. Windowed recurrence network analysis

For wRNA, we follow the approach described in subsection 2.4.4 using uniform time delay embedding to reconstruct the higher-dimensional phase space of the system from the x-component. The delay time is chosen to be $\tau = 5\langle dt \rangle$ corresponding to the first root of the autocorrelation function and the embedding dimension is determined to be $m = 3$ as suggested by the false nearest neighbour criterion. We vary the window width in the interval $W \in [100, 300]$ with step size $\Delta W = 1$ and offset $dW = 1$, that is, we have largely overlapping windows. The recurrence threshold ϵ is set by fixing

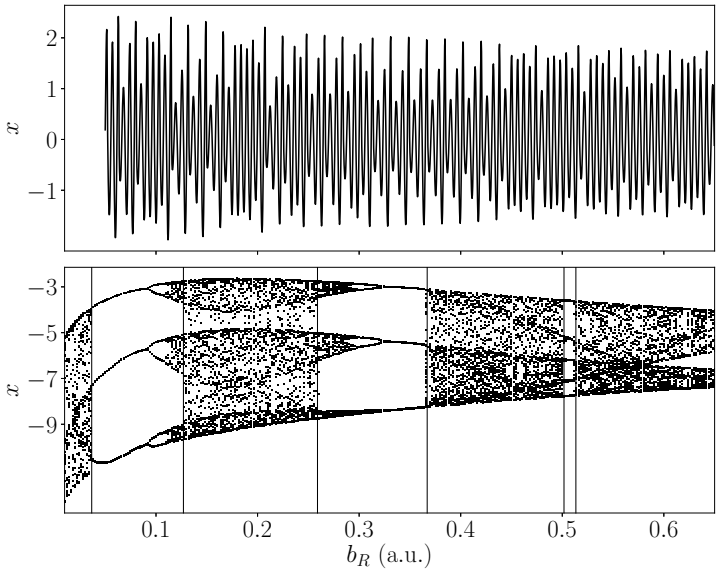

Figure 4.1.: Time series of the x-component of the non-stationary Rössler system with time-varying parameter b_R (top) and bifurcation diagram for the stationary Rössler system for the different values of b_R (bottom). The vertical lines in the bifurcation diagram denote alternating periods of more and less chaotic dynamics. Reproduced with permission from P2.

a recurrence rate of $RR = 0.05$ and distances in phase space are measured with the maximum norm. The pointwise significance test is performed based on random shuffling surrogates with a confidence level of $s_{\mathrm{pw}} = 0.95$.

Before applying this analysis framework to the non-stationary Rössler system, we have to define the areawise test for it by following the procedure described in section 4.2. As domains in which the analysis is repeatedly applied, we identify the time and the window width domain, i. e., $d_1 = t$ and $d_2 = W$. As the intrinsic correlations are assumed to be stationary, we identify the window width as the parameter on which the intrinsic correlations depend, that is, $p = W$.

Next, we have to choose a null model against which we want to test the analysis results. We here consider three different null models, Gaussian white noise (GWN), an autoregressive process of order 1 (AR(1) process), and a data-adaptive routine employing iterative amplitude-adjusted Fourier transform (iAAFT) surrogates. The surrogate generation routines are described in section 2.6. Every null model shares some properties of the original data. For GWN, this is the mean and the standard deviation of the distribution of the time series. For the iAAFT routine, we have the amplitude distribution and the linear correlation structure, while the parameters of the AR(1) process are fitted to the data. Thus, when testing against these null models, we test whether the original data show structures that are not apparent in the surrogate data corresponding to the different null models. In particular, using

Table 4.1.: Data properties and and fitting parameters for the AR(1) model of the non-stationary Rössler system (for a description of the parameters see section 2.6).

μ	σ	$x(0)$	c	α	σ_{ϵ_t}
0.0	1.0	0.1897	0.0	0.9427	0.3337

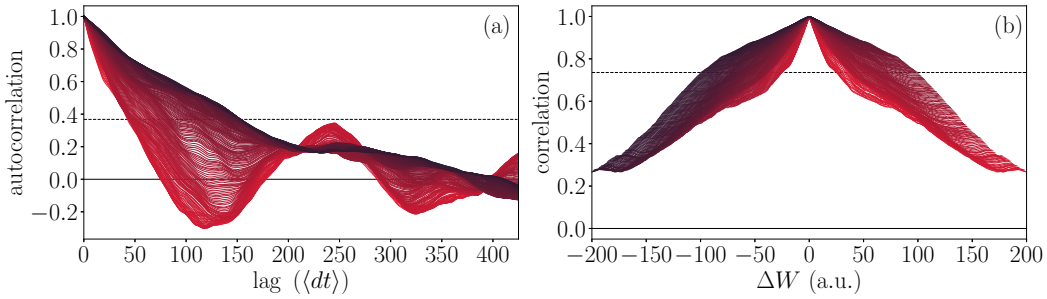

Figure 4.2.: (a) Lagged autocorrelation function of the transitivity in the time domain and (b) correlation between the transitivity results in the window width domain for different values of the window width (W increasing from light to dark red) for one of the N_s realisations of GWN. The dashed lines denote the value of $1/\mathrm{e}$ and $2/\mathrm{e}$, respectively (see text). Reproduced with permission from P2.

this hierarchy of null models from uncorrelated noise over short term correlated noise to random data with identical amplitude distribution and linear correlation structure can help to identify the source of the non-stationarity in the data. In principle, this hierarchy could be complemented with additional null models that possibly also take into account non-linear correlation structures within the data (e. g. twin surrogates (Thiel et al., 2006)) or long-range persistence which has for example been observed in climate records and climate model simulations (Østvand et al., 2014). However, we do not consider additional null models in this work.

To assess the intrinsic correlations of the analysis framework, we create $N_s = 100$ realisations for each of the different null models with parameters of the GWN and AR(1) surrogates as displayed in table 4.1. Each surrogate realisation is embedded using uniform time delay embedding with delay time chosen according to the first root of the autocorrelation function and embedding dimension $m = 3$. We then apply the wRNA as described above to all surrogate data sets.

To quantify the intrinsic correlations in the time domain, we consider the resulting network transitivity $\mathcal{T}$ as a function of time for a fixed value of the window width W and calculate the lagged autocorrelation function up to a lag of $(N - W_{\max})/2$. For a specific lag l, this means calculating the correlation between the transitivity values of two networks consisting of $W - l$ identical and l different nodes. This is then repeated for all values of W. The left hand side of figure 4.2 exemplarily shows the lagged autocorrelation functions for the different window widths for one of the

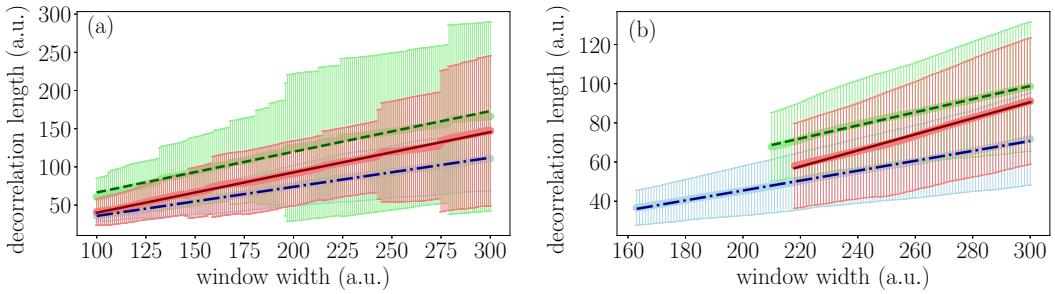

Figure 4.3.: Mean (points), standard deviations (error bars), and linear fits (lines) of the decorrelation lengths as a function of the window width W for (a) correlations in the time domain of the wRNA results and (b) correlations in the window width domain for the non-stationary Rössler system using the three different null models: blue, dash-dotted: GWN; green, dashed: AR(1) process; red, solid: iAAFT null model. Reproduced with permission from P2.

realisations of GWN. The decorrelation length as a function of the window width in the time domain is then given as those values of the lag where the autocorrelation function falls below $1/\mathrm{e}$. The mean and the standard deviation of the decorrelation length and the corresponding linear fit are shown in figure 4.3. Table 4.2 contains the fitting parameters and the values of the coefficient of determination R^2 of the linear fits for the different null models. We observe that the decorrelation length as a function of the window width is well approximated by the linear fit, which is also supported by the high values of R^2.

To assess the correlations in the window width domain, we calculate the Pearson correlation between the network transitivity as a function of time for a specific value of the window width W and the time series of network transitivity of the other (preceding and following) window widths. Those forward and backward correlations for varying starting values of W are visualised on the right hand side of figure 4.2. We see that the forward and backward correlations vary symmetrically and choose to use the backward correlations. To estimate the decorrelation length as a function of the window width we use the value of ΔW at which the correlation falls below $2/\mathrm{e}$ because otherwise, we do not get enough values of the decorrelation length to perform a linear fit as most correlations do not fall below $1/\mathrm{e}$. The right hand side of figure 4.3 shows the mean, standard deviation, and linear fit of the decorrelation time as a function of the window width for the different null models. The corresponding fitting parameters can be found in table 4.2. Again, we observe a good correspondence of the results with the linear fitting model. Thus, for wRNA, the linear fitting approach seems to be well justified.

Given the fit parameters, we can now apply the areawise test as defined in section 4.2 and evaluate the confidence levels of the test for the different null models. The resulting confidence levels are given in the last columns of table 4.2. We observe very high confidence levels for GWN and slightly lower confidence levels for the AR(1) and the iAAFT null models. These lower values may be related to the choice of backward

Table 4.2.: Parameters and coefficients of determination of the linear fits of the decorrelation length as a function of the window width for the network transitivity of wRNA and corresponding significance levels for the different null models in the time and the window width domain.

null model	domain	m	n	R^2	s_{aw}	s_{pw}	s_{tot}
GWN	time	0.3813	−2.364	0.9980			
GWN	W	0.2527	−5.081	0.9991	0.99	0.95	0.94
AR(1)	time	0.5325	13.30	0.9889			
AR(1)	W	0.3348	−1.631	0.9976	0.88	0.95	0.84
iAAFT	time	0.5276	−12.74	0.9976			
iAAFT	W	0.4102	−32.54	0.9967	0.90	0.95	0.86

correlations and the $2/\mathrm{e}$ threshold in the window width domain leading to a bias toward lower decorrelation lengths, but, taken the results for all null models together, we think that these choices for the areawise test are still justifiable.

Finally, we apply the areawise test for the different null models to the analysis results of the non- stationary Rössler system. Figure 4.4 displays the analysis results in combination with the pointwise and the areawise significance tests. First, we observe that applying the areawise test reduces the number of significant points considerably. Also, the results for the different null models agree on the regions in the (time, window width)-plane in which areawise significant points are present even though the sizes of the areawise significant patches differ slightly for the different null models.

When comparing the results to the expected dynamical behaviour of the system from the bifurcation diagram (figure 4.1), we see that in the regime of $b_R \in [0.13, 0.26]$ where more chaotic dynamics can be expected, the network transitivity indeed shows patches of significantly low values corresponding to higher-dimensional dynamics. This is followed by an increase in the network transitivity for $b_R > 0.26$ corresponding to lower-dimensional dynamics. Then we observe alternating values of low and high values of the network transitivity that are not perfectly consistent with the expectations from the bifurcation diagram. In particular, we find an areawise significant patch of low values of the network transitivity for small to intermediate window widths after $b_R = 0.3$ though in this regime of the parameter, we would expect lower-dimensional dynamics from the bifurcation diagram. The regime $b_R \in [0.50, 0.51]$ in which we also expect lower-dimensional dynamics shows corresponding higher but non-significant values of the network transitivity. Finally, for $b_R > 0.51$, we observe the expected decrease of the values of the network transitivity and also identify areawise significant patches of low values of the network transitivity for small window widths.

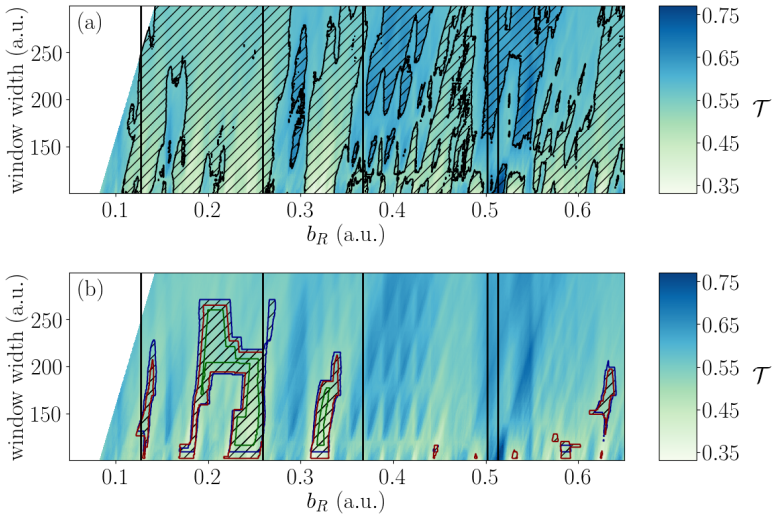

Figure 4.4.: Transitivity $\mathcal{T}$ of wRNA (color coded) of the non-stationary Rössler system with (a) pointwise significance test using random shuffling surrogates and (b) areawise significance test (hatched contours). The test results for the GWN null model are shown by dark blue, the AR(1) null model by dark green and the iAAFT null model by dark red contours. The vertical lines indicate the different regimes of more and less chaotic dynamics as identified in the bifurcation diagram of the stationary system (figure 4.1). Reproduced with permission from P2.

Thus, we find that the variability of the network transitivity in many cases follows the expectations from the bifurcation diagram of the stationary Rössler system. Deviations from the expectations can probably be attributed to the transient nature of the analysed time series which may cause bifurcations to be delayed or missed (Donges et al., 2011a).

For the average shortest path length within the network, we observe similar results as for the network transitivity (see appendix B.1) even though the confidence level of the areawise significance test for the average shortest path length is considerably lower for the AR(1) null model and the iAAFT null model shows less areawise significant points. In combination with the analytical relationship between the network transitivity and the dimensionality of the system's dynamics (Donner et al., 2011b), we think that the network transitivity should be preferred when inferring information on the dynamics of a system with wRNA.

4.3.2. Windowed scale-specific recurrence network analysis

To study the dynamics of the non-stationary Rössler system in more detail and to show that the areawise significance test can be combined with different methods, we now turn to wssRNA which can be used to study the system's dynamics at different time scales separately.

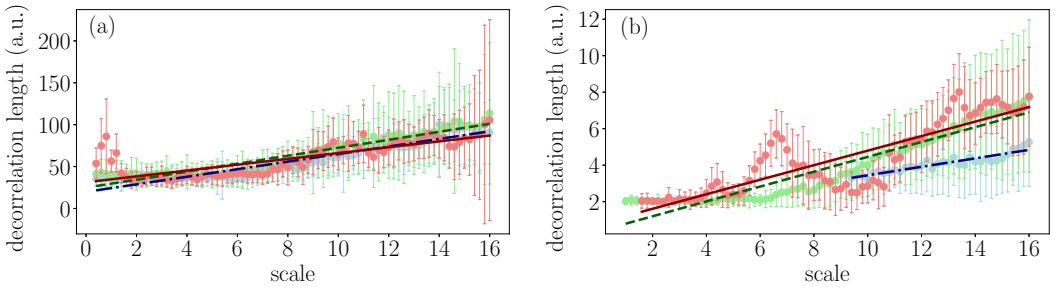

Figure 4.5.: Same as in figure 4.3 but for wssRNA and correlations in the time and the scale domain as a function of the scale. Reproduced with permission from P2.

That is, we apply the areawise test in combination with wssRNA as described in section 2.5 for scales $s \in [0.4, 16]$ with step size $\Delta s = 0.2$ to the non-stationary Rössler system. The window widths of the windowed analysis are chosen corresponding to equation (2.23), the offset of the windowed analysis is given as $dW = 1$, and the pointwise significance test is again based on random shuffling surrogates with confidence level $s_{\mathrm{pw}} = 0.95$.

For the areawise test, we identify the time and the scale as domains in which the analysis is repeatedly applied, that is, we have $d_1 = t$ and $d_2 = s$. With the same argument as above, we expect the intrinsic correlations to be only dependent on the chosen scale of the analysis, i. e., $p = s$. We again use the hierarchy of null models consisting of GWN, the AR(1) process, and the iAAFT null model and follow the same numerical procedure in order to estimate the decorrelation lengths as a function of the scale. The threshold for finding the decorrelation lengths is set to $1/\mathrm{e}$ for both domains. Figure 4.5 shows the mean and standard deviation of the different null model realisations and the linear fits of the decorrelation lengths as a function of the scale for the two domains. The fitting parameters and the confidence levels of the areawise test are given in table 4.3. In the time domain, we see that the results of the decorrelation length as a function of the scale are very similar for the different null models. Also, we observe that for wssRNA, the linear fitting model is not as appropriate as for wRNA which is particularly true in the scale domain and for the iAAFT null model, evident also in the low values of the coefficient of determination R^2. Still, with this fitting approach, we obtain high confidence levels and thus stick to the linear model and leave more general fitting models for future work.

The results of the analysis are visualised in figure 4.6. We again see that applying the areawise test reduces the number of significant points of the analysis results. The patches of areawise significant points obtained with the AR(1) and the iAAFT null model are very similar, while there are some additional small patches of areawise significant points for the GWN null model. As the iAAFT routine shares more properties of the original data than the other models, we will concentrate on the results for this model in the following. We observe small patches of significantly low values of the network transitivity for smaller scales, in particular, in the parameter

Table 4.3.: Same as in table 4.2 but for wssRNA and correlations in the time and the scale domain as a function of the scale.

null model	domain	m	n	R^2	s_{aw}	s_{pw}	s_{tot}
GWN	time	4.516	19.74	0.8836			
GWN	scale	0.2321	1.124	0.8529	0.93	0.95	0.88
AR(1)	time	4.757	24.86	0.9147			
AR(1)	scale	0.4070	0.3845	0.9023	0.97	0.95	0.92
iAAFT	time	3.483	31.30	0.6361			
iAAFT	scale	0.3982	0.8128	0.7396	0.95	0.95	0.90

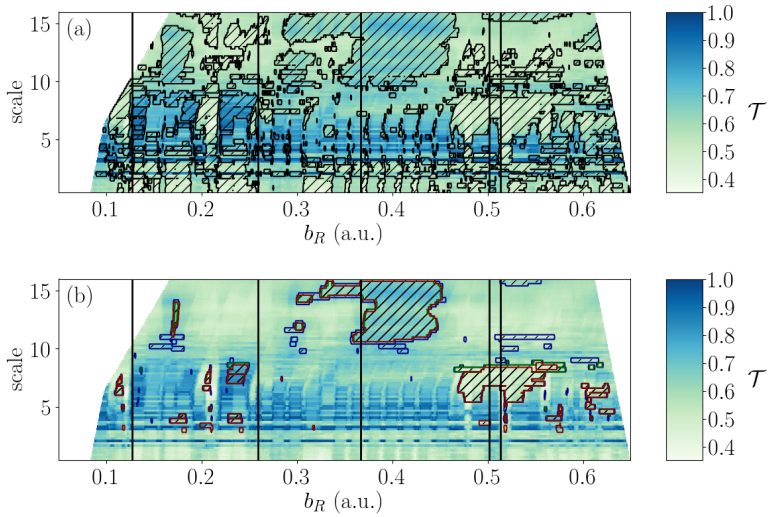

Figure 4.6.: Same as in figure 4.4 but for wssRNA for varying scales. Reproduced with permission from P2.

regimes $b_R \in [0.13, 0.26]$ and $b_R > 0.51$. Also, we observe a patch of significantly low values of the network transitivity at intermediate scales for $b_R \in [0.48, 0.55]$ reflecting the higher-dimensional dynamics in this regime and showing that for these scales in the transient time series, the short interval $b_R \in [0.50, 0.51]$ of expected lower-dimensional dynamics is missed. For $b_R \in [0.37, 0.45]$ we observe a significant patch of high values of the network transitivity for intermediate to large scales, starting already around $b_R = 0.3$ for large scales possibly resulting from the expected low-dimensional regime for $b_R \in [0.26, 0.37]$.

Thus, wssRNA reveals that the dynamics at different scales vary and higher-dimensional dynamics are happening at smaller scales, while lower-dimensional dynamics seem to be related to the variability of the system at larger scales. Again, the results of the average path length are comparable to those of the network transitivity (see appendix B.2). Like this, wssRNA can complement results obtained with traditional wRNA and should be used as an additional valuable tool to analyse time series from dynamical systems

4.4. Discussion and conclusions

Identifying and characterising dynamical anomalies in time series is an important task as it provides information about the dynamics of the system under study. Nevertheless, the concept is only useful when a reliable framework for defining an anomaly and quantifying its significance is available. In particular, when pursuing a sliding window approach or when some analysis parameter is varied, multiple testing and intrinsic correlations within the analysis results complicate the definition of an anomaly and its significance.

In this chapter, we introduced an areawise significance test that can be combined with an arbitrary analysis method and identifies patches of false positive significant analysis results that appear due to intrinsic correlations within this method. The idea of the test is based on that of the areawise significance test introduced in Maraun et al. (2007) but is not restricted to wavelet analyses. Instead, a numerical approach independent of the underlying analysis method is pursued to estimate the decorrelation length of the intrinsic correlations. For this, the domains in which the analysis is repeatedly applied and the parameters on which possible intrinsic correlations depend have to be identified. Then, a null model has to be chosen and the decorrelation length of the intrinsic correlations of the method as a function of the dependent parameters can be numerically estimated using surrogate data sets corresponding to the null model. A pointwise significant point is considered to be areawise significant if it lies within a patch of pointwise significant points that is larger than the decorrelation lengths with respect to the analysis parameters of the considered point. Moreover, by using surrogate data, it is possible to derive confidence levels of the areawise significance test.

We here considered three distinct null models sharing different properties with the original data. First, we had a look at the case of uncorrelated GWN with the

same mean and standard deviation as the original data. Second, we considered an AR(1) process, i. e., short-term correlated noise where the AR(1) model parameters were fitted to the original data. Third, we used a data-adaptive iAAFT null model, that is, these surrogate data sets have the same amplitude distribution and linear correlation structure as the original data. We studied a non-stationary Rössler system and combined the areawise significance test with wRNA and wssRNA in order to obtain information about the system's dynamics.

The results from the network transitivity of wRNA are in many cases consistent with the expected results for the corresponding stationary Rössler system. Deviations possibly result from the transient nature of the analysed time series. When additionally applying wssRNA, we found that higher-dimensional dynamics results from the variability at smaller scales, while lower-dimensional dynamics results from the system's variability at larger scales. Corresponding results can also be found for another network measure, namely the average shortest path length in the network (appendix B).

For both methods, the areawise significance test considerably reduced the number of pointwise significant analysis results and thus, succeeded in identifying patches of pointwise significant points that are probably false positives. We expect this to hold also when combining the approach with other analysis methods, such as, for example, for analyses using climate networks (Tsonis et al., 2006; Donges et al., 2009; Radebach et al., 2013; Wiedermann et al., 2016) where often a windowed approach is pursued and also the size of the window width is sometimes varied.

Of course, modifications of the areawise significance test presented here are possible. In particular, the linear fitting model used to get an estimation of the relationship between the decorrelation lengths and the parameters on which intrinsic correlations within the analysis results depend can be replaced by a more general fitting model. Also, when some understanding of the dependence of the correlations in the different domains in which the analysis is repeatedly applied is available, this can be used to replace the rectangular shape defining the neighbourhood for the areawise significance test accordingly. If required, different null models, possibly sharing also some non-linear properties of the original data, can be considered for both the pointwise and the areawise significance test to identify the source of non-stationarity within the data.

We think that this areawise significance test has a great potential for improving the identification of significant anomalies in time series of many different types and like this, also the interpretation of obtained dynamical anomalies as only the most important features of the data are brought out. Thus, the introduction of the test contributes not only to the further development of non-linear time series analysis approaches in general, but also to our framework of wRNA in particular.

Chapter 5.

Summary: Development of analysis framework

This first part of the thesis dealt with the introduction and development of an analysis framework based on windowed recurrence network analysis (wRNA) and windowed scale-specific recurrence network analysis (wssRNA) that can be used to reliably detect and characterise dynamical anomalies in time series. In particular, we focused on experimentally measured time series representing a system whose dynamics are not accessible analytically.

After a general introduction to non-linear time series analysis, we established the theory on which this thesis is based in chapter 2. That is, we (i) studied the problem of phase space reconstruction to recover the dynamics of a higher-dimensional system from a univariate measured time series, (ii) explored the concepts of recurrence network analysis and scale-specific recurrence network analysis with particular focus on sliding window approaches, and (iii) entered the field of significance testing using surrogate data.

To further study and develop the existing framework of wRNA, we compared the methods of uniform time delay embedding and derivative embedding for different ways to estimate the derivatives for the case of non-uniformly sampled and noisy data in chapter 3. Such data pose a particular challenge to the reconstruction of the system's phase space as time delay embedding is not defined for non-uniformly sampled data and derivative embedding suffers from noise amplification for higher-dimensional embeddings. We found that using linear interpolation in combination with uniform time delay embedding performs reasonably well in many cases and its performance can sometimes be improved by using cubic spline interpolation. For derivative embedding, we found that estimating the derivatives by using the relation between the derivatives of a time series and the discrete Legendre polynomials performs best compared to the other ways of derivative estimation. In some cases, this approach can be a useful alternative to time delay embedding.

We then considered the problem of defining anomalies and their significance in wRNA and wssRNA in chapter 4. When applying sliding window approaches or when repeating an analysis for a set of analysis parameters, intrinsic correlations within the analysis results complicate the detection of anomalies as in such cases, patches of significant points instead of isolated significant points appear irrespective of whether they are true or false positives. Based on a numerical estimation of the decorrelation

length of the intrinsic correlations using surrogate data with respect to a specified null model, we introduced an areawise significance test that can identify patches of false positive significant analysis results. When applying the test in combination with wRNA and wssRNA to study a non-stationary Rössler system, we found that the areawise significance test is indeed able to considerably reduce the number of significant points. Also, using the network transitivity to infer information on the dimensionality of the system's dynamics, we observed good agreement with the expected behaviour of the corresponding stationary system. Deviations may result from the transient nature of the studied time series. Thus, we are confident that the detected areawise significant anomalies quantify the system's dynamics and that the areawise test improves the reliability of the framework of wRNA.

For completeness, we here summarise the analysis framework as we think it is most suitable for the detection of dynamical anomalies in real-world time series. For this, we assume that the available time series $x(t)$ is univariate and represents the dynamics of some higher-dimensional dynamical system.

- The first step in the analysis of the time series $x(t)$ is the reconstruction of the higher-dimensional phase space of the underlying dynamical system. For this, uniform time delay embedding or derivative embedding when estimating the derivatives with discrete Legendre polynomials is used. For time delay embedding, the delay time is estimated by the first root of the autocorrelation function or the first minimum of the mutual information. For the discrete Legendre polynomials, the number of neighbours to each side taken into account for estimating the derivatives is chosen of the order of the embedding dimension. The embedding dimension is determined with the help of the false nearest neighbour method corrected for autocorrelation effects.

- In the second step, the embedded time series is analysed with wRNA and wssRNA for varying window widths and scales, respectively. The threshold for the recurrences is chosen adaptively by fixing a recurrence rate and distances in phase space are calculated using the maximum norm. The resulting network transitivity is used to characterise the dimensionality of the system's dynamics.

- Then, to test whether the values of the network transitivity actually show dynamical anomalies, a pointwise significance test is applied. The surrogates can, for example, be random shuffling surrogates, but any other appropriate null model may be chosen.

- Finally, to correct for intrinsic correlations of the windowed analysis for varying window widths and scales, the areawise significance test is applied with respect to a chosen null model and the confidence level of the areawise test are determined. We recommend to use a data-adaptive null model such as iAAFT surrogates or to use a hierarchy of null models.

- Areawise significant values of the network transitivity then characterise dynamical anomalies in terms of significantly higher- or lower-dimensional dynamics compared to the dynamics of the null models.

In the second part of the thesis, we apply this analysis framework to palaeoclimate proxy time series. With this, we want to assess how well wRNA is suited to detect dynamical anomalies in past climate variability from data of different palaeoclimate archives. However, the framework can in principle be applied to any type of time series data.

Part II.

Application of analysis framework

In the second part of the thesis, we apply the framework of windowed (scale-specific) recurrence network analysis to detect dynamical anomalies in time series from different palaeoclimate archives. That is, in chapter 6, we analyse four real-world data sets to infer information on climate variability in North and South America in the last two millennia. Then, in chapter 7, to gain some more insights on the implications of the type of archive and its local boundary conditions for the results obtained with windowed recurrence network analysis, we employ the framework of proxy system modelling to different artificial climate input time series with well-known properties. In chapter 8, we summarise the main conclusions of this second part of the thesis.

Chapter 6.

Analysing palaeoclimate data with windowed recurrence network analysis

In this chapter, we turn to the problem of characterising past climate variability from palaeoclimate proxy data. In a first step, we introduce the main drivers of the climate of the last two millennia and review associated episodes of outstanding climate conditions. We also establish the main palaeoclimate archives that are studied within the thesis and present exemplary data sets from each archive. We then use the analysis framework of windowed recurrence network analysis (wRNA) and windowed scale-specific recurrence network analysis (wssRNA) to analyse these exemplary real-world palaeoclimate proxy time series from the different archives. With this, we want to highlight the potentials and limitations of the analysis approach for real-world data. Additionally, we aim at taking a first step towards a systematic characterisation of non-linear climate variability in North and South America.

The results in this chapter are partially based on the results from publications P1 and P2.

6.1. Introduction

The analysis of palaeoclimate data offers the possibility to gain information about past climate variability. Apart from stochastic internal variation, climate variability is subject to external forcing with the most important factors being changes in the orbital parameters, solar radiation, explosive volcanism, and the greenhouse gas concentration in the atmosphere, all operating on different time scales (Ruddiman, 2001). In the last two millennia, insolation changes, volcanism, and the increasing concentration of greenhouse gases have been identified as the main drivers of climate change (Crowley, 2000; Mann et al., 2009; Luterbacher et al., 2016).

During the Roman high period, wet and warm summers have been found to prevail in Europe, coining the term Roman Warm Period (RWP) for times 200 B. C. to 150 AD (Bianchi and McCave, 1999; Büntgen et al., 2011). Subsequently, increased variability in climate from approximately $250 - 550$ AD has been observed (Büntgen et al., 2011). Decreasing solar activity in combination with an extreme volcanic eruption about 536 AD and a cluster of explosive eruptions in $536 - 547$ AD led to the term Late Antique Little Ice Age (LALIA) for the period $550 - 660$ AD (Sigl et al., 2015; Büntgen et al., 2016). Wet and warm summers related to stable atmospheric

conditions, particularly pronounced in central and northern Europe, again occurred at the medieval high period such that the time span $900 - 1250$ AD has been termed Medieval Climate Anomaly (MCA) (Hughes and Diaz, 1994; Mann et al., 2009; Büntgen et al., 2011; Luterbacher et al., 2016). Volcanic forcing and decreasing solar activity then initiated the Little Ice Age (LIA) which consisted of several periods of decreased temperature around $1400 - 1750$ AD (Briffa et al., 1998; Crowley, 2000; Mann et al., 2009). Finally, with the beginning of the industrial revolution, increasing greenhouse gas concentrations after 1850 AD led to the 20th century warming, also referred to as the current warm period (CWP) (Crowley, 2000; Bird et al., 2011).

In fact, most of these studies have focused on Europe or the Northern Hemisphere. Even within this region, the timing and the imprint of the described episodes has been found to vary significantly depending on the exact location (Hughes and Diaz, 1994; Mann et al., 2009). Global temperature reconstructions identify a long-term cooling trend until the late 19th century in most regions worldwide, while the multi-decadal to centennial variability differs within the different regions and is more similar within one hemisphere than between the hemispheres (PAGES2k-Consortium, 2013). Also, no globally synchronous MCA or LIA could be identified. Still, warmer conditions are evident in the Northern Hemisphere between $830 - 1100$ AD and in the Southern Hemisphere between $1160 - 1370$ AD with the transition to cooler conditions earlier in the Arctic, Asia, and Europe, and later in North America and the Southern Hemisphere (PAGES2k-Consortium, 2013). Recent global temperature reconstructions show warm temperature anomalies in 1320 AD, 1420 AD, 1560 AD, and 1780 AD, while cold anomalies are identified for 1260 AD, 1450 AD, and 1820 AD (Neukom et al., 2019).

For South America, a strengthening of the South American monsoon system has been found and attributed to the LIA for times $1600 - 1820$ AD, while a weakening was observed for times $900 - 1100$ AD and since approximately 1850 AD, possibly corresponding to imprints of the MCA and the CWP in this region (Bird et al., 2011; Vuille et al., 2012; Novello et al., 2016). With respect to the vulnerability of South America to recent climate change (Villalba et al., 2009), a more detailed assessments of South American climate variability is of great importance and also contributes to a better understanding of the climate system.

In particular, the use of non-linear methods to study past climate variability can yield valuable insights. Applying our framework of wRNA to study four palaeoclimate proxy time series from North and South America thus serves as a starting point for systematically characterising past non-linear climate variability on the American continents. We start by introducing the studied archives and exemplary data sets in section 6.2, then present the results of our analysis in section 6.3, and finally summarise our main conclusions in section 6.4.

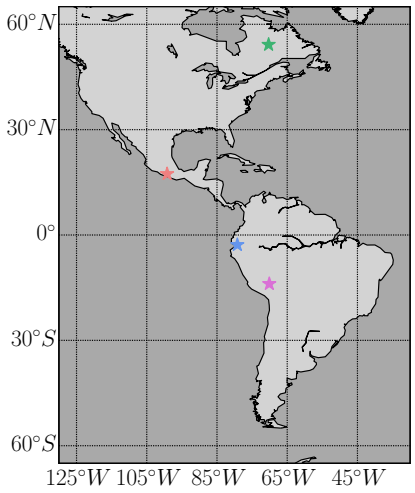

Figure 6.1.: Locations of the archives providing the different proxy time series used in this chapter. The location of the tree ring archive is denoted in green, of the lake sediment archive in blue, of the speleothem archive in red, and of the ice core archive in magenta.

6.2. Palaeoclimate archives and proxy data

6.2.1. Tree rings

Many trees form annual rings whose characteristics depend on environmental factors such as temperature and soil moisture (Bradley, 2015b). In fact, those trees constitute the most important palaeoclimate archive for temperature reconstructions of the past millennium (Bradley, 2015b; IPCC, 2013; St. George, 2014; St. George and Esper, 2019). Still, obtaining and interpreting chronologies from tree ring measurements poses many challenges. For example, it has been shown that the quality of the available data sets varies in terms of data homogeneity, sample replication, growth coherence, chronology development, and climate signal (Esper et al., 2016). Also, modern accelerated tree growth might lead to biases in palaeoclimate reconstructions that need to be accounted for (Scharnweber et al., 2019).

We study a local tree ring width index chronology from eastern Canada (Gennaretti et al., 2014). It is compound of 292 subfossil and 25 living trees and located at a lake (54.2° N, 70.3° W) corresponding to the green star in figure 6.1. The proxy time series of tree ring width indices is visualised in the top panel of figure 6.2. It has $N = 1102$ data points, is annually sampled, and covers the period $910 - 2011$ AD.

This local tree ring width index chronology is part of a millennial temperature reconstruction of annual summer temperatures in eastern Canada exhibiting responses to volcanic activity (Gennaretti et al., 2014). In fact, the region has been found to

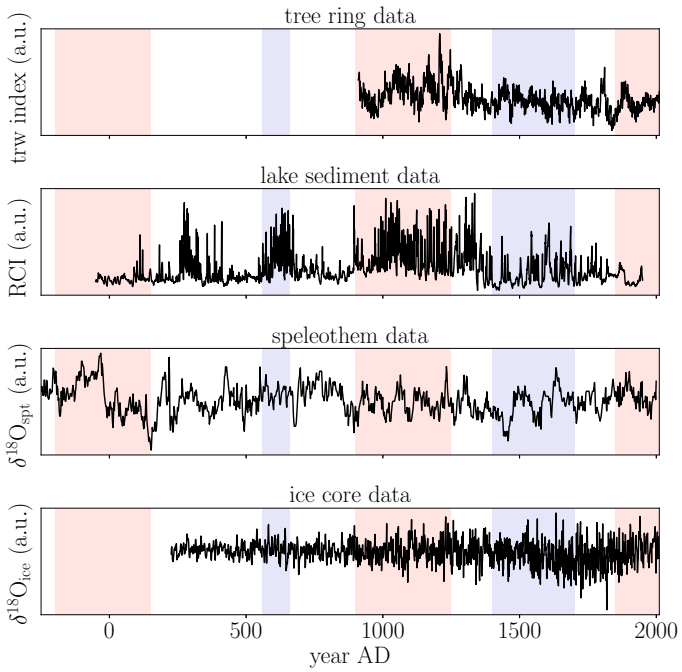

Figure 6.2.: Proxy time series of tree ring width (trw) indices, red colour intensity (RCI) of the lake sediment data, and oxygen isotope ratios (δ^{18}O) of the speleothem and the ice core data (top to bottom). The vertically shaded areas correspond to the episodes of outstanding climate variability as introduced in section 6.1.

be more sensitive to volcanism than, for example, Eurasia as complex sea-ice-ocean feedbacks in combination with explosive volcanic eruptions can cause or extend cold episodes. Particularly, the Samalas eruption (1257 AD) and the Tambora eruption (1815 AD) have been identified to influence tree growth in eastern Canada (Gennaretti et al., 2014).

Tree rings have so far not been studied using recurrence based approaches, mainly because corresponding time series usually show unbalanced variability across the different frequencies (Briffa et al., 1996). As the data set provided in Gennaretti et al. (2014) is classified as good in Esper et al. (2016), we expect it to be a suitable exemplary data set to start exploring this proxy with our framework of wRNA and wssRNA.

6.2.2. Lake sediments

Another important archive for past climate reconstructions are lacustrine sediments which stand out because of their global distribution over all climatic zones, their high resolution, and because they cover long time spans (Bradley, 2015e; Cohen, 2003). They contain a plethora of different proxy variables that can be considered for inferring information on past climate variability as, for example, sedimentary proxies, physiochemical proxies, and biological proxies (Zolitschka and Enters, 2009).

We study the red color intensity (RCI) data from Laguna Pallcacocha (Moy et al., 2002) which is a high-altitude lake in southern Ecuador (2.8° S, 79.2° W) marked by the blue star in figure 6.1. We use the most recent part of the available time series covering the interval $-50 - 1950$ AD. As the original time series is non-uniformly sampled, we interpolate it to uniform sampling using linear and cubic spline interpolation. The average sampling rate is given as $\langle dt \rangle = 0.51$ years corresponding to a length of $N = 3901$ data points. The linearly interpolated time series is displayed in the second panel of figure 6.2.

The red color intensity has been used as a proxy for rainfall intensity. In particular, higher values of the RCI represent lighter coloured laminae in the sediment and can be associated with strong rainfall events (Moy et al., 2002). In Moy et al. (2002), it was also found that this time series can be related to the strength of historical El Niño Southern Oscillation (ENSO) events as the recorded strong rainfall events were triggered by moderate to strong warm ENSO episodes, i. e., El Niño events.

6.2.3. Speleothems

Speleothems are formations in caves mainly consisting of calcium carbonate which incrementally grow from drips of groundwater passing through the ambient rock of the cave, that is, the karst (Bradley, 2015d). The isotopic composition of speleothems is an important high-resolution palaeoclimate proxy due to the archive's global distribution in areas where other archives are less represented, the possibility to obtain precise chronologies, and the preservation of many time scales in the records (Wong and Breecker, 2015; Atsawawaranunt et al., 2018). In the lower latitudes, the archive

is mostly sensitive to changes in precipitation amount, while in higher latitudes, temperature is the more important driver for the variability of the speleothem's isotopic composition (Bradley, 2015d; Oster et al., 2019). Still, including information about the complex local boundary conditions of and the microclimate in the caves is of major importance for interpreting the proxy signals (Lechleitner et al., 2018).

To study oxygen isotope ratios (δ^{18}O) of speleothems, we use data from the stalagmite JX-6 from Juxtlahuaca cave (Lachniet et al., 2012) which is located in southern Mexico (17.4° N, 99.2° W) as indicated by the red star in figure 6.1. Again, we use linear and cubic spline interpolation to obtain uniform sampling with average sampling rate $\langle dt \rangle = 1.8$ years, thus, the resolution of the data is lower than for the lake sediment data. The time series covers the period $-250 - 2000$ AD and consists of $N = 1218$ data points. The third panel of figure 6.2 shows the corresponding linearly interpolated time series. This data set has also been found to be precipitation sensitive and thus to characterise the rainfall variability in the region where smaller values of the oxygen ratios are related to more rainfall and larger values correspondingly to less rainfall. In the study area, rainfall is mostly affected by the strength of the North American summer monsoon which, in turn, is modulated by ENSO with warm ENSO episodes weakening the summer monsoon and vice versa (Lachniet et al., 2012).

6.2.4. Ice cores

Ice cores consist of accumulated snow that transforms to firn and later to ice by a de- and reformation of the snow crystals due to the increasing weight of subsequently fallen snow (Bradley, 2015c). They are one of the most important archives for reconstructing past atmospheric conditions as they provide, for example, information on past temperatures and the atmospheric composition via the isotopic composition of the ice and air contained in closed bubbles, respectively (Jouzel, 2013). In the last decades, data from high-elevation ice cores in the low latitudes have become increasingly available and offer the possibility to study past climate variability in the context of recent climate change (Thompson et al., 2005). To obtain reliable results from those high-resolution cores, some challenges still have to be addressed in more detail. For example, dating of the tropical ice cores becomes difficult for times in which the seasonal cycle is no longer resolved and also the interpretation of the isotopic composition in such cores is debated (Vimeux et al., 2009).

To explore the ice core archive, we use a data set of oxygen isotope ratios (δ^{18}O) from the Quelccaya ice cap (Thompson et al., 2013). The cap is located in the Peruvian Andes (13.9° S, 70.8° W) and lies at an altitude of 5670 m above sea level. The location of Quelccaya ice cap is denoted by the magenta star in figure 6.1. The time series is annually sampled and spans the interval $226 - 2009$ AD, thus it consists of $N = 1784$ data points. A visualisation of the time series can be found in the bottom panel of figure 6.2.

The variability of the δ^{18}O in this data set has been found to be related to sea surface temperatures in the tropical eastern Pacific (Thompson et al., 2013). Similar relationships between Pacific sea surface temperatures and the δ^{18}O in tropical ice

cores have been found, for example, in Vuille et al. (2003) and could be explained by an influence of Pacific sea surface temperatures on upper-level wind anomalies that force the moisture flow over the Andes.

6.3. Results

We now apply the developed analysis framework to the four proxy time series in order to characterise past climate variability on the American continents. First, we start by presenting the results for the varying phase space reconstruction approaches from publication P1. Afterwards, we use uniform time delay embedding in combination with wRNA and wssRNA and the areawise significance test following the framework summarised in chapter 5. The corresponding results for the tree ring width index time series follow those described in publication P2.

6.3.1. Phase space reconstruction

To study the dependence of wRNA on different phase space reconstruction approaches for real-world data, we analyse the lake sediment data set from Laguna Pallcacocha and the speleothem oxygen isotope ratios from Juxtlahuaca cave. We compare the results for the network transitivity of wRNA when reconstructing the phase space of the systems using uniform time delay embedding for varying delay times τ, derivative embedding with the discrete Legendre polynomials for varying numbers p of neighbours taken into account for derivative estimation, and derivative embedding with moving Taylor Bayesian regression (MoTaBaR) for varying numbers N_{mtb} of points taken into account for the local Taylor approximation. For the derivative embeddings, the resulting time series are scaled to have unit variance. The embedding dimension is chosen to be $m = 4$ in accordance with the false nearest neighbour criterion. In fact, when varying the embedding dimension, we observe similar results (not shown). The windowed analysis is performed for five values of the window width, $W \in [100, 150, 200, 250, 500]\,\langle dt \rangle$ with offset $dW = 1\,\langle dt \rangle$. The pointwise significance test is based on random shuffling surrogates with significance level $s_{\mathrm{pw}} = 0.95$. The results are visualised in figure 6.3.

For the Laguna Pallcacocha data set and time delay embedding, we observe four to five periods with significantly high and one to two periods of significantly low values of the network transitivity. For larger window widths, the timing shifts to more recent times which can be explained by recalling that we assign the time to a window such that it represents the dynamics of the W previous observations. For derivative embedding with discrete Legendre polynomials, we get similar results as for time delay embedding though for larger W, the periods of significant transitivity values get wider and neighbouring periods can no longer be separated. Also, we observe a higher number of significant points. For derivative embedding with MoTaBaR, we see a very stable behaviour of the identified anomalies for varying N_{mtb} and more but shorter periods of significant values of the network transitivity. Additionally, the

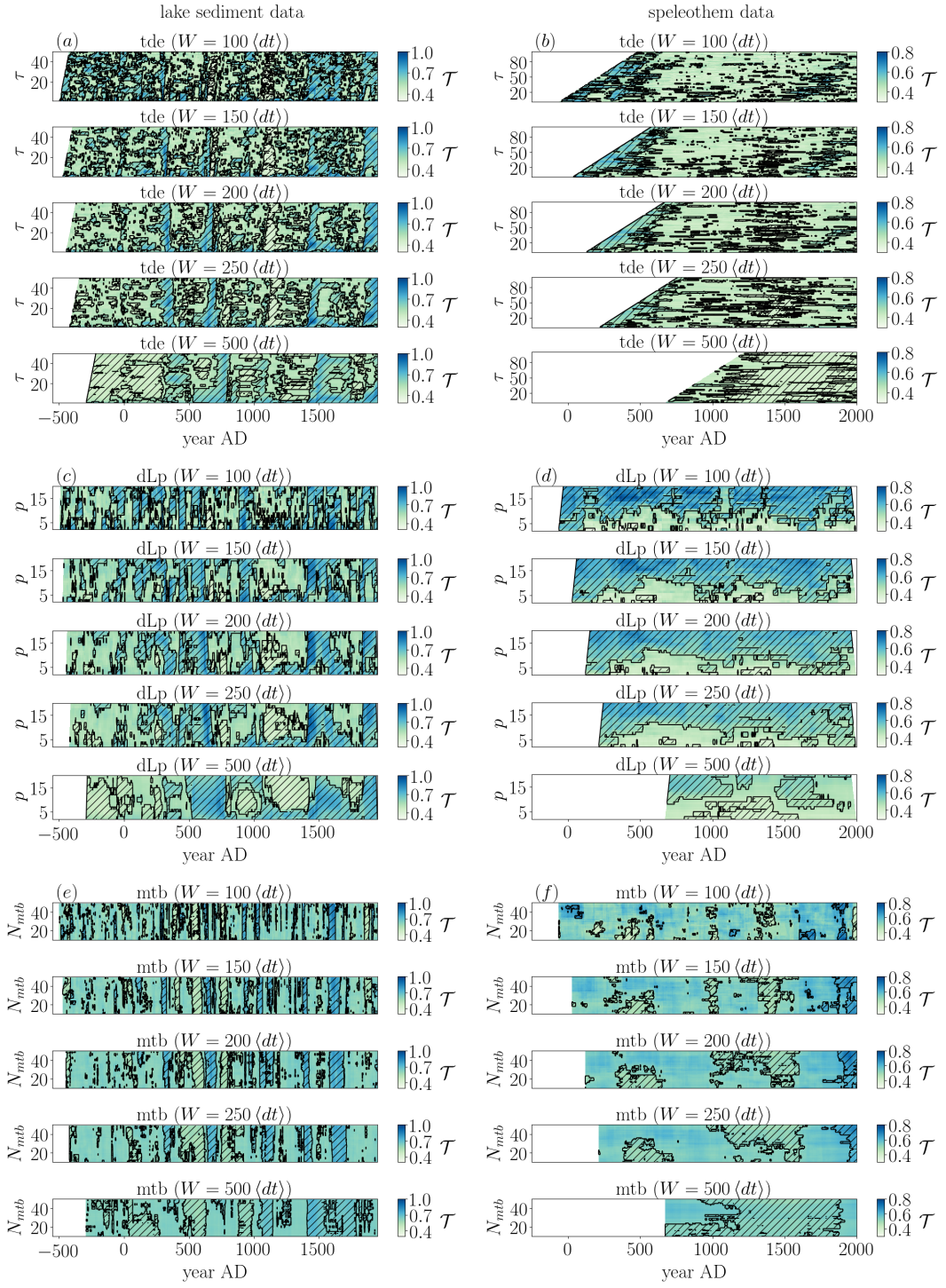

Figure 6.3.: Network transitivity (colour coded) as a function of time for Laguna Pallcacocha ((a), (c), (e)) and Juxtlahuaca cave ((b), (d), (f)) data for different phase space reconstruction approaches and varying embedding parameters: ((a), (b)) time delay embedding for varying delay times τ, ((c), (d)) derivative embedding using discrete Legendre polynomials for varying number of neighbours p, and ((e), (f)) derivative embedding using MoTaBaR for varying N_{mtb}. Pointwise significant points are marked by the hatched contours. Adapted from P1, with the permission of AIP Publishing.

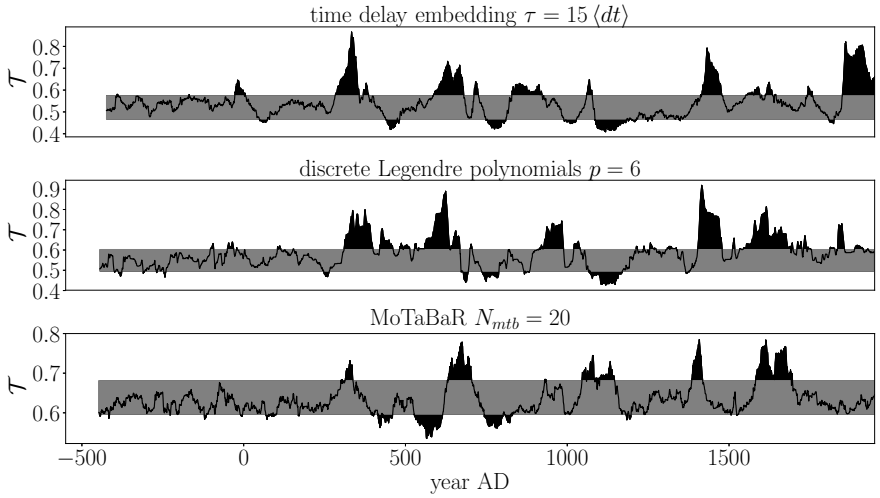

Figure 6.4.: Network transitivity for window width $W = 200\,\langle dt \rangle$ of Laguna Pallcacocha data for the three considered phase space reconstruction approaches. The grey bars represent the confidence bounds derived from the random shuffling surrogates. Reproduced from P1, with the permission of AIP Publishing.

maximum values of the resulting network transitivity are lower and the minimum values are higher than for the other two approaches.

To explore the similarities and differences between the different approaches in more detail, figure 6.4 shows the network transitivity for time delay embedding with delay time $\tau = 15\,\langle dt \rangle$, for derivative embedding with the discrete Legendre polynomials for $p = 6$, and for derivative embedding with MoTaBaR for $N_{mtb} = 20$. Those parameter choices are motivated by the results described in chapter 3. We observe that the results for time delay embedding and derivative embedding with the discrete Legendre polynomials generally agree well. Some of the significant periods are more or less pronounced depending on the chosen phase space reconstruction approach. The results from MoTaBaR show less agreement with the other results and sometimes even exhibit opposite behaviour. This highlights the importance to consider more than one approach in order to check whether the results are robust and confirms the results from chapter 3 that uniform time delay embedding and derivative embedding with discrete Legendre polynomials can give comparable results. We discuss the relation of the detected anomalies to past climate variability in subsections 6.3.2 and 6.3.3 in combination with the areawise significance test.

In the results from the Juxtlahuaca cave data set, we cannot identify consistent anomalies within the different phase space reconstruction approaches and the corresponding parameter variations. Generally, we observe some elevated values of the network transitivity for the recent past and the oldest part of the time series as well as some low values of the transitivity around 1500 AD. However, the timing varies for the different methods and choices of the window width. For derivative embedding with discrete Legendre polynomials and large values of p, we see a different pattern

with many significant high values of the network transitivity. This can possibly be related to the fact that for larger p, the smoothing of the time series is stronger. In general, we do not expect the results for different values of p to be equally well suited for the analysis and our results confirm that a choice of p of the order of the embedding dimension is reasonable. For MoTaBaR, the results are more robust than for the other two approaches but not as much as for the corresponding results of Laguna Pallcacocha. Again, we observe that the range of transitivity values obtained with MoTaBaR differs from the range of the other approaches. In this case, we find very high values of the network transitivity. With respect to these results, the Juxtlahuaca cave data set does not seem to be equally well suited for the wRNA as the Laguna Pallcacocha data set.

6.3.2. Windowed recurrence network analysis

Next, we apply wRNA for varying window widths in combination with the areawise significance test to all four data sets introduced in section 6.2. We use uniform time delay embedding with delay times $\tau = 25\,\langle dt \rangle$ for the tree ring data, $\tau = 15\,\langle dt \rangle$ for the lake sediment data, $\tau = 11\,\langle dt \rangle$ for the speleothem data, and $\tau = 2\,\langle dt \rangle$ for the ice core data. For the lake sediment data, we choose the embedding dimension to be $m = 4$, while for the other three data sets, we use $m = 3$ which can be seen as a compromise between the results of the false nearest neighbour method and the length of the available data sets. The windowed analysis is performed as outlined in chapter 5 for window widths varying in the interval $[100, 300]\,\langle dt \rangle$ with step size $\Delta W = 1\,\langle dt \rangle$ and offset $dW = 1\,\langle dt \rangle$. The pointwise significance test is again based on random shuffling surrogates with confidence level $s_{\mathrm{pw}} = 0.95$ and the areawise significance test is performed as detailed in chapter 4 using the data-adaptive null model based on the iterative amplitude-adjusted Fourier transform surrogates. The fitting parameters and the confidence levels of the areawise significance test for the four data sets can be found in appendix C.

Figure 6.5 shows the results of the wRNA as a function of time. The vertical lines denote the episodes of documented climatic variations as discussed in the introduction. First, we note that we do not get any areawise significant patches of the network transitivity for the speleothem oxygen isotope ratios from Juxtlahuaca cave, confirming the expectations from subsection 6.3.1 that pointwise detected anomalies are not robust in this data set. For the lake sediment data from Laguna Pallcacocha and the oxygen isotope ratios from the Quelccaya ice cap, we find some patches of areawise significant values of the network transitivity, most of them corresponding to anomalously low values. For the tree ring data from eastern Canada, we find one patch of anomalously low values of the network transitivity around the Samalas eruption in 1257 AD possibly marking the end of the MCA in this region. Interestingly, for smaller delay times, we find areawise significant anomalies around the Tambora eruption in 1815 AD, which is discussed in more detail in appendix C.2.

With respect to the different episodes of documented climate variations of the past 2000 years, we find that for the RWP, there is not sufficient data coverage in order to

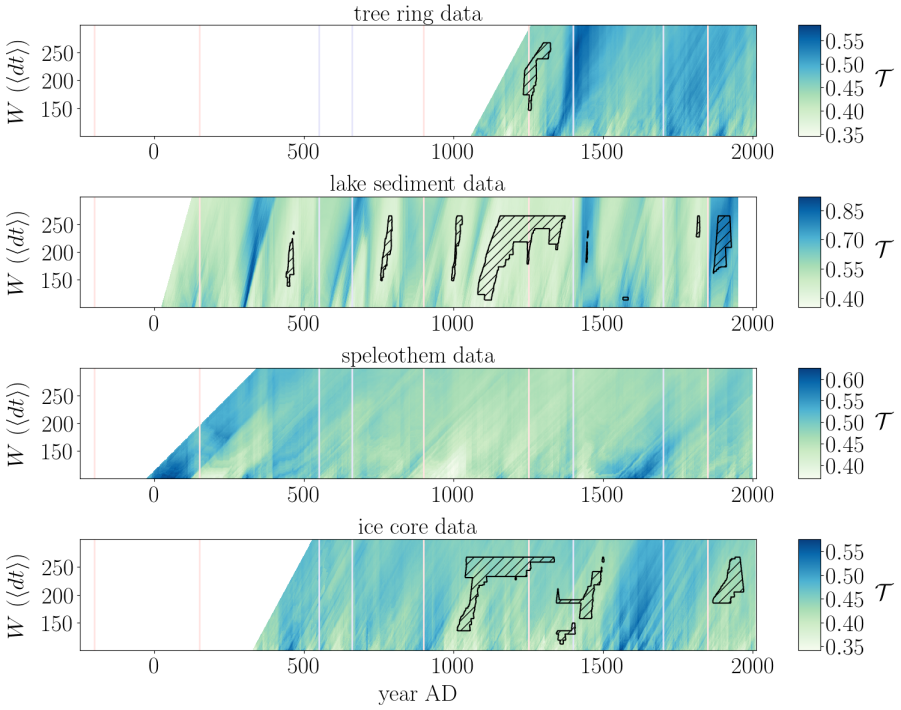

Figure 6.5.: Network transitivity (colour coded) obtained from wRNA as a function of time for varying window width W for the four different proxy time series in combination with the areawise significance test (hatched contours). The vertical lines again denote the episodes of outstanding climate variability introduced in section 6.1.

make any statements. The first centuries AD that have been associated with increased climatic variabilities, are covered by the lake and speleothem data, and partially also by the ice core data. We find both low and high values of the network transitivity within this period and one patch of areawise significant low values in the lake sediment data set corresponding to anomalously high-dimensional dynamics. During the LALIA, we do not find areawise significant analysis results but observe low values of the network transitivity. The same holds for the period between the LALIA and the MCA, where we also observe an areawise significant patch of low transitivity values in the data from Laguna Pallcacocha. During the MCA, and particularly towards its end for larger choices of the window width, we find areawise significant anomalously low values of the network transitivity indicating increasingly higher-dimensional dynamics. In Europe, the MCA has been characterised by relatively stable climatic conditions, thus, we would expect the dynamics to be lower-dimensional. Our findings point to a different manifestation of the MCA in North and South America or represent the reordering of the climate system towards the beginning of the LIA. The onset of the LIA is then characterised by higher values of the network transitivity with downward trend during the LIA for the tree ring and the lake sediment data, while the speleothem and the ice core data show lower values at the onset and elevated values during the LIA. Both for the lake and the ice core data, the beginning of the LIA also corresponds to areawise significant anomalies. For more recent times, we observe areawise significant low values of the network transitivity for the ice core and areawise significant high values for the lake sediment data.

To get another perspective on the obtained results, we analyse data of the last millennium reanalysis project version 2 (Hakim et al., 2016; Tardif et al., 2019) which provides reconstructed temperature and precipitation data of the past 1500 years for the different locations of the proxy time series (appendix C.3). We find less areawise significant patches of the network transitivity than for the proxy data and also observe local differences in the variability of the network transitivity.

Taken together, these results show that dynamical anomalies in the past climate are recorded differently at the different locations, thus they indicate different local manifestations of climate variability on the American continents. The fact that the speleothem data do not show areawise significant patches points to the role that local boundary conditions and the type of archive may play for how well a climate signal is reproduced within a proxy time series.

6.3.3. Windowed scale-specific recurrence network analysis

Finally, we study the four data sets using wssRNA for varying scales $s \in [0.2, 16.0]$ with $\Delta s = 0.2$. The width of the windows of the analysis is chosen according to equation (2.23) and the offset of the windowed analysis is $dW = 1 \langle dt \rangle$. The other analysis parameters are chosen as described above. The fitting parameters and confidence levels for the areawise test can be found in appendix C.

The resulting network transitivity as a function of time is shown in figure 6.6 where the vertical lines again denote the episodes of documented extraordinary

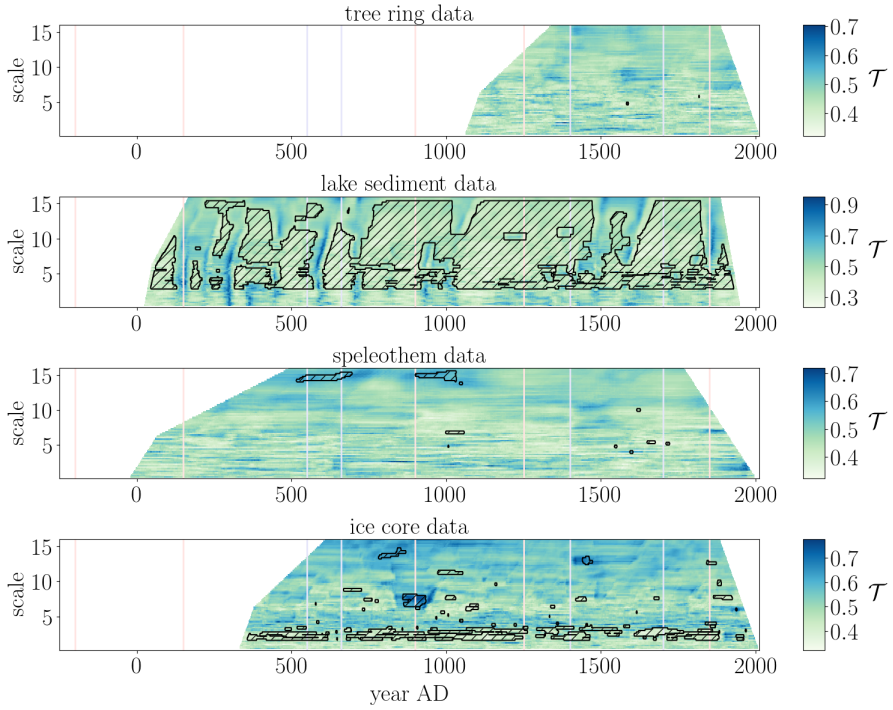

Figure 6.6.: Same as in figure 6.5 but for wssRNA with varying scales s.

climate variability. For the tree ring data, we only observe two very small patches of areawise significant values of the network transitivity not giving any additional insights to the results obtained from traditional wRNA. By contrast, the results for the lake sediment data from Laguna Pallcacocha show a very high number of areawise significant patches of anomalously low values of the network transitivity for scales $s > 2.8$. This might be related to the relatively low confidence level of the areawise significance test for this data set possibly resulting from the non-appropriate linear fitting model for the decorrelation length as a function of the scale. As already argued in chapter 4, a more general fitting model might increase the confidence level, decrease the number of areawise significant patches, and thus, yield results that can be better interpreted with respect to past climate variability. For the speleothem data from Juxtlahuaca cave, we observe two patches of areawise significant high values of the network transitivity at large scales during the LALIA and the beginning of the MCA indicating particularly low-dimensional dynamics at those times. Also, we find some small patches of areawise significant low values of the network transitivity at intermediate scales during the MCA and the LIA. The results from the Quelccaya ice cap data show many small areawise significant patches at small scales and some additional patches at intermediate scales. In particular, we find an areawise significant patch of high values of the network transitivity for intermediate scales at the onset of the MCA.

Thus, as argued in chapter 4, the wssRNA can, in many cases, be used to obtain additional insight into the dynamics of the underlying system as its dimensionality may vary depending on the considered time scales.

6.4. Discussion and conclusions

In order to characterise past climate variability on the American continents, we used the framework of wRNA to study four palaeoclimate proxy data sets from four different archives. They comprise tree ring width data from eastern Canada, the red colour intensity of a lake sediment from Laguna Pallcacocha in Ecuador, oxygen isotope ratios of a speleothem from Juxtlahuaca cave in Mexico, and oxygen isotope ratios of an ice core from Quelccaya ice cap in the Peruvian Andes.

In a first step, we compared the results of two of the data sets, namely the ones from Laguna Pallcacocha and Juxtlahuaca cave, when varying the phase space reconstruction approach and the embedding parameters. We found that uniform time delay embedding and derivative embedding with the discrete Legendre polynomials provide comparable results, while derivative embedding with MoTaBaR only partially agrees with the results from the other two approaches. Also, we found that the results from the Laguna Pallcacocha data set are more robust when varying the embedding parameters than those from the Juxtlahuaca cave data set.

Afterwards, we applied our framework of wRNA and wssRNA in combination with uniform time delay embedding to all four considered data sets. For the tree rings, we expected to find North Atlantic influences possibly similar to those in Europe with a particular sensitivity to explosive volcanic eruptions, which was indeed the case. Depending on the chosen delay for time delay embedding, areawise significant patches of the network transitivity appeared at times following the Samalas eruption in 1257 AD and the Tambora eruption in 1815 AD, coincident with the end of the MCA and the beginning of the CWP, respectively (appendix C.2). Additionally applying the wssRNA framework did not yield further insights.

For the ENSO sensitive lake sediment, we found more areawise significant patches of anomalously low than high values of the network transitivity. In particular, we found areawise significant low values starting in the middle of the MCA and extending to the beginning of the LIA for larger window widths. When applying wssRNA, we found a high fraction of areawise significant low values of the network transitivity. In order to identify patterns, we think that a more general fitting model of the decorrelation length as a function of the scale for the areawise significance test should be considered.

For the speleothem oxygen isotope ratios, we did not get any areawise significant patches of the network transitivity confirming that this data set might not be well suited for characterising past climate variability with wRNA. Still, when applying wssRNA, we found some areawise significant high values of the network transitivity during the LALIA and the beginning of the MCA for large scales.

For the ice core oxygen isotope ratios, we found a similar pattern of low values of the network transitivity starting in the middle of the MCA, while afterwards, the variability of the transitivity showed opposite behaviour to that observed in the lake sediment results. In particular, opposed to the areawise significant patch of high values of the network transitivity in the data from Laguna Pallcacocha, we observed an areawise significant patch of low values for the ice core data from Quelccaya ice cap for the CWP, showing that the climatic imprints as recorded by the proxy data differ locally in South America. For the wssRNA, we observed many small patches of areawise significant low values of the transitivity at small scales, while at intermediate scales, high values of the network transitivity, for example at the beginning of the MCA, prevailed.

Thus, in this chapter, we were able to confirm the results from chapter 3 that uniform time delay embedding and derivative embedding with discrete Legendre polynomials give comparable results. We showed that the framework of wRNA and wssRNA can be used to detect and characterise dynamical anomalies in past climate variability by studying palaeoclimate proxy time series from different archives. In particular, we found that some anomalies are present within all studied data sets, while for other periods, we observed local differences in past climate variability in North and South America. Still, this work only constitutes a first step towards exploring past climate variability on both American continents and more systematic studies, for example, about the imprint of different explosive volcanic eruptions on tree ring data, have to follow. However, as we also found that not all data sets give equally robust results when varying the analysis parameters, the role that the archive and local boundary conditions play for tracking past climate variability with the developed analysis framework has first to be assessed in more detail. This necessity is also supported by the results obtained from the last millennium reanalysis data studied in appendix C.3.

Chapter 7.

Proxy system model perspective on windowed recurrence network analysis

This chapter further tackles the problem of different palaeoclimate archives yielding differently robust results when applying windowed recurrence network analysis (wRNA). To systematically study the influence of the archive on detecting dynamical anomalies in past climate variability in palaeoclimate proxy time series with the developed analysis framework, we make use of the concept of proxy system modelling. In particular, we compare properties of different input time series and the corresponding results of wRNA to the properties and results of the time series processed through proxy system models for four different archives. With this, we aim at contributing to an improved interpretation of wRNA results obtained from real-world palaeoclimate data sets.

This chapter is based on, and closely follows, publication P3.

7.1. Introduction

The results of wRNA are not always equally robust under varying analysis parameters, as observed in chapter 6 for proxy time series from different archives. In fact, most studies employing wRNA in the palaeoclimate context focused on archives such as marine sediments (e. g. Donges et al., 2011a; Donges et al., 2011b) and speleothems (e. g. Donges et al., 2015a; Eroglu et al., 2016; Goswami et al., 2018) which exhibit balanced information content over the different time scales. Tree ring chronologies on the other hand, which often contain more high- than low-frequency variability (Briffa et al., 1996) have so far been widely disregarded. With respect to already obtained results when applying complex systems methods to paleoclimate data (Donges et al., 2015b; Eroglu et al., 2018; Trauth et al., 2019, chapter 6), a further exploration of past climate variability offers the prospective of deepening our understanding of the climate system. Thus, a systematic evaluation of the role of the proxy archive on the detectability of past climate variability with the developed analysis framework contributes to identifying suitable data sets to be studied with wRNA and interpreting the obtained results with respect to their climatic imprints.

For this, proxy system models, i. e., simple mathematical models that simulate the formation of a palaeoclimate proxy (Evans et al., 2013), can be of service. They allow to systematically study the impact of natural archives on tracking past climate

variability with an analysis method. Given some climate input variables, the proxy system model outputs a proxy time series. In this study, we consider intermediate complexity models that model tree ring width (Tolwinski-Ward et al., 2011), branched glycerol dialkyl glycerol tetraethers in lake sediments (Dee et al., 2018), and the isotopic compositions of speleothems (Dee et al., 2015) and ice cores (Dee et al., 2015).

In sections 7.2 and 7.3, we introduce the proxy system models and the artificial climate input time series, respectively. As input data, we consider two stochastic processes, Gaussian white noise (GWN) and an autoregressive process of order 1 (AR(1) process), two non-stationary time series from the paradigmatic Rössler and Lorenz systems, and, to simulate real past climate conditions, climate time series from the last millennium reanalysis project (Hakim et al., 2016; Tardif et al., 2019). We then compare the input and the proxy system model output with respect to the properties of the time series and the results of the wRNA in section 7.4 and present our main conclusions in section 7.5.

7.2. Proxy system models

Proxy system models take a time series representing local climatic conditions as input and simulate the physical process in the archive such that the resulting model output time series is similar to one obtained from a corresponding real-world archive. They thus offer the possibility to gain insights into the processes that determine the growth and the climate sensitivity of a particular palaeoclimate proxy and to investigate both characteristic properties of corresponding time series and their implications for further analyses.

In general, a proxy system model can be divided into an environment, a sensor, an archive, and an observation sub-model (Evans et al., 2013). The environment model uses the climate input variables to model the environmental factors relevant for the archive. The sensor model then describes the reaction of the archive to the environment, while the archive model accounts for processes relevant for the inscription of this reaction into the archive. Finally, the observation model simulates dating or measurement uncertainties.

We here use different combinations of the environment, the sensor, and the archive sub-models for the considered archives, while, for the sake of simplicity, neglecting possible dating and measurement uncertainties. In the following, we provide information on the considered proxy system models and the corresponding local boundary conditions that are used to tune the model parameters. A more detailed description of the proxy system models can be found in appendix D.1.

7.2.1. Tree ring model

Besides tree ring width, maximum latewood density (MXD) and the isotopic compositions of tree cellulose have become increasingly popular proxy variables for inferring information on past climate variability from trees (Briffa et al., 2004; Gessler et al.,

2014). Even though MXD is nowadays recognised to better reflect environmental conditions, we here focus on tree ring width because of its detailed mechanistic understanding (Fritts, 1976; Esper et al., 2016). To model tree ring growth at a particular site, we use the intermediate complexity model Vaganov-Shashkin-Lite (VS-Lite) (Tolwinski-Ward et al., 2011) which is a simplification of the model introduced in Vaganov et al. (2006). VS-Lite requires monthly input data of temperature T and either precipitation P or soil moisture M. As model parameters, thresholds for temperature and soil moisture below which growth is not possible and above which growth is optimal (T_1, M_1, T_2, M_2), the latitude of the site (Φ), and integration start and end months (I_0,I_f) that set the period in which the tree responds to climate have to be specified.

If precipitation is given, soil moisture is obtained by applying the Leaky Bucket model (Huang et al., 1996). It is based on the water balance in soil and requires as additional parameters the initial moisture content of the soil M_0, the minimum and maximum soil moisture content $M_{\text{min,max}}$, the root depth d_r, and the run-off parameters m, α and μ, characterising the surface run-off, the inverse response time of the base flow run-off, and the portion of subsurface flow going into base flow run-off and groundwater flow, respectively.

The sensor model for the tree ring width relies on the principle of limiting factors (Fritts, 1976), that is, the assumption that tree ring growth is limited by the resource that is the scarcest for optimal growing conditions. Thus, a temperature-based and a soil moisture-based growth response are calculated as

$$g_T(t) = \begin{cases} 0 & \text{if } T(t) < T_1 \\ \dfrac{T(t) - T_1}{T_2 - T_1} & \text{if } T_1 \leq T(t) \leq T_2 \\ 1 & \text{if } T_2 > T(t) \end{cases} \tag{7.1}$$

and

$$g_M(t) = \begin{cases} 0 & \text{if } M(t) < M_1 \\ \dfrac{M(t) - M_1}{M_2 - M_1} & \text{if } M_1 \leq M(t) \leq M_2 \\ 1 & \text{if } M_2 > M(t), \end{cases} \tag{7.2}$$

respectively. The total growth response $g(t)$ of the tree on the climatic input is then given as

$$g(t) = g_E(t) \min \left\{ g_T(t), g_M(t) \right\}, \tag{7.3}$$

that is, as the minimum of the temperature- and moisture-based growth responses modulated by an insolation-based growth response $g_E(t)$ depending on the normalised mean lengths of the day for each month.

Finally, the archive model integrates $g(t)$ over the growth period (I_0 to I_f) and the annually resolved time series of tree ring width anomalies is obtained by normalising

Table 7.1.: Climatic boundary conditions and model parameters for the tree ring width model as derived from the eastern Canada data (Gennaretti et al., 2014).

variable	description	value
T_m	mean temperature at site	$-3.8°$ C
P_m	mean annual precipitation sum	693 mm
Φ	latitude of site	54.2°N
$I_{0,f}$	integration period influencing growth	$[1, 12]$
$T_{1,2}$	temperature thresholds for growth	$[5.8, 17]$°C
$M_{1,2}$	soil moisture thresholds for growth	$[0.032, 0.24]$
$M_{\text{min, max}}$	minimum/maximum soil moisture content	$[0.01, 0.76]$
M_0	soil moisture content at beginning of simulation	0.2
m	surface run-off parameter	4.886
α	inverse response time of the base flow run-off	$0.093\,\text{month}^{-1}$
μ	subsurface run-off parameter	5.8
d_r	root depth	1000 mm

the integrated growth response to zero mean and unit variance. A more detailed description of the model can be found in appendix D.1.1.

To set the means of the input variables and to tune the model parameters, we use the climatic boundary conditions corresponding to those of the local tree ring width index chronology from eastern Canada (54.2° N, 70.3° W) studied in chapter 6 (Gennaretti et al., 2014). Regional average annual temperature is given as −3.8°C with average minimum temperatures of −23°C in January and average maximum temperatures of 16°C in July. The average annual precipitation sum amounts to 693 mm with a minimum of about 30 mm in February or March and a maximum of about 100 mm in September. The means and standard deviations of the climatic input variables and their corresponding annual cycles were chosen according to this information. To determine the threshold parameters, we used the Bayesian parameter estimation suggested in Tolwinski-Ward et al. (2013), while the parameters for the Leaky Bucket model were chosen as recommended in Tolwinski-Ward et al. (2011). Table 7.1 summarises the climatic boundary conditions and the model parameters.

7.2.2. Lake sediment model

As processes within a lake are highly complex, intermediate complexity models that are not specific to a particular lake are scarce. We here model branched glycerol dialkyl glycerol tetraethers (brGDGTs) contained within lacustrine sediments as this proxy can be captured in a simple model. BrGDGTs are a relatively new proxy with high potential for future palaeoclimate studies as they are, for example, not restricted to lakes with seasonal formation of ice sheets (Weijers et al., 2007; De Jonge et al., 2014; Russell et al., 2018). We use one of the sensor models provided in the PRoxY System Modelling (PRYSM) v2.0 framework (Dee et al., 2018) that requires a time series of mean annual air temperature T as input.

Branched glycerol dialkyl glycerol tetraethers are membrane lipids produced by anaerobic bacteria and their degree of cyclisation and methylation has been related to lake pH and mean annual soil and air temperatures (Weijers et al., 2007; De Jonge et al., 2014; Russell et al., 2018). In the sensor model, we use the Methylation of Branched Tetraether (MBT) index $\mathrm{MBT}'_{5\mathrm{ME}}$ to quantify the degree of methylation, which is related to mean annual air temperature via the equation (Russell et al., 2018)

$$\mathrm{MBT}'_{5\mathrm{ME}} = (T + 1.21)/32.42. \tag{7.4}$$

The archive model accounts for post-depositional perturbations, i. e., bioturbation, and mixing of the sediments using the TURBO2 model (Trauth, 2013). TURBO2 models the benthic mixing effects, that is, the mixing effects at the bottom of a lake or ocean, on individual sediment particles. In particular, instantaneous mixing of the sediment particles occurs in a mixed layer of a specified thickness on top of a sediment core, while the rest of the core is unaffected by the mixing. This model has been developed for studying bioturbation in ocean sediments, but has also been used for lacustrine archives (Dee et al., 2018). Apart from the sensor model output, the archive model requires three additional input parameters, the abundance of the signal carrier over time (abu), the thickness of the mixed layer over time (mxl), and the number of signal carriers on which the proxy signal is measured (numb). The model returns the time series of original and bioturbated abundances and corresponding proxy signatures which are then used as final proxy for the mean annual air temperature. Details on the model can be found in appendix D.1.2.

As climatic boundary conditions, we use the same setting as for the tree ring width model. For the model parameters, we employ typical values for lake sediments given in the PRYSM implementation for modelling the lake archive (Dee et al., 2018) as corresponding information for lakes from the modelled region was not available. In particular, it should be noted that the abundances of the input species and the mixed layer thickness are constant over time. The climatic boundary conditions and model input parameters are given in table 7.2.

Table 7.2.: Climatic boundary conditions and model parameters for the lake model as derived from the eastern Canada data (Gennaretti et al., 2014).

variable	description	value
T_m	mean temperature at site	$-3.8°$ C
abu	abundances of input species	200
mxl	mixed layer thickness	4
numb	amount of measured foraminifera	10

7.2.3. Speleothem model

We use the model for speleothem δ^{18}O that is implemented and presented within the PRYSM framework (Dee et al., 2015). It is an intermediate-complexity model and based on the model presented in Partin et al. (2013). As input, the mean annual temperature T and the mean of the precipitation-weighted annual δ^{18}O content of the precipitation $\delta^{18}O_P$ are required. Also, the ground water residence time τ_{gw} has to be specified.

In the sensor model, processes in the karst and the cave are taken into account, while other processes such as evapotranspiration are neglected. In particular, the $\delta^{18}O_P$ signal is filtered by applying an aquifer recharge model to simulate the the mixing of waters of different ages in the karst (Gelhar and Wilson, 1974) which is parametrised by the mean transit time τ_{gw}. The isotopic composition of the cave water is modelled as the convolution (denoted by $*$) of the isotopic composition of the water and the impulse response of the aquifer recharge model $g(t) = 1/\tau_{\mathrm{gw}} \exp(-t\tau_{\mathrm{gw}})$

$$\delta^{18}O_d = g(t) * \delta^{18}O_P. \tag{7.5}$$

Finally, the isotopic composition of the flowstone calcite $\delta^{18}O_c$ is obtained by implementing a temperature-dependent fractionation (Wackerbarth et al., 2010)

$$\delta^{18}O_c = \frac{\delta^{18}O_d + 1000}{1.03086} \exp\left(\frac{2780}{T_a^2} - \frac{2.89}{1000}\right) - 1000. \tag{7.6}$$

Here, the temperature T_a is given as the decadal average of T. Details on the model can be found in appendix D.1.3.

For the model, we use the climatic boundary conditions of Juxtlahuaca cave (Lachniet et al., 2012) which was also studied in chapter 6. It is located in southern Mexico (17.4° N, 99.2° W) and has been related to rainfall variability in the region (Lachniet et al., 2012). The average value of the oxygen isotope ratios are given as $-8.4\,‰$, while the average temperature in the cave has been found to be 24.2°C for modern conditions (Lachniet et al., 2017). We choose the mean of the precipitation-weighted

Table 7.3.: Climatic boundary conditions and model parameters for the speleothem δ^{18}O model as derived from the Juxtlahuaca cave data (Lachniet et al., 2012).

variable	description	value
T_m	mean temperature at site	24.2° C
$\delta^{18}O_P$	mean isotopic composition of precipitation	−6.60 ‰
τ_{gw}	mean aquifer transit time	9 years

isotopic composition of the input such that the average of the model output data equals the average of the Juxtlahuaca cave proxy data. The lag between modern rainfall data and the proxy data that leads to the highest correlations between those quantities has been found to be 9 years (Lachniet et al., 2012), thus, we use this value as the mean aquifer transit time. Table 7.3 summarises the climatic boundary conditions and model parameters.

7.2.4. Ice core model

We here model the isotopic composition of ice of tropical ice cores by using the corresponding model provided within the PRYSM framework (Dee et al., 2015). The model requires the mean temperature T_m and the precipitation-weighted mean annual isotopic composition of the precipitation $\delta^{18}O_P$ as input. Additionally, the altitude of the glacier z, the mean surface pressure p, the mean accumulation rate at the site A_m and the total depth of the core $h_{\max}$, given by the time span of the observations multiplied by the average accumulation rate, have to be specified.

In a first step, the sensor model corrects the isotopic composition of the precipitation for the altitude of the glacier using the altitude effect (Dee et al., 2015). Then, the archive model accounts for compaction and diffusion within the core. For this, the density of the core has to be calculated depending on its depth. We use an adapted version of the firn densification model presented in Herron and Langway (1980). From the density and the mean temperature T_m, it is possible to compute the diffusion length σ as a function of the depth h (Cuffey and Steig, 1998; Johnsen et al., 2000; Gkinis et al., 2014) which, in turn, can be used to calculate the final proxy time series $\delta^{18}O_d$. The isotopic signal of the ice $\delta^{18}O_{\text{ice}}$ is convolved with a Gaussian kernel function of standard deviation corresponding to the diffusion length at the given depth

$$\delta^{18}O_d = \frac{1}{\sigma\sqrt{2\pi}} \exp\left(\frac{-h^2}{2\sigma^2}\right) * \delta^{18}O_{\text{ice}}. \tag{7.7}$$

The convolution is again denoted by the asterisk ($*$). Appendix D.1.4 provides a detailed description of the ice core model.

Table 7.4.: Climatic boundary conditions and model parameters for the ice core δ^{18}O model as derived from the Quelccaya ice cap data (Thompson et al., 2013; Yarleque et al., 2018).

variable	description	value
$\delta^{18}O_P$	mean isotopic composition of precipitation	$-3.75\,‰$
T_m	mean temperature at site	$-3.99°\,C$
A_m	average accumulation rate at site	1.15 m w.e./a
p	mean surface pressure at site	1 Atm
z	altitude of site	5670 m
ρ_0	surface density of snow at site	$300\,kg/m^3$
a	altitude effect	$-0.25\,‰/100\,m$

The climatic boundary conditions for the ice core δ^{18}O model are chosen corresponding to those at the Quelccaya ice cap (Thompson et al., 2013) studied in chapter 6. Quelccaya ice cap is located in the Peruvian Andes (13.9° S, 70.8° W) at an altitude of 5670 m above sea level and is characterised by an average accumulation rate of 1.15 m w.e. per year. The mean of the proxy $\delta^{18}O_{ice}$ values is $-17.9\,‰$ and the average annual temperature over the last decade at the Quelccaya ice cap is $T_m = -3.99°\,C$ (Yarleque et al., 2018). Table 7.4 summarises the climatic boundary conditions and the model parameters.

7.3. Input time series

To compare the impacts of different archive formation processes, we need to generate data of which we know the properties that we aim to analyse. We here consider two stochastic processes, namely GWN and an AR(1) process, non-stationary versions of the well-known Rössler and Lorenz systems, and output data from the last millennium reanalysis (LMR) project. These processes and systems were chosen in order to compare the model impact for both stochastic and deterministic input.

For each process except the last, one realisation resulting in a time series of length $N = 1000$ (years) is created for temperature, precipitation and precipitation-weighted oxygen isotope ratios as detailed below. For the stochastic time series, the realisations for the different variables are independent of each other, while for the non-stationary model systems, the precipitation is proportional to negative temperature and oxygen isotope ratios. As the tree ring width model requires monthly input, a noisy sinusoidally shaped annual cycle is added to the temperature and precipitation data where the amplitude and extrema are chosen in correspondence with the local

boundary conditions and the signal-to-noise ratio is given as 69 for temperature and as 98 for precipitation. Finally, yearly means for temperature and sums for precipitation are calculated as the other models require yearly input. The time series are first normalised to zero mean and unit standard deviation. Then, the mean is adjusted to the corresponding climatic boundary conditions as detailed in section 7.2.

7.3.1. Gaussian white noise

To test whether uncorrelated stochastic processes may lead to areawise significant anomalies in palaeoclimate time series, we consider Gaussian white noise. That is, we draw N independent random samples from the probability distribution (2.24) with mean $\mu = 0$ and standard deviation $\sigma = 1$

$$p_G(x) = \frac{1}{\sqrt{2\pi}} \exp\left(\frac{x^2}{2}\right). \tag{7.8}$$

Because of the stationarity of this process, we do not expect to detect significant dynamical anomalies in the resulting time series.

7.3.2. Autoregressive process of order 1

As short term correlated noise might be a more realistic input with respect to climate applications (von Storch and Zwiers, 1999), we also consider an AR(1) process. Here, we use the relation

$$x(t+1) = \alpha x(t) + \epsilon_t \tag{7.9}$$

to create a time series of length N. ϵ_t is a Gaussian random variable with zero mean and constant standard deviation $\sigma_{\epsilon_t} = 0.5$. The scaling factor is given as $\alpha = 0.7$ and as initial condition, we use $x(0) = 0.3$. The choice of $\alpha = 0.7$ corresponds to the order of the scaling factor that we obtained when fitting an AR(1) process to the tree ring width data from eastern Canada. For these parameter choices, we do not expect to detect significant dynamical anomalies in the data.

7.3.3. Non-stationary Rössler system

We again consider the non-stationary version of the Rössler system (ROS) as introduced in sections 2.2, 3.4.2 and 4.3. It is given by the set of ordinary differential equations (ODEs) specified in section 2.2 (equation (2.2)) with fixed parameters $a_R = 0.2$ and $c_R = 5.7$ and time varying parameter $b_R(t) = b_{R,0} + \Delta b_R(t - t_0)$ with $b_{R,0} = 0.02$ and $\Delta b_R = 0.001$. The system of ODEs is solved numerically with a temporal resolution of $\Delta t = 0.1$ for times in the range $[0, 730]$. The first 300 points are discarded and every seventh point of the remaining time series is used. This procedure is applied in order to reduce the dependence on the chosen initial condi-

tions ($x(0) = 0.5$, $y(0) = 0$ and $z(0) = 0$) and balance the precision of the numerical integration and the resolution and length of the time series.

As described in section 4.3, the bifurcation diagram (figure 4.1) reveals alternating periods of lower and higher dimensional dynamics in the time series. We expect this behaviour to be reflected by corresponding significantly high and low values of the network transitivity of the wRNA. Again, it should be noted that the bifurcation diagram contains the dynamics of the stationary Rössler system, while the time series represents the transient Rössler system and that detected anomalies do not correspond to transitions between more and less chaotic dynamics but rather identify periods of outstandingly high- or low-dimensional dynamics.

7.3.4. Non-stationary Lorenz system

The non-stationary Lorenz system (LOR) studied here is based on the Lorenz system introduced in section 2.2 and given by the corresponding set of ODEs (equation (2.1)). We fix the parameters a_L and c_L to $a_L = 10.0$ and $c_L = 8/3$, while the parameter b_L is varying over time, i. e., $b_L(t) = b_{L,0} + \Delta b_L(t - t_0)$ with $b_{L,0} = 160.0$ and $\Delta b_L = 0.02$. The system of ODEs is solved numerically with a temporal resolution of $\Delta t = 0.05$ for times in the range $[0, 500]$. Here, we use every fifth point of the x-component of the system. The initial conditions are given as $x(0) = 10.0$, $y(0) = 10.0$ and $z(0) = 10.0$.

The stationary Lorenz system exhibits a shift from periodic to chaotic dynamics at $b_L = 166.0$ (Barrio and Serrano, 2007). The transient system introduced above, has been found to show transitions at $b_L = 161.0$ and $b_L = 166.5$ (Donges et al., 2011a) which we expect to be reflected in corresponding high and low values of the network transitivity before and after $b_L = 166.5$, respectively.

7.3.5. Last millennium reanalysis data

To simulate real-world climate conditions, we use reconstructed temperature and precipitation time series for the period $501 - 2000$ AD provided by the last millennium reanalysis project version 2 (Hakim et al., 2016; Tardif et al., 2019). In this project, information from general circulation models and from proxy measurements are combined using palaeoclimate data assimilation. As we only have data for temperature and precipitation, we restrict ourselves to model tree ring width and brGDGTs for this input. The data set is globally gridded. We use the ensemble averaged time series with the coordinates closest to those where we situated the tree and the lake model (54° N, 70° W). When considering other coordinates in the region or averages over the region, we however found similar results (not shown).

7.4. Results

7.4.1. Time series properties

As a first step to evaluate the impact of the proxy system models on the input time series, we compare their properties to those of the different proxy system model output time series. The annually sampled input time series for temperature, precipitation, and the isotopic composition of the precipitation and the corresponding output time series obtained by applying the four proxy system models (tree ring model (trw), lake sediment model (lak), speleothem model (spt), and ice core model (ice)) for the five input scenarios of GWN, the AR(1) process, the non-stationary Rössler system, the non-stationary Lorenz system, and the last millennium reanalysis data are displayed in appendix D.2.

The speleothem, ice core, and lake sediment model output show the expected low-pass filter effect resulting from the residence time of the water in the cave, the diffusion within the ice core, and the bioturbation of the lake sediment, respectively. For the tree model, the expected short scale dynamics are evident. Also, it should be noted that the tree model with the parameters as specified in table 7.1 seems to respond to temperature, meaning that the limiting factor for tree growth identified by the VS-Lite model in eastern Canada is temperature. Of course, other factors such as the slope of the area or the constitution of the soil (which are not explicitly taken into account by the model) may also play a role for the climate sensitivity of the trees.

For further evaluation, we standardise all time series to compare their properties. The left panels of figure 7.1 show the histograms of the input and output time series. To quantify differences in the histograms, we consider the skewness of the distributions of the different time series as a simple measure of identifying possible biases introduced by the proxy system models. In table 7.5, the skewness of the distributions of the different time series is displayed. In particular, those values showing a significant deviation from the skewness of the corresponding input are marked in bold. The assessment of the significance of the deviations is discussed in appendix D.2. The resulting time series from the tree model all show significant deviations in skewness from the input data, which is probably related to the thresholding of the growth response functions for temperature and soil moisture. For the other proxy models, we observe significant deviations of the output of the non-stationary model systems and the reanalysis data. For the speleothem model, we also observe a significant deviation of the skewness for the AR(1) process. This behaviour of the different models possibly points to a different reaction of the models to different distributions of the input data which should be explored in more detail in future work.

The middle and right panels of figure 7.1 show the autocorrelation functions and estimates of the power spectral density obtained using the Welch method (Welch, 1967) of the different input and model output time series. Again, the results from the tree ring width model closely follow the autocorrelations and power spectral densities of the temperature input. The speleothem model output shows the expected loss

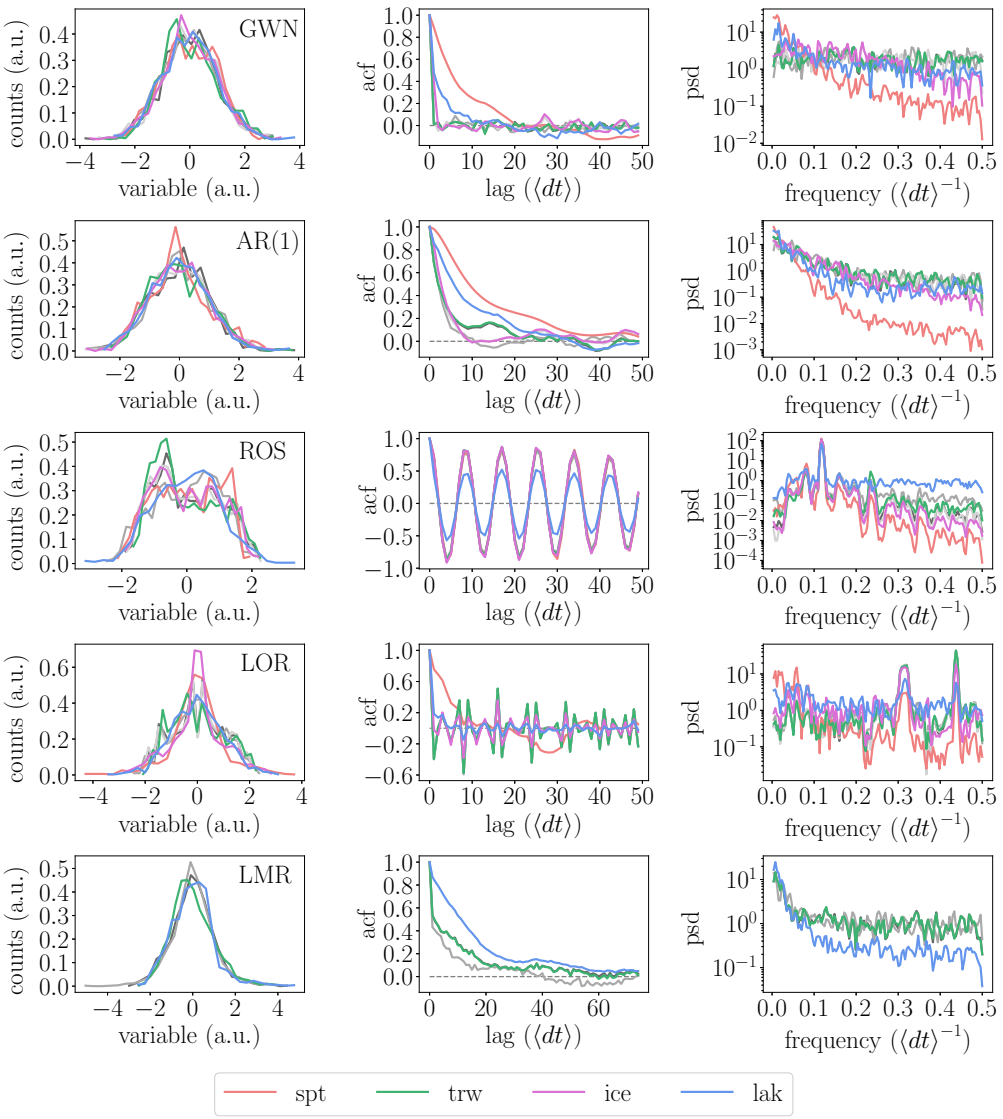

Figure 7.1.: Normalised histograms (left), autocorrelation functions (acf, middle) and estimated power spectral densities (psd, right) of the different input and proxy system model output time series for GWN, AR(1), ROS, LOR, and LMR (top to bottom). The input time series are denoted in grey, the tree ring model output in green, the lake sediment model output in blue, the speleothem model output in red, and the ice core model output in magenta. Adapted from P3.

Table 7.5.: Skewness of the different input and proxy system model output time series. Significant deviations from the skewness of the surrogate data are marked in bold face (see appendix D.2).

input/output	GWN	AR(1)	ROS	LOR	LMR
temperature	0.00	0.07	0.21	−0.02	0.33
precipitation	0.12	−0.03	−0.20	0.01	0.01
isotopes	−0.06	0.12	0.22	−0.02	–
trw	**0.34**	**0.35**	**0.40**	**0.26**	**0.63**
lak	0.11	0.23	**−0.05**	**0.01**	**0.71**
spt	−0.06	**0.38**	**−0.09**	**−0.21**	–
ice	−0.01	0.15	**0.15**	**−0.05**	–

of power in the higher frequencies. Such a loss of power can also be observed in the ice core model output, but is not as pronounced as for the speleothem model output. The same is true for the lake sediment model output with the exception of the Rössler and Lorenz scenarios. In this case, the output exhibits more power in the higher frequencies than the corresponding input. This might be related to the different intrinsic frequencies of the non-stationary model systems in comparison with the stochastic processes in combination with the choice of mxl = 4 for the mixed layer thickness in the lake sediment model.

7.4.2. Windowed recurrence network analysis

In a second step, we apply wRNA to the different input and proxy model output time series and compare the results. That is, we apply the analysis framework developed in the first part of the thesis and summarised in chapter 5. We reconstruct the phase space of the time series using uniform time delay embedding for embedding dimension $m = 3$ and delay time τ corresponding to the first root of the autocorrelation function. The wRNA is performed for window widths $W \in [100, 300] \langle dt \rangle$ with step size $\Delta W = 1 \langle dt \rangle$ and offset $dW = 1 \langle dt \rangle$. The recurrence rate is fixed to $RR = 0.05$ and distances are calculated with respect to the maximum norm. Finally, the areawise significance test introduced in chapter 4 is applied based on a pointwise significance test using random shuffling surrogates with confidence level $s_{\mathrm{pw}} = 0.95$ and the iterative amplitude-adjusted Fourier transform null model.

The results for the network transitivity are shown in figures 7.2 to 7.6. Areawise significant patches indicating anomalously low or high values of the network transitivity are highlighted by the hatched areas. The confidence levels of the areawise significance test are given in table 7.6. We observe that except for the case of the AR(1) process

Table 7.6.: Confidence levels s_{aw} of the areawise significance test for the different input and proxy model output time series.

input/output	GWN	AR(1)	ROS	LOR	LMR
temperature	0.994	0.998	0.955	0.994	0.998
precipitation	0.995	0.993	0.960	0.990	0.995
isotopes	0.997	0.978	0.954	0.989	–
trw	0.994	0.991	0.957	0.983	0.996
lak	0.995	0.971	0.989	0.998	0.964
spt	0.953	0.704	0.954	0.996	–
ice	0.989	0.979	0.960	0.985	–

combined with the speleothem model, we get very high confidence levels, indicating that the areawise test manages well to discriminate between time series that follow and such that do not follow the corresponding null model.

The results for Gaussian white noise (figure 7.2) do neither exhibit any areawise significant points for the input temperature nor for the output of the tree ring width and the lacustrine archive. The GWN realisation of the isotopic composition of the precipitation shows a patch of areawise significant anomalously low values of the network transitivity that is not expected for this type of process. Those anomalies are not apparent in the output of the speleothem and the ice model, that is, processing those data through the models leads to less significant points. The speleothem model output additionally shows a small patch of falsely identified areawise significant points for small window widths after $t = 950$.

For the realisation of the temperature AR(1) process (figure 7.3), we find an areawise significant patch of anomalously high values of network transitivity that is not present in the tree ring and lake sediment model output. For the realisation of the isotope input, we do not observe any areawise significant points. However, the speleothem model output is associated with two large falsely identified patches of significant values of the network transitivity. To improve the reliability of the results for the stochastic processes and to evaluate whether the particular realisations created within this study give representative results, more realisations of these processes should be analysed and compared.

The network transitivity of the input time series of the non-stationary Rössler system (figure 7.4) shows areawise significant patches of low values for $b_R \in [0.30, 0.35]$ and of high values in the regime $b_R \in [0.55, 0.57]$. The results for the isotope input additionally exhibit a small areawise significant patch around $b_R = 0.25$. Again, the tree and lake model results do not show areawise significant points, i. e., the detection of significant points is prevented by processing the input through the model.

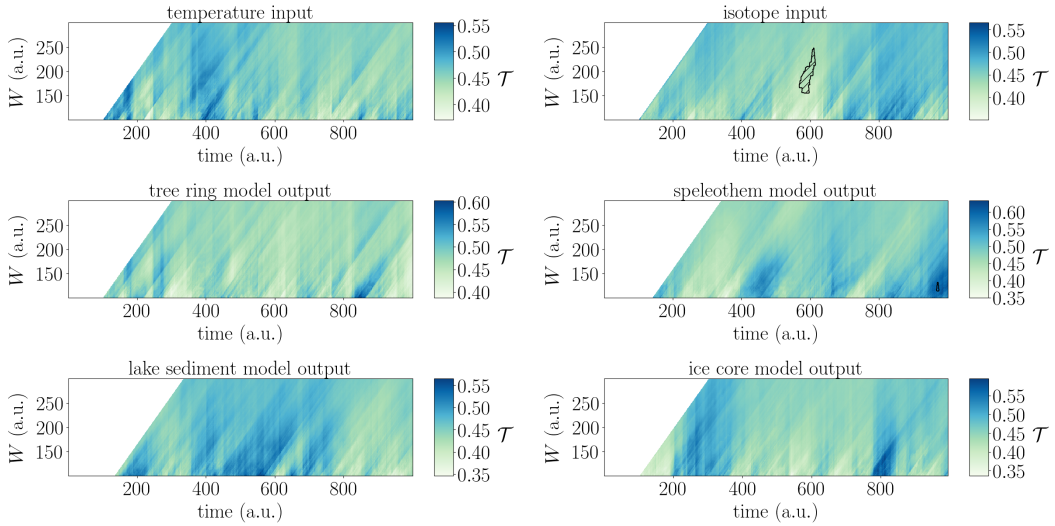

Figure 7.2.: Network transitivity (colour-coded) for GWN model in- and output with areawise significance test (hatched contours). Adapted from P3.

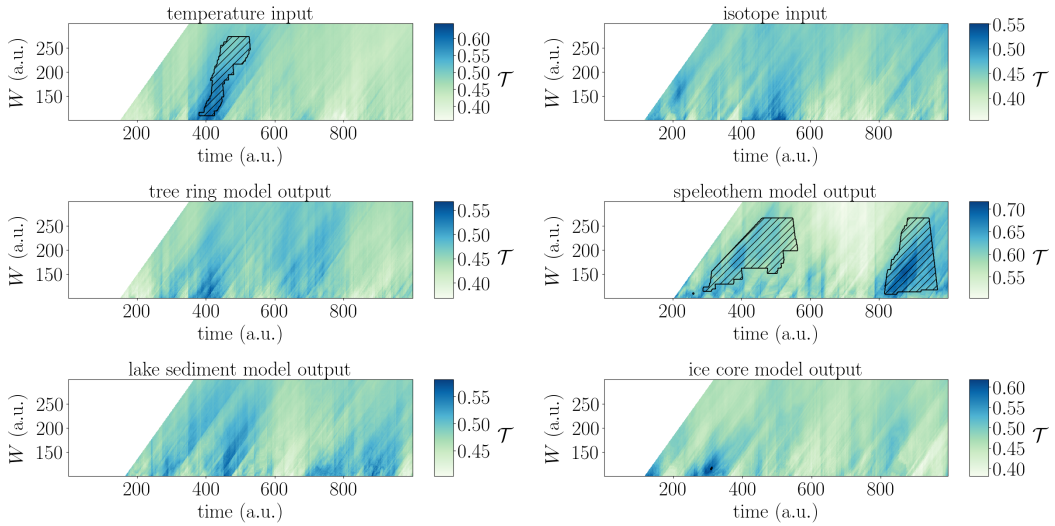

Figure 7.3.: Same as in figure 7.2 but for the AR(1) model in- and output. Adapted from P3.

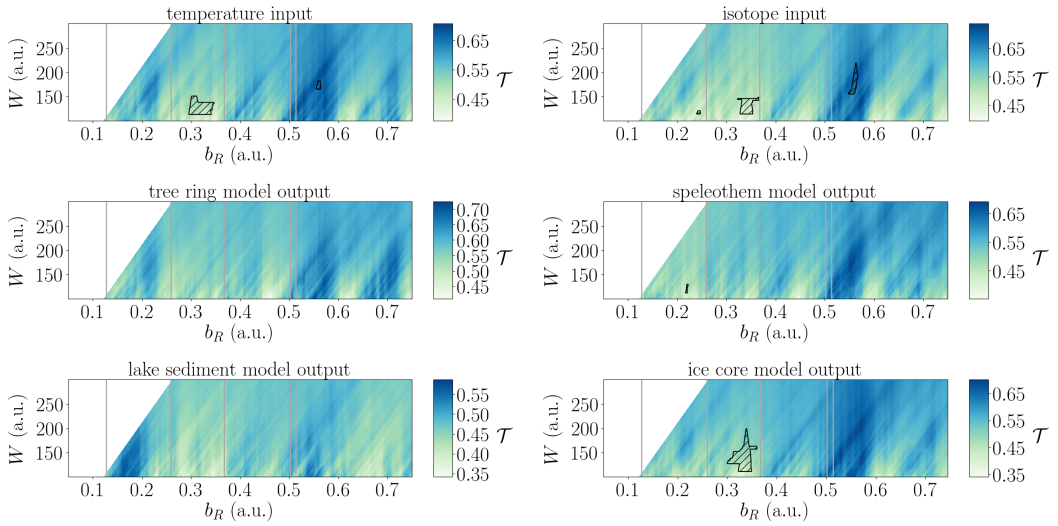

Figure 7.4.: Same as in figure 7.2 but for the non-stationary Rössler system in- and output. The vertical grey lines denote the periods of more and less chaotic dynamics as identified in the bifurcation diagram of the stationary system (figure 4.1). Adapted from P3.

In the results for the speleothem model output, we only identify a small areawise significant patch possibly associated with the one from the isotope input at $b_R = 0.25$. The output from the ice core model reproduces the areawise significant patch for $b_R \in [0.30, 0.35]$ but extends to slightly larger window widths.

For the non-stationary Lorenz system (figure 7.5), we identify two main patches of areawise significant values of the network transitivity in the input results. They comprise a large patch of areawise significant low values of the network transitivity for large values of b_L and a small patch of areawise significant high values of the network transitivity around $b_L = 163.2$. The isotope input additionally shows a small patch around $b_L = 166.6$. The tree ring model output also shows the large and the small patch of significant values of the network transitivity, where the small patch is markedly extended for larger window widths, while the lake sediment model shows no areawise significant points. In the speleothem model output, we identify two large patches of areawise significant high values for $b_L \in [163, 164]$ and $b_L \in [165.0, 166.6]$. That is, the small patches from the isotope input also appear in the model output, but additionally, a large number of falsely identified significant points is evident. The large patch of low transitivity values is not reproduced. The ice core model output exhibits a small patch for larger values of b_L and small values of the window width. Thus, most of the areawise significant points apparent in the isotope input are missed.

The last millennium reanalysis data temperature input (figure 7.6), shows a patch of areawise significant low values of the network transitivity around the onset of the European Medieval Climate Anomaly (MCA). The vertical lines denote the estimated on- and offsets of characteristic climatic episodes of the past two millennia

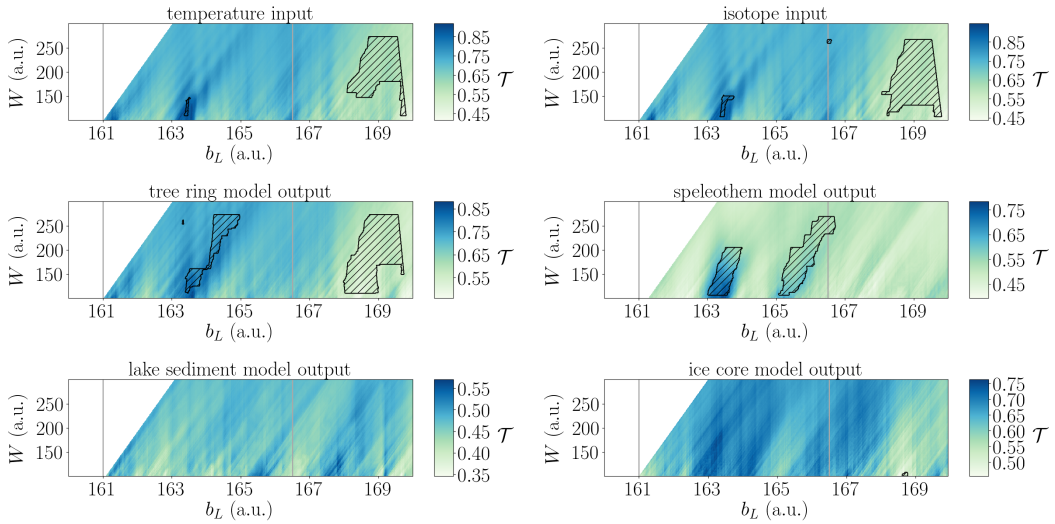

Figure 7.5.: Same as in figure 7.2 but for the non-stationary Lorenz system in- and output. The vertical grey lines denote the transitions identified in Donges et al. (2011a). Adapted from P3.

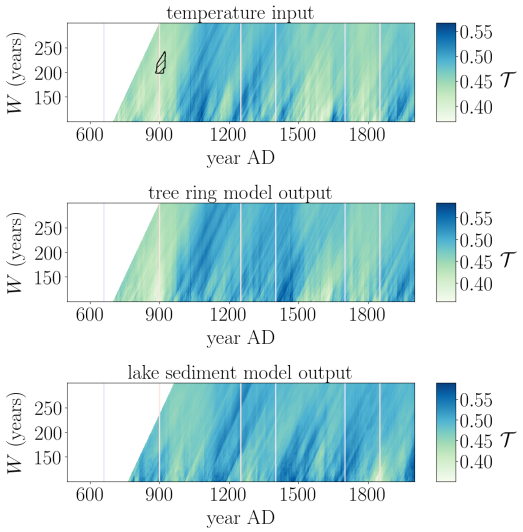

Figure 7.6.: Same as in figure 7.2 but for the last millennium reanalysis in- and output (54° N, 70° W). The vertical lines denote the outstanding episodes of climate variability introduced in section 6.1. Adapted from P3.

Table 7.7.: Fractions of missed and falsely identified significant points in the different proxy models with respect to the corresponding input variables (var).

proxy	var		GWN	AR(1)	ROS	LOR	LMR
trw	T	missed	0.000	0.056	0.012	0.003	0.004
		falsely identified	0.000	0.000	0.000	0.064	0.000
lak	T	missed	0.000	0.056	0.011	0.083	0.004
		falsely identified	0.000	0.000	0.000	0.000	0.000
spt	I	missed	0.010	0.000	0.011	0.106	–
		falsely identified	0.000	0.237	0.000	0.088	–
ice	I	missed	0.010	0.000	0.006	0.109	–
		falsely identified	0.000	0.000	0.011	0.001	–

as introduced in chapter 6. The model output time series do not exhibit any areawise significant points. The network transitivity of the tree ring model output shows a similar variability as the network transitivity of the input temperature with higher values corresponding to lower-dimensional dynamics during the MCA and lower values corresponding to higher-dimensional dynamics during the Little Ice Age (LIA). Also, it should be noted that the variability evident from the wRNA results of the tree ring model shows a comparable variability to the results obtained from the real-world data from the corresponding location studied in chapter 6 for times starting around the onset of the LIA. For earlier times, the transitivity values differ, which might be related to the shorter time span covered by the real-world data set and the limited data availability for earlier times in this data set.

As a first step towards quantifying the influence of the proxy system models on detecting areawise significant values of the network transitivity, we evaluate the fraction of falsely identified and missed significant points in the different proxy models for the different input time series in table 7.7. For the tree ring, the lake sediment, and the ice core model, missed significant points are more common than falsely identified significant points, with the only exceptions being the Lorenz input for the tree ring model and the Rössler input for the ice core model. Still, the ice core model seems to best reproduce past climate variability.

The speleothem model shows both falsely identified and missed significant points. In particular, these high fractions of falsely identified and missed significant points confirm that the Juxtlahuaca data set studied in chapter 6 does not seem to be well-suited for an analysis with wRNA. As other speleothem data sets, especially from Asia, have already been successfully used to characterise past climate variability with recurrence based measures (Donges et al., 2015a; Eroglu et al., 2016), a further

study of the role that the cave boundary conditions play for reliably applying the analysis framework to speleothem data is of great importance. In appendix D.3, we repeated the analysis for the speleothem model when tuning the model parameters to the conditions of Dongge cave (Wang et al., 2005) from Asia. For this setting, the average temperature and the mean aquifer transit time are smaller. We find that in this case, we still get both missed and falsely identified significant points. However, to draw conclusions about the general suitability of the archive, more systematic studies, in particular with respect to the mean aquifer transit time, have to be performed.

7.5. Discussion and conclusions

In this chapter, we have evaluated the suitability of wRNA for detecting dynamical anomalies in time series from different palaeoclimate proxy archives. For this, we used the concept of proxy system modelling and created artificial input time series corresponding to GWN, an AR(1) process, and the x-component of the non-stationary Lorenz and Rössler systems. Additionally, we used temperature and precipitation data from the LMR project (Hakim et al., 2016; Tardif et al., 2019). We then processed the input time series through proxy system models for tree ring widths, brGDGTs in lake sediments, and oxygen isotope ratios of speleothems and ice cores to compare time series properties and the results of wRNA for the input and output time series.

All tree ring model output time series showed a significant increase in the skewness of the time series distribution as compared to the input time series which can be explained by the thresholding within the model. The autocorrelation functions and power spectral densities closely follow the corresponding temperature input. In the wRNA results, less areawise significant points were apparent compared to the results for the input time series. That is, processing data through the tree ring model prevents significant anomalies to be detected.

For the studied lacustrine proxy, we observed that the skewness of the distributions of the time series differs for the model system and LMR input which might be related to a different reaction of the benthic mixing for different input distributions. In most cases, we observe larger decorrelation times than for the input time series. For the wRNA, we did not see any falsely identified significant points, instead, some significant points were missed.

For the speleothem model, the skewness of the time series distributions changed significantly except for the GWN input, which might again be related to different filtering effects of the model for different distributions of the input time series. We observed highly increased decorrelation times in the autocorrelation function. In the wRNA results, we found both missed and falsely identified significant points. Particularly the falsely identified significant points may cause problems in the analysis and interpretation of real speleothem data.

The ice core model also exhibits changes in skewness for the non-stochastic input, which is probably related to the filtering of the input signal during the diffusion within the core. We observed slightly increased decorrelation times and correspondingly

less power in the higher frequencies of the power spectral density. For wRNA, some falsely identified significant and some missed significant points were apparent. Still, the results of the input and output time series showed a better correspondence than for the other models.

In summary, we found that time series of tree ring width and brGDGTs in lake sediments have problems with missing areawise significant points, while the isotopic composition of speleothems has mainly problems with falsely identified significant points. Time series of the isotopic composition of ice show a good correspondence to the respective input even though some areawise significant points are missed. These finding help improving the interpretation of wRNA results for real-world applications. Thus, with respect to the results obtained in chapter 6, we conclude that the corresponding results for the tree ring width indices and the isotopic composition of the ice core likely show dynamical imprints of past climate variability. For the isotopic composition of the speleothem, we did not get any areawise significant results even though, from the results obtained in this chapter, we would rather expect an increased number of detected significant points. As no proxy system model for the red colour intensity of a varved lake sediment was available, we cannot relate the results obtained here to the data from Laguna Pallcacocha.

Future work should, on the one hand, comprise the study of alternative proxy system models with this framework. In particular, the development of proxy system models for more lacustrine proxy variables will complement the improved understanding of the suitability of wRNA for these types of data. Also, sensitivity studies for the different model parameters are of interest to better interpret results obtained with wRNA for a given real-world data set and to understand regional differences. This concerns especially the mean aquifer transit time of speleothem model which can, for real data, be estimated by cave monitoring. On the other hand, including dating and measurement uncertainties in the proxy system models and in the further analyses will increase the credibility of the obtained results.

Additionally, studying properties of the analysed time series can serve as a starting point to judge the suitability of wRNA for other data. The study of time series that are related by static transformations but exhibit different probability density functions can give additional insights into systematic biases introduced by the proxy system models. Also, exploring the relation between the autocorrelation of a time series and corresponding resulting network properties (as for example studied in Zhang et al. (2017) for the exponent of the degree distribution of visibility graphs) can provide additional information on the role of the different archives for wRNA. More generally, the effect of different non-linear filters (which the different proxy system models basically are) should be studied more systematically. In particular, the theory of non-linear observability can provide additional insights by identifying the processing through the proxy system model with the creation of a new observable. The choice of observable has already been shown to influence results of recurrence quantification analysis (Portes et al., 2014) and recurrence network analysis (Portes et al., 2019). Taken together, such considerations will help working out the role that different palaeoclimate archives play for reliably characterising past climate variability.

Chapter 8.

Summary: Application of analysis framework

The second part of this thesis was devoted to applications of the analysis framework of windowed recurrence network analysis (wRNA) and windowed scale-specific recurrence network analysis (wssRNA) to detect and characterise dynamical anomalies in past climate variability in proxy time series from different palaeoclimate archives. In particular, we focused on two aspects. First, we started exploring the non-linear past climate variability on both American continents and second, we addressed the question whether proxy time series from different archives are equally well suited for tracking past climate dynamics with the analysis framework.

In a first step, we analysed four palaeoclimate proxy time series from North and South America. We focused on the American continents because particularly the southern part has been underrepresented in previous studies of past climate variability, even though it is very vulnerable with respect to recent climate change (Villalba et al., 2009). Also, we focused on climate variability within the last 2000 years due to the availability of high-resolution proxy data and the relevance of this period for modern societies (Mann, 2007).

We started by presenting the results for the red colour intensity data set from Laguna Pallcacocha in Ecuador and the speleothem oxygen isotope ratios from the Juxtlahuaca cave in Mexico for different phase space reconstruction approaches and respectively varying embedding parameters. We found that uniform time delay embedding and derivative embedding with the discrete Legendre polynomials give comparable results, while derivative embedding with moving Taylor Bayesian regression only partially agrees with the other results. This confirms the results for the model system presented in chapter 3. Also, for the Laguna Pallcacocha data set, we found relatively robust results when varying the embedding parameters within the different approaches, which is not the case for the Juxtlahuaca data set. Thus, these results show that not all data sets are equally well suited for wRNA.

We then restricted ourselves to time delay embedding and applied the developed analysis framework of wRNA and wssRNA in combination with the areawise significance test to all four data sets. That is, we additionally considered the tree ring width index chronology from eastern Canada and the oxygen isotope ratios chronology from Quelccaya ice cap in the Peruvian Andes. As already expected from the results for

the varying embedding parameters, we did not find any areawise significant patches within the results of the speleothem data set from Juxtlahuaca cave.

For the other three data sets, we identified areawise significant low values of the network transitivity centred around the end of the Medieval Climate Anomaly (MCA), extending further back in time for the lake sediment and ice core data. This might indicate that the termination of the MCA started earlier in South America than in Canada. The network transitivity then showed an opposed variability for the lake sediment and the ice core results, suggesting locally different imprints of the Little Ice Age and the current warm period. For the tree ring width data, we only found this one patch of areawise significant values of the network transitivity that not only coincides with the end of the European MCA but also follows the Samalas eruption in 1257 AD. Interestingly, when varying the embedding delay (appendix C.2), we observed areawise significant patches around the Samalas eruption for larger delay times and areawise significant patches around the Tambora eruption (1815 AD) for shorter delay times. This may possibly be related to reactions at different time scales to the different explosive volcanic eruptions.

To have a closer look at the system dynamics at different time scales, we additionally applied wssRNA to the four data sets. For the tree ring data, this approach did not provide any additional insights as only two very small areawise significant patches were detected. For the lake sediment data, we found a large fraction of areawise significant analysis results but could not extract any particular pattern. Applying a more general fitting model for the decorrelation lengths as a function of the scale might yield better interpretable results and a higher confidence bound of the areawise test. For the speleothem and the ice core data sets, wssRNA was able to resolve more details. In particular, we found areawise significant patches of high values of the network transitivity for large (speleothem) and intermediate (ice core) scales, respectively.

To more systematically study the role of the archive for characterising past climate variability with the developed framework, we employed proxy system models. Proxy system models simulate the evolution of a proxy variable over time given the climatic input variables and the local boundary conditions of the corresponding archive. We used four different models to simulate the tree ring width (Tolwinski-Ward et al., 2011), lacustrine branched glycerol dialkyl glycerol tetraethers (Dee et al., 2018), speleothem oxygen isotope ratios, and ice core oxygen isotope ratios (Dee et al., 2015). To tune the model parameters, we used exemplary real-world data sets and created artificial climate input time series of temperature, precipitation, and isotopic composition of precipitation. We then analysed the input time series using the framework of wRNA and compared the results to corresponding results for the model output time series.

For the lake sediment, the speleothem, and the ice core archive, the model output time series were low-pass filtered due to the bioturbation, aquifer transit time, and diffusion, respectively, while for the tree ring archive such an effect was not present. For the wRNA results, we found that the tree ring and lake sediment archives sometimes miss areawise significant anomalies that are present in the input. For

the speleothem archive, we found areawise significant patches that are not present within the input, thus, when interpreting the results from this archive for real-world time series, the possibility of false positive significant analysis results has to be taken into account. For the results as recorded in the ice core archive, we found the best agreement with the input results making this archive especially well-suited for our analysis framework. Generally, we have shown that different filtering processes lead to different phenomena for an analysis with wRNA which should, independent of the palaeoclimate application, be studied in further detail in the future.

In the light of the results from chapter 7 for the tree ring and the ice core archives, the identified anomalies in the eastern Canada tree ring width data and the oxygen isotope ratios from Quelccaya ice cap (chapter 6) can be assumed to represent actual anomalies of the climate variability. As we did not consider the red colour intensity as a proxy variable for the lake sediment archive, we cannot draw any conclusions about the reliability of the detected anomalies in the Laguna Pallcacocha data. To resolve the discrepancy between no detected areawise significant anomalies in the Juxtlahuaca cave data set and the high rates of falsely identified anomalies in the speleothem model output, more systematic studies on the role of the cave boundary conditions are required.

Summing up, in this second part of the thesis, we found that not all data sets are equally well suitable for being analysed with the proposed framework. In particular, local boundary conditions, the climate sensitivity of the data under study, and the archive play a role for how well the climate signal is reproduced. The implications of these results for future work are discussed in detail in chapter 9.

Chapter 9.

Conclusions

In this thesis, we aimed at advancing the framework of windowed recurrence network analysis (wRNA) for detecting and characterising dynamical anomalies in time series from different palaeoclimate proxies. For this, independently of the application to palaeoclimate data, we tested and further developed parts of the framework, namely phase space reconstruction from measured univariate time series and significance testing. Then, to take a first step towards characterising non-linear past climate variability on both American continents, we applied the framework to four real-world palaeoclimate time series from North and South America and identified regional similarities and differences within the last two millennia. Finally, to better understand the relation between the results of the different proxy time series and actual climate variability, we systematically studied the implications of processing climatic input through proxy system models prior to applying the analysis framework.

9.1. Contributions of this thesis

Besides providing a detailed introduction into the existing framework of wRNA, the first part of the thesis was devoted to test and improve the routines of phase space reconstruction and significance testing. The second part then dealt with the application to palaeoclimate data and focused on the suitability of the framework for inferring information about past climate variability from different palaeoclimate archives. In the following, we shortly summarise the corresponding results and highlight their implications for the field. Possible modifications and ideas for future work are provided in section 9.2.

Phase space reconstruction

In a first step, we systematically studied different approaches for phase space reconstruction when the available data are non-uniformly sampled and contaminated with noise. We compared the concept of uniform time delay embedding to that of derivative embedding for three different ways of estimating derivatives, i. e., central difference quotients, discrete Legendre polynomials, and moving Taylor Bayesian regression. To quantify the quality of the reconstructions, we considered the paradigmatic Rössler and Lorenz systems for varying noise levels and shapes of the sampling interval distribution and transformed the embedded time series into recurrence networks. By

comparing the network transitivity and the average shortest path length to corresponding reference values obtained from recurrence networks of the original attractors, we found that there is not one overall optimal approach for phase space reconstruction. Generally, both time delay embedding with linearly interpolated data and derivative embedding with discrete Legendre polynomials for cubic spline interpolated data performed reasonably well. When additionally applying the different reconstruction approaches in combination with wRNA to a non-stationary Rössler system, we found similar results.

This study highlights the importance of a proper reconstruction of the system's phase space prior to further recurrence-based analyses. In particular, we emphasise that comparing several phase space reconstructions by varying the reconstruction approach or the embedding parameters can improve the reliability of the analysis results. If the data are non-uniformly sampled, combining uniform time delay embedding with cubic spline interpolation can sometimes improve the results. For derivative embedding, the resulting coordinates should be scaled to unit variance and more sophisticated derivative estimation approaches should be preferred. For the discrete Legendre polynomials, the number of neighbours p included to each side to estimate the derivatives should be chosen of the order of the embedding dimension or slightly larger.

Related publication Lekscha and Donner (2018, P1)

Areawise significance tests

We then turned to the problem of significance testing when intrinsic correlations within the analysis results lead to patches of possibly false positive significant points. Based on the areawise significance test for the wavelet spectrogram presented in Maraun et al. (2007), we developed a generalised areawise significance test relying on a numerical estimation and linear fitting of the intrinsic correlations with respect to a chosen null model. This test can be applied in combination with any analysis method and, for the cases of wRNA and windowed scale-specific recurrence network analysis (wssRNA) applied to the non-stationary Rössler system, successfully reduced the number of significant points. In addition, our areawise significance test provides confidence bounds for the detected anomalies.

The introduction of this areawise test contributes to the development of a reliable framework of wRNA as it considerably improves the interpretation of detected dynamical anomalies by only highlighting the most relevant features of the data. Due to its generality, it has the potential to improve the interpretation of the results of many other analysis methods as well. In combination with the results for the phase space reconstruction, the framework as summarised in chapter 5 is well suited for characterising the dynamics of non-linear systems from many different disciplines, such as, for example, medicine, geology, climate, and finance.

Related publication Lekscha and Donner (in press, P2)

Analysing palaeoclimate data with wRNA

We then applied the analysis framework to four real-world palaeoclimate proxy time series from four different archives. By varying the phase space reconstruction approach, we confirmed the results from chapter 3 that uniform time delay embedding and derivative embedding with discrete Legendre polynomials yield comparable results. We also noted that not all data sets give robust results when varying the embedding parameters and methods and thus, that not all data sets are equally well suited for this type of analysis. Our finding was confirmed when applying the framework for varying window widths of wRNA where the areawise significance test did not yield any areawise significant points for the studied speleothem data set. The other three data sets provided insights into past climate variability on the American continents of the last one to two thousand years which, based on the limited number of studied data, show synchronous dynamical anomalies particularly around the end of the Medieval Climate Anomaly but also reveal regional differences for some periods of time. Additionally applying wssRNA has been found to be a valuable tool for obtaining complementary scale-resolved information about climate variability.

These results serve as a first step towards a more systematic characterisation of non-linear past climate variability in North and South America and highlight that local or regional effects can not be neglected when characterising past climate dynamics.

Related publications Lekscha and Donner (2018, P1), Lekscha and Donner (in press, P2)

Proxy system model perspective on wRNA

When studying palaeoclimate proxy data from different archives, the question whether all those data are equally well suited for inferring information on past climate variability using the developed framework of wRNA naturally arises. To systematically study and to improve the interpretation of results obtained from real-world data, we employed proxy system models for tree ring width, branched glycerol dialkyl glycerol tetraethers (brGDGTs) in lake sediments, and oxygen isotope ratios in speleothems and ice cores. For different artificial climate input time series, we compared time series properties and wRNA results of input and model output. We found that tree rings and brGDGTs rather miss dynamical anomalies present in the input data, while oxygen isotope ratios in speleothems additionally introduce anomalies that are not present in the input. Oxygen isotope ratios in ice cores, however, seem to best represent the dynamics of the climate input even though some significant anomalies may be missed.

These insights play a major role when interpreting the results of wRNA for real-world data from the corresponding proxies. They also stress the importance of continuously developing and improving proxy system models for advancing our understanding of past climate variability.

Related publication Lekscha and Donner (submitted, P3)

Summary of thesis contributions

To sum up, with this thesis, we advanced the development of a reliable analysis framework of wRNA. In particular, we provided insights into the role of the choice of the phase space reconstruction approach and embedding parameters (chapter 3) and developed an areawise significance test that improves the interpretation of results when intrinsic correlations within the analysis results play a non-negligible role (chapter 4). We also emphasised the importance of checking the robustness of the analysis results before drawing any conclusions by varying analysis parameters such as the window width of the windowed analysis and put forward the use of wssRNA in addition to traditional wRNA. This framework has been proven to be particularly useful for detecting non-stationarity and characterising the dimensionality of the dynamics from a measured univariate time series of possibly only relatively few data points.

By applying the framework to palaeoclimate time series, we promote the use of non-linear methods in this field even though not all real-world data sets are equally well suited for this type of analysis. On the one hand, local boundary conditions may lead to non-significant signals of recorded data as it was the case for the speleothem data set studied in chapter 6. On the other hand, the type of archive and proxy variable plays a role for the detection of actual climate variability with this framework as demonstrated in chapter 7 for four distinct proxy variables from different palaeoclimate archives. However, with these limitations in mind, we were able to start exploring the non-linear variability of the climate in North and South America.

9.2. Outlook

The above considerations show that applying non-linear methods in general, and the developed analysis framework of wRNA in particular, have a great potential for inferring information on past climate variability that is complementary to the information obtained in classical reconstructions of past climate conditions. Still, such methods are not very present in the corresponding communities. Thus, a further development and promotion of reliable analysis frameworks that include objective routines for choosing the analysis parameters and the provision of corresponding analysis tools is of utmost importance.

As a next consequent step, the concept of non-uniform time delay embedding for phase space reconstruction deserves additional attention because it offers the perspective of better capturing different time scales of the system's dynamics. The unified approach put forward in Pecora et al. (2007) provides, in our opinion, the most objective and physics based available algorithm to reconstruct the phase space from uni- or multivariate measured data. But, as currently no implementation is publicly available, this method has not yet received much attention for practical applications. We started implementing different approaches for phase space reconstruction and

corresponding parameter estimations (including the approach presented in Pecora et al. (2007) for non-uniform time delay embedding) and plan to provide a corresponding open-access software package (https://github.com/hkraemer/Embedding-methods, still under construction).

Another important aspect for the further development of the analysis framework concerns the fitting model of the intrinsic correlations of the areawise significance test. So far, only a linear fitting model is applied but as observed for wssRNA, this linear model can not always be assumed to be appropriate. Thus, a generalisation of this step of the areawise significance test can be expected to provide improved confidence bounds.

In order to further establish wssRNA, more systematic studies on how to filter the time series before applying wRNA are required. Apart from wavelet filtering, also moving average filtering (Smith, 2003), the empirical mode decomposition (Huang et al., 1998), and singular spectrum analysis (Broomhead and King, 1986; Elsner and Tsonis, 1996) are possible candidates. When choosing wavelets, more research on the influence of the choice of the mother wavelet and parameters such as the bandwidth or the centre frequency on the analysis results are of great interest. Also, an objective criterion to choose the scales at which the system is investigated should be identified.

Eventually, the analysis framework should be complemented by explicitly including uncertainties in the analysis, for example, following the ideas in Goswami et al. (2014) and Goswami et al. (2018). This is particularly relevant in the palaeoclimate context as dating uncertainties can often not be neglected.

To further advance the use of the framework for studying past climate variability, the systematic study of the influence of the archive for characterising climate dynamics should be extended by taking into account proxy system models for additional archives and proxy variables and performing sensitivity tests with respect to the model parameters. Also, the relation between the implications for the wRNA results of the non-linear filtering of the climate signal in the proxy archive and the theory of observability should be explored in more detail (Letellier et al., 1998; Aguirre et al., 2008; Portes et al., 2014; Portes et al., 2019).

As all studies on non-linear past climate variability rely on the availability of high quality palaeoclimate data such as, for example, in the PAGES 2k database (PAGES2k-Consortium, 2017), such databases should be further extended and maintained. For this, the assessment and implementation of quality standards for the different proxy archives following the ideas put forward in Esper et al. (2016) for tree rings should be continuously promoted. Then, a systematic analysis of the available data can be performed using the framework developed in this thesis. In order to interpret the analysis results with respect to archive type, proxy sensitivity, local boundary conditions, regional effects, and global trends, the use of clustering algorithms or machine learning techniques might be of particular interest, especially for pattern identification (Hastie et al., 2001; Alpaydin, 2014). With this, many different problems can be considered, for example, the imprints of volcanic forcing of different eruptions in tree ring data could be explored in more detail.

Finally, a naturally arising subsequent step when analysing the available palaeoclimate data is, in analogy to the concept of climate networks (Tsonis et al., 2006; Donges et al., 2009; Radebach et al., 2013; Wiedermann et al., 2016), to not only consider single time series within the analysis framework, but to also take into account correlations between the proxy data at different locations and the corresponding analysis results. That this can yield interesting insights into the development of past modes of climate variability and teleconnection patterns has been demonstrated, for example, in Franke et al. (2017). Also the framework of recurrence based time series analysis comprises natural extensions for correlating multiple time series such as cross recurrences and joint recurrences (Marwan et al., 2007; Donner et al., 2015). In this respect, the possibility to test detected correlations for causality using sophisticated methods as recently reviewed in Runge et al. (2019) offers a particularly relevant perspective for advancing the understanding of the Earth's climate system.

Appendix

Appendix A.

Additional information: Phase space reconstruction approaches

A.1. Derivatives and discrete Legendre polynomials

We here derive equation (3.6) which relates the derivatives of a time series at a point x_i to a weighted sum of $2p+1$ points around this reference point with the weights being the discrete Legendre polynomials $r^{(i)}_{j,p,n}$ (equation (3.8)). This derivation is adapted from Gibson et al. (1992) for the case of non-uniformly sampled data.

Given a discrete set of univariate data $\{x_i = x(t_i)\}_{i=1}^{N}$ with non-uniform sampling intervals $\Delta t_{i,n} = t_{i+n} - t_i$, we can apply a discrete linear filter

$$\omega_j(t_i) = \sum_{n=-p}^{p} r^{(i)}_{j,p,n} x(t_i + \Delta t_{i,n}). \tag{A.1}$$

Performing a Taylor expansion of equation (A.1) for small $\Delta t_{i,n}$ yields

$$\omega_j(t_i) = \sum_{n=-p}^{p} r^{(i)}_{j,p,n} \left[\sum_{\nu=0}^{\infty} \frac{(\Delta t_{i,n})^\nu}{\nu!} \frac{d^\nu}{dt^\nu} x_i \right] \tag{A.2}$$

$$= \sum_{\nu=0}^{\infty} \frac{1}{\nu!} \frac{d^\nu}{dt^\nu} x_i \sum_{n=-p}^{p} (\Delta t_{i,n})^\nu r^{(i)}_{j,p,n}. \tag{A.3}$$

To derive an expression for $\omega_j(t_i)$ that is proportional to the jth derivative, the filter function $r^{(i)}_{j,p,n}$ has to be orthogonal to $(\Delta t_{i,n})^\nu$ for $\nu < j$, that is, the relation

$$\sum_{n=-p}^{p} (\Delta t_{i,n})^\nu r^{(i)}_{j,p,n} = 0 \tag{A.4}$$

has to hold. The discrete Legendre polynomials defined by the recursion relation (3.8) are mutually orthonormal filters satisfying

$$\sum_{n=-p}^{p} r^{(i)}_{k,p,n} r^{(i)}_{l,p,n} = \delta_{kl} \tag{A.5}$$

with δ_{kl} being the Kronecker Delta. Thus, choosing the discrete Legendre polynomials as filters assures that condition (A.4) holds. Like this, the Taylor expansion (A.3) is, to leading order, reduced to

$$\omega_j(t_i) = \frac{1}{j!}\frac{d^j}{dt^j}x_i \sum_{n=-p}^{p} (\Delta t_{i,n})^j r_{j,p,n}^{(i)}. \tag{A.6}$$

When equating this result and equation (A.1) we arrive at the desired result (3.6)

$$\frac{d^j}{dt^j}x_i \approx \frac{j!}{c_{j,p}(\Delta t_{i,n})} \sum_{n=-p}^{p} r_{j,p,n}^{(i)} x_{i+n}. \tag{A.7}$$

A.2. Parameter choices for the phase space reconstruction appraoches

We here present additional results used for deciding which model parameters (delay time τ for time delay embedding and number of neighbours p used to estimate derivatives for the discrete Legendre polynomials) and which type of sampling (non-uniform, uniform using linear/ cubic spline/ moving Taylor Bayesian regression (MoTaBaR) interpolation) performs best for each approach. As for all those scenarios, we vary the embedding dimension, the noise level, the shape of the non-uniform sampling interval distribution, and additionally consider the network transitivity and the average shortest path length, we only show selected results.

Time delay embedding

For time delay embedding, we first have to choose the delay time τ. Figure A.1 exemplarily compares the relative differences to the reference network transitivity for time delay embedding with linear and cubic spline interpolation when varying the delay times for embedding dimension $m = 3$, standard deviation of the noise $\sigma = 1.0$, and shape of the sampling interval distribution $k = 1.0$. We choose delay times $\tau = 2\langle dt \rangle$ for the Lorenz and $\tau = \langle dt \rangle$ for the Rössler system which is on the one hand in accordance with the first root of the autocorrelation function and on the other hand performs reasonably well with respect to the reference solutions for all dimensions and measures.

After having chosen the delay time, we have to decide whether to use the linearly or the cubic spline interpolated data. Figures A.2 and A.3 show the performance of the two interpolation methods when varying the noise level and the shape of the sampling distribution for the Lorenz and the Rössler system, respectively. We see that depending on the system and the parameters, the approaches perform differently well. This is also the case when taking into account the results for the other dimensions and the average shortest path length. We decide to use the linear interpolation to compare time delay embedding to derivative embedding because this is the most

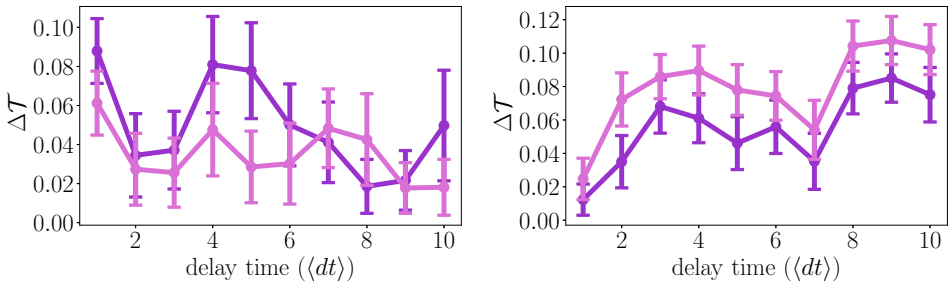

Figure A.1.: Mean (points) and standard deviation (errorbars) of the relative difference to the reference transitivity for the Lorenz (left) and the Rössler (right) system using time delay embedding for varying delay times τ and embedding dimension $m = 3$. The dark violet line corresponds to cubic spline interpolation and the light violet line to linear interpolation. The standard deviation of the noise is $\sigma = 1.0$ and the shape parameter of the sampling distribution is $k = 1.0$.

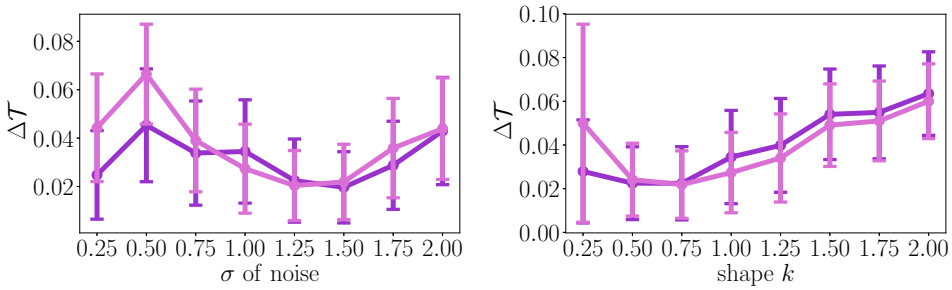

Figure A.2.: Mean (points) and standard deviation (errorbars) of the relative difference to the reference transitivity for the Lorenz system using time delay embedding for delay time $\tau = 2\,\langle dt \rangle$ and embedding dimension $m = 3$. The dark violet line corresponds to cubic spline interpolation and the light violet line to linear interpolation.

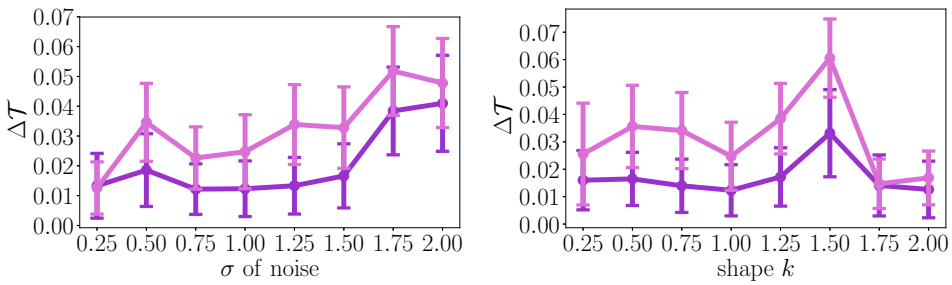

Figure A.3.: Same as in figure A.2 but for the Rössler system with delay time $\tau = \langle dt \rangle$.

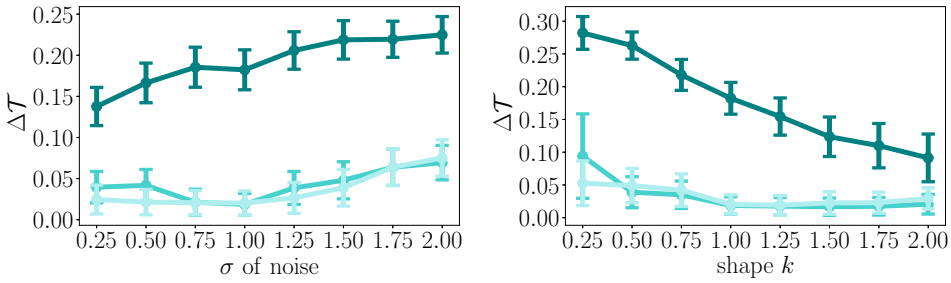

Figure A.4.: Mean (points) and standard deviation (errorbars) of the relative difference to the reference transitivity for the Lorenz system using derivative embedding with central differences and embedding dimension $m = 3$. The dark cyan line corresponds to non-uniform sampling, the medium cyan line to linear interpolation, and the light cyan line to cubic spline interpolation.

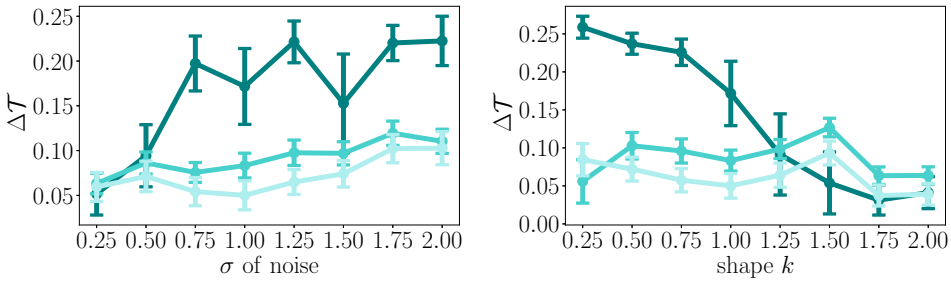

Figure A.5.: Same as in figure A.4 but for the Rössler system.

commonly used approach in applications. But we note that in some cases, using cubic spline interpolation instead of linear interpolation can be of advantage.

Derivative embedding using central differences

For derivative embedding with central differences, we do not have to choose any model parameters, instead, we have to choose whether to use the results obtained directly from the non-uniformly sampled data or from uniformly sampled data obtained by linear or cubic spline interpolation. As the results are generally much better when scaling the reconstructed coordinates to unit variance, we here only show the corresponding results.

Figures A.4 and A.5 show the performance of the different samplings for the network transitivity when varying the standard deviation of the noise σ and the shape parameter k of the sampling distribution for the two model systems. As expected, the results for the non-uniformly sampled data show a particular dependence on the noise level and the shape of the sampling distribution. We observe that cubic spline interpolation performs best in almost all cases and thus, use this interpolation

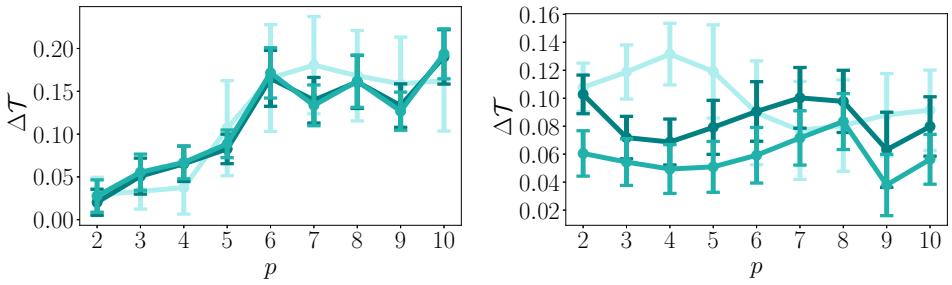

Figure A.6.: Mean (points) and standard deviation (errorbars) of the relative difference to the reference transitivity for the Lorenz (left) and the Rössler (right) system using derivative embedding with discrete Legendre polynomials for varying values of p and embedding dimension $m = 3$. The dark cyan line corresponds to linear interpolation, the medium cyan line to cubic spline interpolation, and the light cyan line to non-uniform sampling. The standard deviation of the noise is $\sigma = 1.0$ and the shape parameter of the sampling distribution is $k = 1.0$.

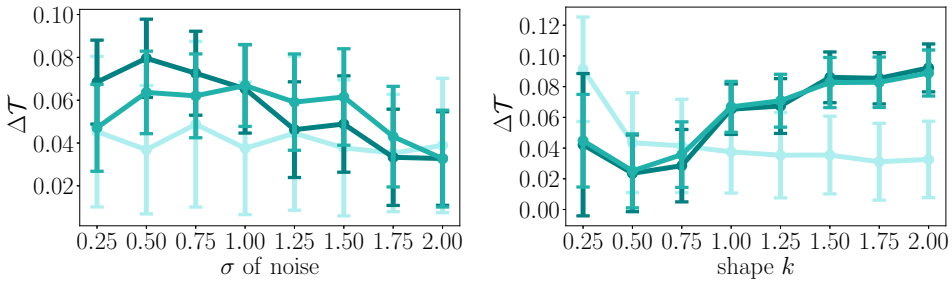

Figure A.7.: Mean (points) and standard deviation (errorbars) of the relative difference to the reference transitivity for the Lorenz system using derivative embedding with discrete Legendre polynomials for $p = 4$ and embedding dimension $m = 3$. The dark cyan line corresponds to linear interpolation, the medium cyan line to cubic spline interpolation, and the light cyan line to non-uniform sampling.

method for comparing derivative embedding with central differences to the other phase space reconstruction approaches.

Derivative embedding using discrete Legendre polynomials

For derivative embedding with discrete Legendre polynomials, we first note that scaling the coordinates to unit variance is of advantage for the Lorenz and of disadvantage for the Rössler system, such that we use the scaling only for the Lorenz system. We then have to choose the value of p, that is, the number of neighbours to each side that is taken into account for estimating the derivatives. Figure A.6 shows the performance of the network transitivity for varying values of p for embedding dimension $m = 3$, noise standard deviation $\sigma = 1.0$, and shape parameter $k = 1.0$. For the Lorenz system, the performance is best for small values of p, while for the Rössler system

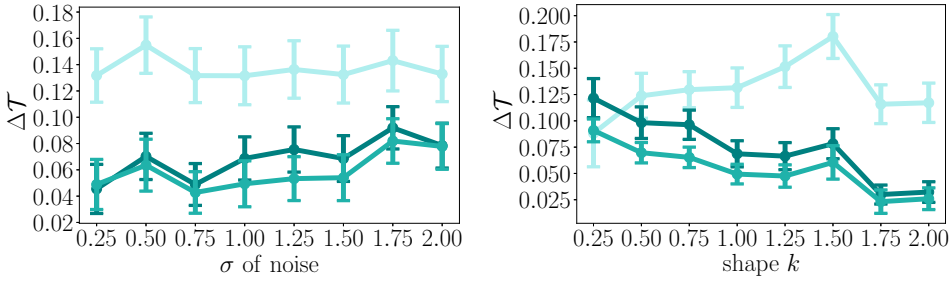

Figure A.8.: Same as in figure A.7 but for the Rössler system.

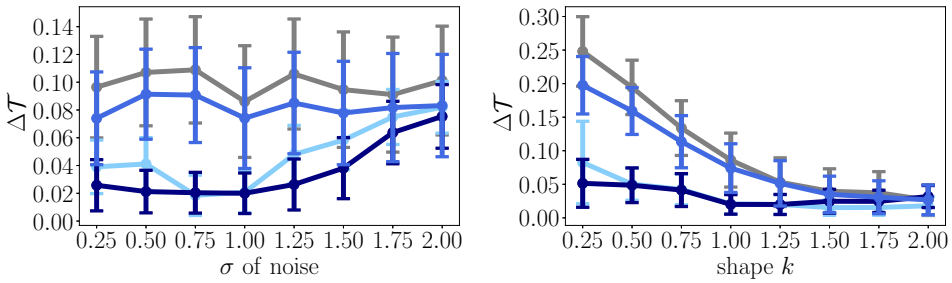

Figure A.9.: Mean (points) and standard deviation (errorbars) of the relative difference to the reference transitivity for the Lorenz system using derivative embedding with MoTaBaR and embedding dimension $m = 3$. The grey line corresponds to non-uniform sampling, the dark blue line to cubic spline interpolation, the medium blue line to the internal MoTaBaR interpolation, and the light blue line to linear interpolation.

the difference to the reference transitivity of the interpolated solutions has minima at $p = 4$ and $p = 9$. When considering all results, we choose to use the value of p dependent on the embedding dimension as for higher derivatives, more points should be taken into account. Here, we choose $p = 4$ of dimension $m = 3$ and $p = 6$ for dimensions $m = 4$ and $m = 5$, but in general, we think that the choice of $p \approx m + 1$ is well justified by the results.

Next, we have a look at the performance of the non-uniformly sampled reconstructions and the interpolated reconstructions. Figures A.7 and A.8 show the difference to the reference transitivity depending on the noise level and the sampling distribution of the time intervals between observations. We see that the results for non-uniform sampling show small values of $\Delta\mathcal{T}$ for the Lorenz but large values for the Rössler system. The two interpolated solutions behave very similarly but the cubic spline interpolation mostly outperforms the linear interpolation. Thus, for the comparison between the approaches, we use the results obtained with cubic spline interpolation.

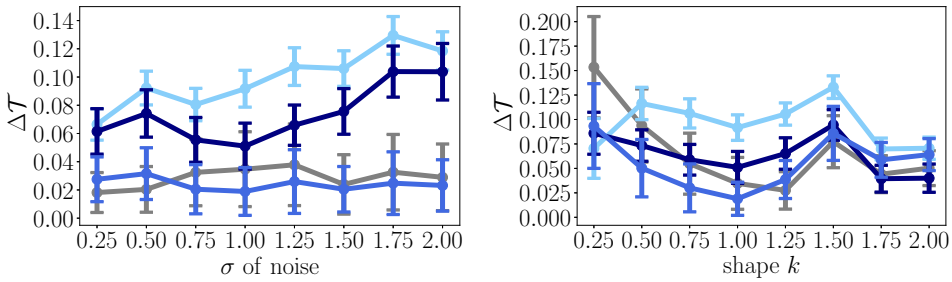

Figure A.10.: Same as in figure A.9 but for the Rössler system.

Derivative embedding using MoTaBaR

For derivative embedding with MoTaBaR, we also note that scaling the coordinates to unit variance generally improves the results. To compare the results for the non-uniformly sampled case to the differently interpolated cases, figures A.9 and A.10 show the performance of the network transitivity for varying standard deviation of the noise and varying shape parameter of the gamma distribution for all those cases. We see that for the Lorenz system, cubic interpolation performs best, while for the Rössler system, the internal interpolation routine of MoTaBaR performs best. Taking into account the other dimensions and the results for the average path length, we decide to use the internal MoTaBaR interpolation routine to compare the results of the MoTaBaR phase space reconstruction to the other reconstruction approaches.

Appendix B.

Additional information: Areawise significance tests

We here complement the results of chapter 4 for the areawise significance test in combination with windowed recurrence network analysis (wRNA) and windowed scale-specific recurrence network analysis (wssRNA).

B.1. Windowed recurrence network analysis

We start with the wRNA of the non-stationary Rössler system as described in chapter 4 and present results for the average shortest path length $\mathcal{L}$ to supplement the insights obtained from the network transitivity.

Figure B.1 shows the decorrelation length as a function of the window width for the time and the window width domain. The fitting parameters and the confidence levels of the areawise significance test for the different null models are displayed in table B.1. We note that the values of the coefficient of determination for the average shortest path length are high even though not as high as for the network transitivity. Also, the confidence level for the null model of an autoregressive process of order 1 (AR(1) process) is low, that is, we do not discuss the results for this null model in the following. Possibly, a more general fitting model would result in estimates for the decorrelation length as a function of the window width that yield higher confidence levels for the areawise significance test.

Figure B.2 shows the analysis results of the wRNA with pointwise and areawise significance tests. We note that for the iterative amplitude-adjusted Fourier transform (iAAFT) null model, the patches of areawise significant points are considerably smaller than for the other null models and also than for the network transitivity. But particularly for the Gaussian white noise (GWN) null model, we see that the parameter regimes in which areawise significant point occur are identical to the regimes in which the network transitivity shows areawise significant results except that, for the average shortest path length, those patches appear at larger values of the window widths.

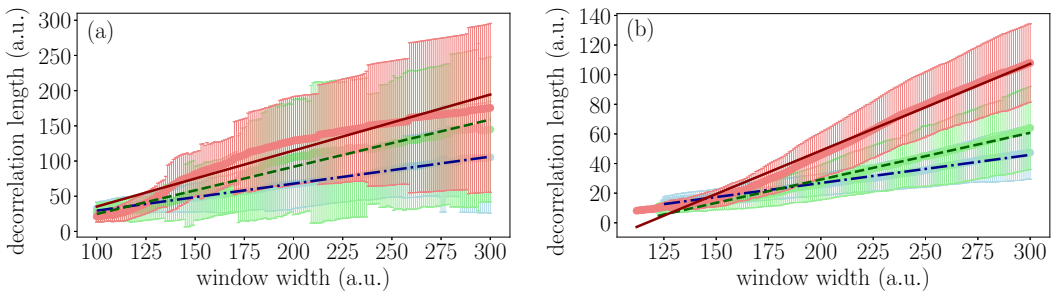

Figure B.1.: Mean (points), standard deviations (error bars), and linear fits (lines) of the decorrelation lengths as a function of the window width W for (a) correlations in the time domain of the results for the average shortest path length $\mathcal{L}$ of wRNA and (b) correlations in the window width domain for the non-stationary Rössler system using the three different null models: blue, dash-dotted: GWN; green, dashed: AR(1) process; red, solid: iAAFT null model.

Table B.1.: Parameters and coefficients of determination of the linear fits of the decorrelation length as a function of the window width for the average shortest path length of wRNA and corresponding significance levels for the different null models in the time and the window width domain.

null model	domain	m	n	R^2	s_{aw}	s_{pw}	s_{aw}
GWN	time	0.3838	−8.905	0.9950			
GWN	W	0.1901	−11.16	0.9898	0.99	0.95	0.94
AR(1)	time	0.6706	−42.28	0.9644			
AR(1)	W	0.3153	−33.83	0.9887	0.63	0.95	0.60
iAAFT	time	0.7957	−44.29	0.9426			
iAAFT	W	0.5857	−68.40	0.9871	0.85	0.95	0.81

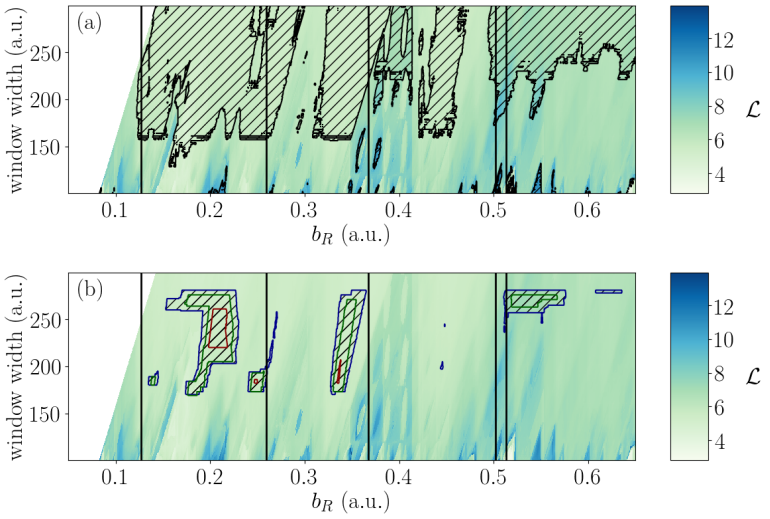

Figure B.2.: Average shortest path length $\mathcal{L}$ of wRNA (color coded) of the non-stationary Rössler system with (a) pointwise significance test using random shuffling surrogates and (b) areawise significance test (hatched contours). The test results for the GWN null model are shown by dark blue, the AR(1) null model by dark green, and the iAAFT null model by dark red contours. The vertical lines indicate the different regimes of the stationary system according to the bifurcation diagram in figure 4.1.

B.2. Windowed scale-specific recurrence network analysis

We now continue with the results of the average shortest path length for wssRNA. Details on the analysis framework can again be found in chapter 4.

In figure B.3, the resulting decorrelation lengths as a function of the scale for the average shortest path length obtained with wssRNA are displayed for the time and the scale domain. Table B.2 gives the fitting parameters for the linear fits of the decorrelation length as a function of the scale and the resulting confidence levels of the areawise significance test for the different null models. As for the network transitivity, the linear fitting model does not seem to be appropriate for wssRNA. But again, the confidence levels of the areawise significance test are high enough to justify the use of the linear model. We note that the dependence of the decorrelation lengths on the scale are similar for the different null models.

The results of the wssRNA for the average shortest path length and the pointwise and areawise significance test for the different null models are displayed in figure B.4. As before, we observe areawise significant patches of anomalously low and high values of the average shortest path length at similar regimes of the time-varying parameter b_R as for the network transitivity.

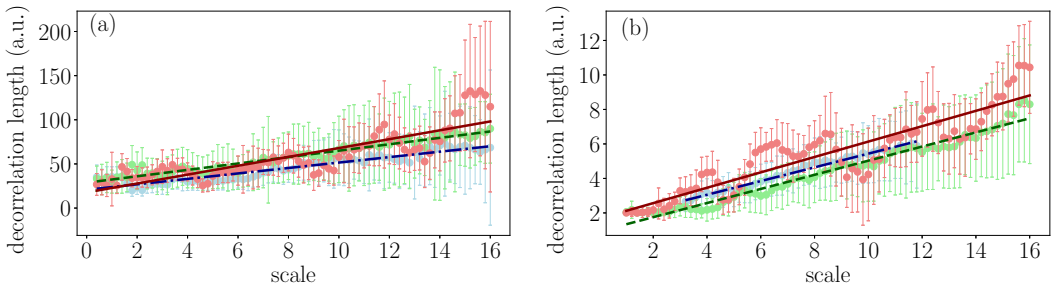

Figure B.3.: Same as in figure B.1 but for wssRNA and correlations in the time and scale domain as a function of the scale.

Table B.2.: Parameters and coefficients of determination of the linear fits of the decorrelation length as a function of the window width for the average shortest path length of wssRNA and corresponding significance levels for the different null models in the time and the scale domain.

null model	domain	m	n	R^2	s_{aw}	s_{pw}	s_{aw}
GWN	time	3.080	20.75	0.8845			
GWN	scale	0.3975	1.462	0.9815	0.96	0.95	0.91
AR(1)	time	3.629	28.73	0.9374			
AR(1)	scale	0.4095	0.9338	0.9671	0.89	0.95	0.85
iAAFT	time	5.021	17.78	0.7166			
iAAFT	scale	0.4460	1.676	0.8174	0.92	0.95	0.87

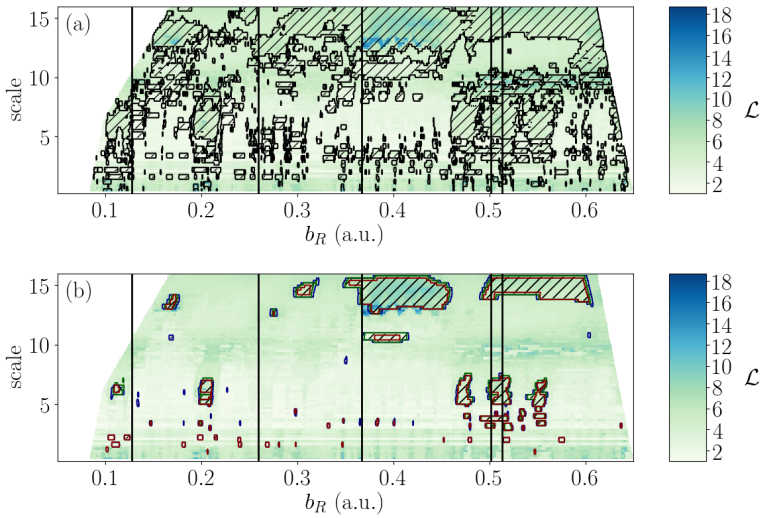

Figure B.4.: Same as in figure B.2 but for wssRNA and varying scales.

Appendix C.

Additional information: Analysing palaeoclimate data with wRNA

In this appendix, we provide additional information for chapter 6. That is, we show the fitting parameters for the areawise significance tests of the windowed recurrence network analysis (wRNA) and the windowed scale-specific recurrence network analysis (wssRNA) for the four proxy time series on the one hand and the results of the wRNA of the tree ring data set for varying choices of the delay time for time delay embedding on the other. Also, we provide wRNA results of data from the last millennium reanalysis (LMR) project.

C.1. Fitting parameters for areawise significance tests

Tables C.1 and C.2 give the fitting parameters and confidence levels of the areawise significance test for the four proxy time series for wRNA and wssRNA, respectively. Corresponding to the results obtained in chapter 4, we observe high values of the coefficient of determination for the linear fitting model for wRNA and lower values for wssRNA. As argued before, a more general approach for fitting the decorrelation length as a function of the scale might increase the confidence levels of the wssRNA.

Table C.1.: Parameters and coefficients of determination of the linear fits of the decorrelation length as a function of the window width for the network transitivity of wRNA and corresponding significance levels for the different proxy time series and the iAAFT null model in the time and the window width domain.

data	domain	m	n	R^2	s_{aw}	s_{pw}	s_{tot}
trw	time	0.2217	26.77	0.9813			
trw	W	0.3148	−15.74	0.9997	0.99	0.95	0.94
lak	time	0.3581	12.10	0.9980			
lak	W	0.2844	−0.4848	0.9999	0.84	0.95	0.80
spt	time	0.2605	21.28	0.9802			
spt	W	0.1834	14.50	0.9964	0.98	0.95	0.93
ice	time	0.4044	−1.072	0.9945			
ice	W	0.2958	−9.843	0.9989	0.99	0.95	0.94

Table C.2.: Parameters and coefficients of determination of the linear fits of the decorrelation length as a function of the scale for the network transitivity of wssRNA and corresponding significance levels for the different proxy time series and the iAAFT null model in the time and the scale domain.

data	domain	m	n	R^2	s_{aw}	s_{pw}	s_{tot}
trw	time	3.178	27.84	0.8692			
trw	scale	0.4971	−0.06078	0.8701	0.97	0.95	0.92
lak	time	3.915	28.12	0.8457			
lak	scale	0.8020	−0.3626	0.9140	0.89	0.95	0.85
spt	time	3.847	23.82	0.9018			
spt	scale	0.6317	−0.3764	0.8681	0.96	0.95	0.91
ice	time	3.942	23.36	0.9161			
ice	scale	0.3042	1.507	0.9285	0.94	0.95	0.89

C.2. Results for tree ring data for varying embedding delay

For the tree ring width time series, we provide additional results of the wRNA for varying delay times corresponding to the results obtained in publication P2 for the areawise significance test with respect to the null model of the autoregressive process of order 1 (AR(1) process). The parameters of the AR(1) process were fitted to the data according to equation (2.25) resulting in the choices $x(0) = 1.303$, $c = 0.2738$, $\rho = 0.7327$, and $\sigma_{\epsilon_t} = 0.1308$. The fitting parameters and confidence levels of the areawise significance test are shown in table C.3.

The results of the wRNA for the varying delay times are shown in figure C.1. For all delay times we observe a similar variability of the network transitivity with low values marking the end of the Medieval Climate Anomaly and high, but not areawise significant values before the onset of the Little Ice Age. For some choices of τ we do not observe any areawise significant patches, thus, the null hypothesis of the dynamics resulting from an AR(1) process cannot be rejected. Generally, for smaller values of the delay time, we find areawise significant patches of low values of the network transitivity around or after the Tambora eruption (1815 AD). For larger values of τ areawise significant patches are more centred around the Samalas eruption (1257 AD). This behaviour might indicate that reactions of the climate system took place at different time scales for the different eruptions as the different choices of the delay time reproduce different time scales of the system better. But, before drawing any final conclusions, this hypothesis has to be tested using more data sets.

Table C.3.: Parameters and coefficients of determination of the linear fits of the decorrelation length as a function of the window width for the network transitivity of wRNA and corresponding significance levels for the tree ring width data set from eastern Canada and the AR(1) null model in the time and the window width domain.

domain	m	n	R^2	s_{aw}	s_{pw}	s_{tot}
time	0.2616	15.32	0.9947			
W	0.2270	0.3893	0.9913	0.99	0.95	0.94

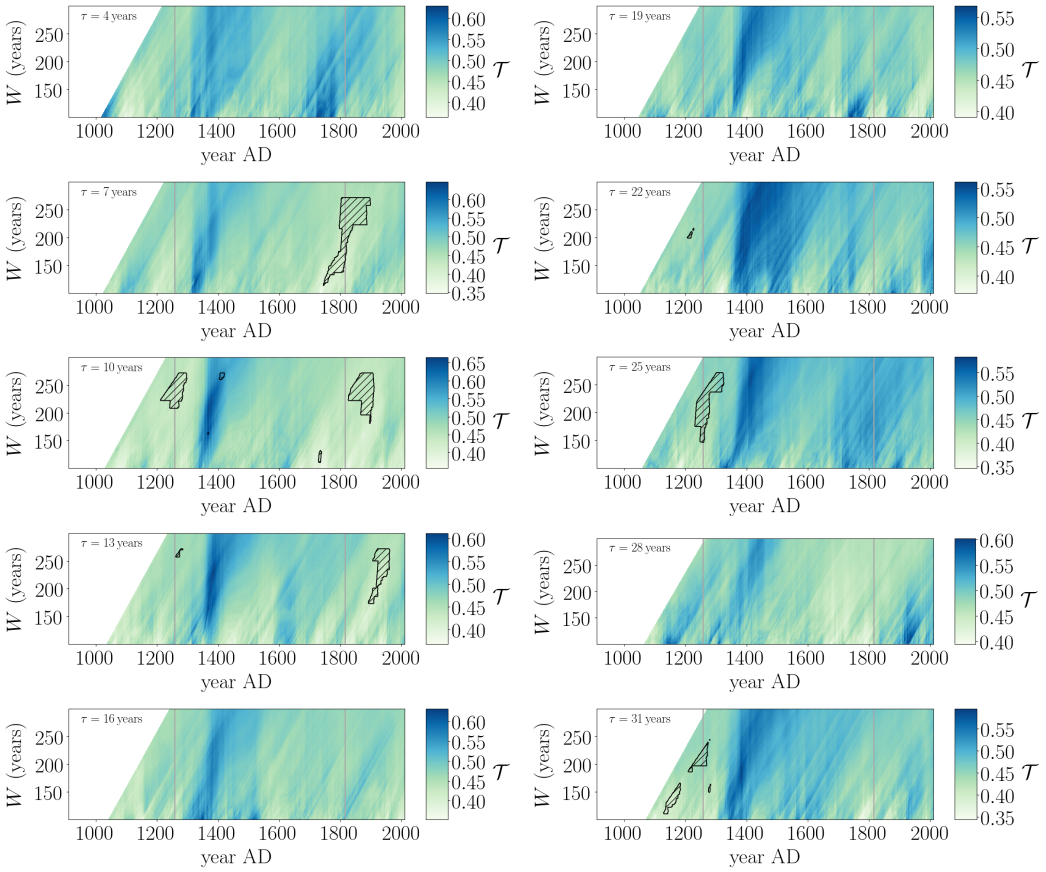

Figure C.1.: Network transitivity (colour coded) as a function of time for the tree ring width index time series from eastern Canada for varying delay times τ. Areawise significant analysis results are marked by the hatched contours. The vertical lines denote the Samalas and Tambora eruption, respectively. Reproduced with permission from P2.

C.3. Results for last millennium reanalysis data

To compare the results obtained for the different proxy data sets to possible real past climate conditions at the corresponding locations, we here analyse data from the LMR project version 2 (Hakim et al., 2016; Tardif et al., 2019). In this project, information from palaeoclimate data and general circulation models is combined to reconstruct globally gridded temperature and precipitation anomalies of the years $501 - 2000$ AD. We use ensemble averages of the coordinates closest to those of the sites of the palaeoclimate proxy data studied in chapter 6. That is, we use the coordinates (54° N, 70° W), (2° S, 80° W), (18° N, 100° W), and (14° S, 70° W) for comparison with the tree ring, lake sediment, speleothem, and ice core site, respectively.

The wRNA is performed analogously to the analysis in chapter 6. The embedding dimension is always chosen to be $m = 3$ and the delay times are given as $\tau = [50, 22, 64, 22]$ years for the temperature at the different sites and as $\tau = [38, 49, 23, 22]$ years for the precipitation at the different sites. The window width is varied in the interval $W \in [100, 300]$ years with step size $\Delta W = 1$ year and offset $dW = 1$ year.

The results are displayed in figures C.2 and C.3. Generally, we observe very few areawise significant patches of anomalously high or low values of the network transitivity in the LMR data. Also, we find that the transitivity varies similarly for temperature and precipitation but shows differences in variability for the different locations. For the climate conditions at the tree ring site, we find an areawise patch of low transitivity values coinciding with the onset of the Medieval Climate Anomaly (MCA) in the temperature and a small patch of areawise significant values at the end of the Little Ice Age in the precipitation data. The tree ring width data (compare chapter 6) show an areawise patch of low transitivity values at the end of the MCA. Due to the temporal limitation of the data set, no information about the onset of the MCA is available. For the data at the lake sediment site, we find a small patch of areawise significant low values of the network transitivity before the onset of the MCA in the precipitation data, while for the corresponding proxy data (compare chapter 6), we find several patches of areawise significant anomalies. For the speleothem and ice core sites, we do not find any areawise significant values in the LMR data.

These results again highlight local differences in past climate variability on the one hand and the necessity to further study the relation between analysis results obtained from palaeoclimate proxy data and real climate conditions on the other hand.

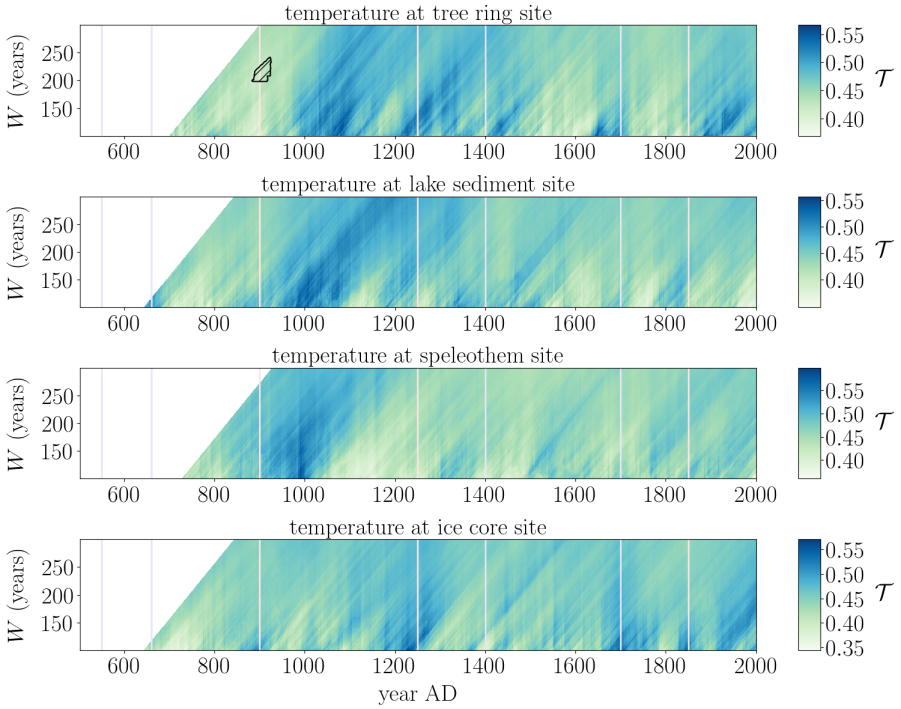

Figure C.2.: Network transitivity (colour coded) as a function of time for varying window width W for the temperature of the LMR data at the four different locations in combination with the areawise significance test (hatched contours). The vertical lines again denote the episodes of outstanding climate variability introduced in section 6.1.

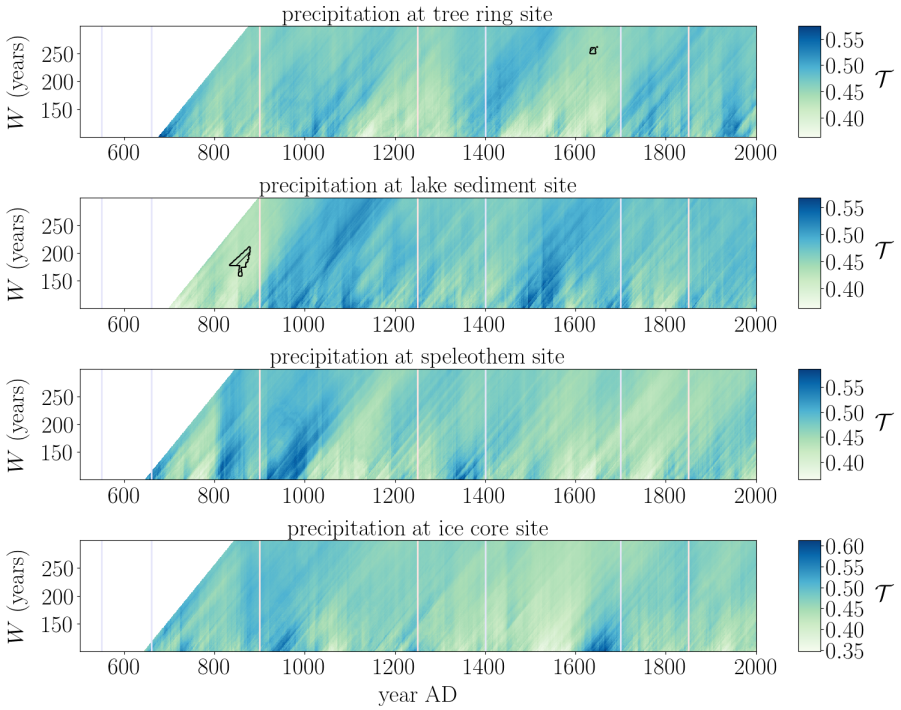

Figure C.3.: Same as in figure C.2 but for the precipitation data at the different locations.

Appendix D.

Additional information: Proxy system model perspective on wRNA

In section D.1, we present the details of the proxy system models that are used and referenced in chapter 7 for studying the suitability of windowed recurrence network analysis (wRNA) for detecting dynamical anomalies in time series from different palaeoclimate proxy archives. In section D.2, we provide some additional information and figures for the time series properties of the different input and model output time series. Finally, in section D.3, we present the wRNA results of the speleothem model in- and output when choosing the model parameters corresponding to the boundary conditions of Dongge cave.

D.1. Details on the proxy system models

Proxy system models are forward models that simulate the formation of paleoclimate proxies and can be split into an environment sub-model modelling the environmental factor to which the proxy is sensitive, a sensor sub-model describing the reaction of the proxy to the environmental factor, an archive sub-model adding the effect of storing the reaction into the specific archive, and an observation sub-model simulating dating and measurement uncertainties (Evans et al., 2013).

D.1.1. Modelling the tree archive

We model the tree ring width as a function of time using the intermediate complexity model Vaganov-Shashkin-Lite (VS-Lite) (Tolwinski-Ward et al., 2011). This is a reduced version of the full Vaganov-Shashkin model (Vaganov et al., 2006) and requires monthly input data of temperature T and either precipitation P or soil moisture M. It relies on the principle of limiting factors (Fritts, 1976), that is, the model assumes tree growth to be dependent on the scarcest resource. It combines an environment model for calculating soil moisture from precipitation, a sensor model that captures the non-linear response of the trees to the climatic boundary conditions, and an archive model in which the climate sensitivity over the year is integrated to obtain yearly ring width anomalies. Thresholds for temperature and soil moisture below which growth is not possible and above which growth is optimal (T_1, M_1, T_2, M_2), the latitude of the site Φ, and integration start and end months I_0 and I_f that set the

period over which climate is responsible for the growth of the modelled tree comprise the set of model parameters.

If precipitation is given, the Leaky Bucket model (Huang et al., 1996) is used as environment model to calculate the soil moisture based on the water balance in soil and additional model parameters as specified below are required. The components of the water balance in the Leaky Bucket model are soil moisture $M(t)$, precipitation $P(t)$, evaporation $E(t)$, run-off $R(t)$, and groundwater loss $G(t)$. The model equation reads

$$\frac{dM(t)}{dt} = P(t) - E(t) - R(t) - G(t). \tag{D.1}$$

The precipitation $P(t)$ is given by the monthly input data. The evaporation $E(t)$ is given by the relation

$$E(t) = E_p \frac{M(t)}{M_{\max}} \tag{D.2}$$

with $M_{\max}$ a measure of the capacity of soils to hold water and E_p the temperature-dependent potential evaporation rate

$$E_p = \begin{cases} 0 & T < 0°C \\ 16L\left(\frac{10T}{I}\right)^a & 0°C \leq T \leq 26.5°C \\ -415.58 + 32.25T - 0.43T^2 & T > 26.5°C. \end{cases} \tag{D.3}$$

L is given as

$$L = \frac{d}{30}\frac{h}{12} \tag{D.4}$$

with d the number of days in a month and h the hours of daylight at the middle day of the month which can be calculated as

$$h = \frac{24 \arccos(1 - m^*)}{180}. \tag{D.5}$$

In this case, m^* is given by

$$m^* = 1 - tan(\Phi) tan\left(23.439 \cos\left(d_m \frac{\pi}{182.625}\right)\right) \tag{D.6}$$

and d_m is the number of the day in the year of the middle of each month. I is given as

$$I = \sum_{M=1}^{12} \left(\frac{T_M}{5}\right)^{1.514} \tag{D.7}$$

where the sum is over the twelve months of the year. Finally, a is given as

$$a = 6.75 \cdot 10^{-7} I^3 - 7.71 \cdot 10^{-5} I^2 + 1.79 \cdot 10^{-2} I + 0.49. \tag{D.8}$$

The run-off $R(t)$ can be divided into the surface run-off $S(t)$ and the base flow run-off $B(t)$

$$R(t) = S(t) + B(t). \tag{D.9}$$

The surface run-off is given by

$$S(t) = P(t) \left(\frac{M(t)}{M_{\max}} \right)^m \tag{D.10}$$

where $m > 1$. The base flow run-off is given by

$$B(t) = \frac{\alpha}{\mu + 1} M(t) d_r \tag{D.11}$$

where α is the inverse of the response time of the base flow, μ determines the portion of the subsurface flow that becomes the base flow and d_r characterises the root depth which is included to convert the model to a volumetric measure. The remaining portion of the subsurface flow is lost as groundwater flow $G(t)$

$$G(t) = \frac{\mu\alpha}{\mu + 1} M(t) d_r. \tag{D.12}$$

That is, in order to calculate the soil moisture from the precipitation, the parameters $M_{\max}$, m, α, μ and d_r have to be specified. Then, the soil moisture of a given month is calculated as the moisture of the previous month plus the change according to equation (D.1) divided by the root depth

$$M(t) = M(t-1) + \frac{1}{d_r} \frac{dM}{dt}. \tag{D.13}$$

Thus, a starting soil moisture M_0 has to be specified. Also, a minimum soil moisture $M_{\min}$ is specified and values below this threshold are automatically set to the minimum soil moisture.

The temperature T and the soil moisture M are then used in the sensor model of VS-Lite to calculate a temperature-based and a moisture-based growth response as

$$g_T(t) = \begin{cases} 0 & \text{if } T(t) < T_1 \\ \dfrac{T(t) - T_1}{T_2 - T_1} & \text{if } T_1 \leq T(t) \leq T_2 \\ 1 & \text{if } T_2 > T(t) \end{cases} \tag{D.14}$$

and

$$g_M(t) = \begin{cases} 0 & \text{if } M(t) < M_1 \\ \dfrac{M(t) - M_1}{M_2 - M_1} & \text{if } M_1 \leq M(t) \leq M_2 \\ 1 & \text{if } M_2 > M(t), \end{cases} \tag{D.15}$$

respectively. T_1 and M_1 specify the threshold temperature and moisture below which no growth is possible and T_2 and M_2 are lower bounds on the optimal temperature and moisture for growth. In between, the growth responses are assumed to vary linearly with temperature and soil moisture. Then, a third insolation-based growth response $g_E(t)$ is calculated as the mean of the normalised length of day ndl of all days of a month. The normalised length of day of each day of the year is given as

$$\text{ndl} = \frac{\arccos(y)\sin(\Phi)\sin(\text{sd}) + \cos(\Phi)\cos(\text{sd})\sin(\arccos(y))}{\max\left\{\arccos(y)\sin(\Phi)\sin(\text{sd}) + \cos(\Phi)\cos(\text{sd})\sin(\arccos(y))\right\}} \tag{D.16}$$

with y given as

$$y = -\tan(\Phi)\tan(\text{sd}) \tag{D.17}$$

and sd the daily solar declination

$$\text{sd} = \arcsin\left(\sin\left(\frac{23.5\pi}{180}\right)\sin\left(\pi\frac{d-80}{180}\right)\right). \tag{D.18}$$

Here, d denotes the number of the day in the year.

The total growth response of the tree $g(t)$ is then, according to the principle of limiting factors (Fritts, 1976), given as the minimum of the temperature- and moisture-based growth responses modulated by the insolation-based growth response

$$g(t) = g_E(t)\min\left\{g_T(t), g_M(t)\right\}. \tag{D.19}$$

To get from those monthly data the annual growth response, $g(t)$ is integrated in the archive model of VS-Lite over those months that are specified as the start end end integration months I_0 and I_f. Finally, the annually resolved time series of tree ring width anomalies is obtained by normalising the annual growth response to zero mean and unit variance.

D.1.2. Modelling the lake archive

We use the PRoxY System Modelling (PRYSM) v2.0 framework (Dee et al., 2018) to model signatures of branched glycerol dialkyl glycerol tetraethers (brGDGTs) from lacustrine archives. As input, a time series of mean annual air temperature T is required. The sensor model uses this input to create a time series of temperature-dependent proxy signatures. The archive model then accounts for the bioturbation of

the signatures within the lake. For this, the abundance of the signal carrier over time (abu), the mixed layer thickness over time (mxl), and the number of signal carriers on which the proxy signal is measured (numb) have to be specified.

Branched glycerol dialkyl glycerol tetraethers are produced by bacteria. Their degree of cyclisation and methylation has been related to soil temperatures (Weijers et al., 2007) and also to mean annual air temperatures (De Jonge et al., 2014; Russell et al., 2018). The degree of methylation can be quantified by the Methylation of Branched Tetraether (MBT) index. The sensor model uses the $\mathrm{MBT}'_{5\mathrm{ME}}$ index that only uses 5-methyl isomers with the calibration of Russell et al. (2018), in which the mean annual air temperature is related to the $\mathrm{MBT}'_{5\mathrm{ME}}$ index via the equation

$$\mathrm{MBT}'_{5\mathrm{ME}} = (T + 1.21)/32.42. \tag{D.20}$$

The archive model then accounts for bioturbation and mixing of the sediments using the TURBO2 model (Trauth, 2013). Based on the assumption that mixing only takes place in a layer of thickness mxl on top of the core, TURBO2 models instantaneous mixing of individual sediment particles. For this, the model takes the proxy signature, i. e., the output of the sensor model and the corresponding abundances as input. A second, virtual species is created that has the same signatures as the original species and abundances that vary complementary to the first species. This is required in order to keep the total abundance of all species constant. In the next step, a virtual sedimentary core is created in form of a matrix with mxl initial rows and abu+50 columns. In this matrix, the information on the proxy signatures is stored and an additional matrix with species identifiers is created. Then, the sedimentary core is build up by adding rows of proxy signatures and species identifiers according to the model input. In every step of adding a row, two mixing processes take place: First, a horizontal mixing is implemented by randomly shuffling the columns of species identifiers in a row. Second, a vertical mixing is implemented by randomly permuting the upper mxl rows of both the isotopic signatures and species identifiers. After having obtained the full sedimentary core, the number of each species is counted in every row to obtain the corresponding bioturbated abundances. The bioturbated proxy signatures are obtained by averaging the first numb signatures of each species in each row. The bioturbated proxy signatures of the first species are then used as final proxy for the mean annual air temperature.

D.1.3. Modelling the speleothem archive

To model stable isotope variability in speleothems, we use the intermediate-complexity model that is included in the PRYSM framework (Dee et al., 2015) and based on the model presented in Partin et al. (2013). It requires the mean annual temperature T and the mean of the precipitation-weighted oxygen isotope composition of the precipitation $\delta^{18}\mathrm{O}_P$ as input. The model consists of a sensor model that covers processes in the karst, while processes in the soil such as evapotranspiration are

neglected. As model parameter, the ground water residence time τ_{gw} has to be specified.

The sensor model filters the $\delta^{18}\mathrm{O}_P$ signal by applying an aquifer recharge model to simulate the storage and thus the mixing of water of different ages in the karst (Gelhar and Wilson, 1974). This process is parametrised by the mean transit time $\tau_{\mathrm{gw}} = \Phi/a$ with Φ the porosity of the aquifer and a an outflow constant. It is sufficient to directly specify the mean transit time τ_{gw}. The isotopic composition of the cave water $\delta^{18}\mathrm{O}_d$ is then given as the convolution (denoted by $*$) of $\delta^{18}\mathrm{O}_w$ with the impulse response of the aquifer recharge model $g(t)$ for times $t > 0$

$$\delta^{18}\mathrm{O}_d = g(t) * \delta^{18}\mathrm{O}_P. \tag{D.21}$$

The impulse response is defined to be

$$g(t) = \frac{1}{\tau_{\mathrm{gw}}} \exp(-t\tau_{\mathrm{gw}}). \tag{D.22}$$

Finally, to obtain the isotopic composition of the flowstone calcite $\delta^{18}\mathrm{O}_c$, the model implements a temperature-dependent fractionation (Wackerbarth et al., 2010)

$$\delta^{18}\mathrm{O}_c = \frac{\delta^{18}O_d + 1000}{1.03086} \exp\left(\frac{2780}{T_a^2} - \frac{2.89}{1000}\right) - 1000 \tag{D.23}$$

with the temperature T_a being the decadal average of T that is calculated by applying a Butterworth filter (Zumbahlen, 2008).

D.1.4. Modelling the ice core archive

We model the isotopic composition of the ice in ice cores by using the ice core model presented within the PRYSM framework (Dee et al., 2015). As input, the precipitation-weighted mean annual oxygen isotope composition of the precipitation $\delta^{18}\mathrm{O}_P$ is required as a function of time t, which is internally converted to a function of age. The model is composed of a sensor model that takes into account an altitude effect and an archive model that corrects for compaction and diffusion within the ice core as detailed below. Model parameters are the mean air temperature T_m over the modelling time span at the site, the altitude of the glacier z, the mean surface pressure p, the mean accumulation rate at the site A_m, and the total depth of the core h_{max}, which is given by the time span of the observations times the average accumulation rate.

The sensor model corrects the isotopic composition of the precipitation for the altitude of the sampling location using the relation

$$\delta^{18}\mathrm{O}_{\mathrm{ice}} = \delta^{18}\mathrm{O}_P + \frac{z}{100}a, \tag{D.24}$$

with a being the altitude effect (Dee et al., 2015).

The archive model then accounts for compaction and diffusion within the ice core. In a first step, the densification of the firn with time is modelled. That is, the density ρ is calculated as a function of the depth of the core h, the mean temperature T_m, the mean accumulation rate A_m, and the surface density of the snow ρ_0 of the site under study. For this, an adapted version of the firn densification model by Herron and Langway is used (Herron and Langway, 1980). There are three stages of densification which have to be treated differently. The first stage takes place for densities $\rho_0 \leq \rho \leq \rho_c$ with ρ_c a critical density. In this stage, the densification rate is usually the highest of the three stages and the dominant mechanism is considered to be grain setting and packing. The second stage takes place for densities $\rho_c \leq \rho \leq \rho_a$ with ρ_a being the density at which air passages become closed off and form individual bubbles. In this stage, the densities increase more slowly and the underlying mechanisms are poorly understood. In the third stage ($\rho_a \leq \rho \leq \rho_i$ with ρ_i the density of solid ice), further densification takes place by a compression of the air bubbles. The densification model only accounts for the first two stages of densification, i. e., we assume that densification is negligible from the density ρ_a onwards.

For practical purposes, we have to specify the depth of the core and the step size dh at which the densities and ages are evaluated. Additionally, the density of ice ($\rho_i = 920\,\mathrm{kg/m^3}$), the critical density ($\rho_c = 550\,\mathrm{kg/m^3}$), and the density of water ($\rho_w = 1000\,\mathrm{kg/m^3}$) have to be specified, the latter for scaling reasons. Then, the critical depth h_c at which the density of the firn equals ρ_c can be calculated using the relation

$$h_c = \frac{1}{\rho_i k_0}\left[\ln\left(\frac{\rho_c}{\rho_i - \rho_c}\right) - \ln\left(\frac{\rho_0}{\rho_i - \rho_0}\right)\right], \tag{D.25}$$

with k_0 a temperature-dependent constant given as

$$k_0 = \frac{0.85 \cdot 11}{\rho_w}\exp\left(-\frac{10160}{RT_m}\right) \tag{D.26}$$

where R is the gas constant. The densities corresponding to the different depths h can then be calculated as

$$\rho(h) = \frac{\rho_i Z_0(h)}{1 + Z_0(h)} \tag{D.27}$$

with

$$Z_0(h) = \exp\left(\rho_i k_0 h + \ln\left(\frac{\rho_0}{\rho_i - \rho_0}\right)\right) \tag{D.28}$$

for depths smaller than the critical depth. Accordingly, the densities for depths larger than the critical depth can be calculated as

$$\rho(h) = \frac{\rho_i Z_1(h)}{1 + Z_1(h)}, \tag{D.29}$$

with

$$Z_1(h) = \exp\left(\rho_i k_1 (h - h_c) + \ln\left(\frac{\rho_c}{\rho_i - \rho_c}\right)\right) \tag{D.30}$$

and

$$k_1 = \frac{1.15 \cdot 575}{A_m^{0.5} \rho_w^{0.5}} \exp\left(-\frac{21400}{R T_m}\right). \tag{D.31}$$

From the density, the corresponding ages can be obtained as

$$t_j = \sum_{k=1}^{j} \frac{dh}{A_m} \frac{\rho_k}{\rho_i}. \tag{D.32}$$

Now that the depth h and the corresponding values of the density ρ and age t of the firn have been calculated in the sensor model, the archive model addresses diffusion within the core. In the PRYSM implementation, the archive model is based on the models presented by Cuffey and Steig (1998), Johnsen et al. (2000), and Gkinis et al. (2014). First, the diffusion length σ has to be calculated as a function of the density

$$\sigma^2(\rho) = \frac{1}{\rho^2} \int_{\rho_0}^{\rho} 2\rho^2 \left(\frac{d\rho}{dt}\right)^{-1} D(\rho) d\rho \tag{D.33}$$

with $D(\rho)$ being the diffusivity. The densification rate $d\rho/dt$ can be expressed as the density profile times the layer thickness

$$\frac{d\rho}{dt} = \frac{d\rho}{dt}\frac{dt}{dz}\frac{dz}{dt} = \frac{d\rho}{dz}\lambda \tag{D.34}$$

with $\lambda = dz/dt$ being the annual layer thickness. That is, we have

$$\sigma^2(\rho) = \frac{1}{\rho^2} \int_{\rho_0}^{\rho} 2\rho^2 \left(\frac{d\rho}{dz}\lambda\right)^{-1} D(\rho) d\rho. \tag{D.35}$$

In order to evaluate this, the diffusivity has to be expressed as a function of the density (Johnsen et al., 2000)

$$D(\rho) = \frac{m e_s D_{ai}}{R T_m \alpha_i \tau} \left(\frac{1}{\rho} - \frac{1}{\rho_i}\right) \tag{D.36}$$

where m is the molar weight of ice, e_s is the saturation vapour pressure over ice

$$e_s = \exp\left(9.5504 - \frac{5723.265}{T_m} + 3.530 \ln(T_m) - 0.0073 T_m\right), \tag{D.37}$$

and $D_{ai} = D_a/1.0285$ is the diffusivity of the water isotopologue $H_2^{18}O$. D_a is the diffusivity of water vapour in the air (Hall and Pruppacher, 1976)

$$D_a = 2.1 \cdot 10^{-5} \left(\frac{T_m}{T_0}\right)^{1.94} \left(\frac{p_0}{p}\right) \tag{D.38}$$

with $T_0 = 273.15\,\mathrm{K}$ and $p_0 = 1\,\mathrm{Atm}$. α_i is the ice-vapour fractionation for the water isotopologue $H_2^{18}O$ and τ is a property of porous materials characterising the length of actual flow paths within the material, i. e., the tortuosity, that can be determined by the relation (Johnsen et al., 2000)

$$\frac{1}{\tau} = 1 - A_m \left(\frac{\rho}{\rho_i}\right)^2 \tag{D.39}$$

for $\rho \leq \rho_i/\sqrt{A_m}$.

With this, we can calculate the final $\delta^{18}\mathrm{O}_d$ of the ice taking into account the diffusion by convolving the signal with a Gaussian kernel with standard deviation equalling the diffusion length

$$\delta^{18}\mathrm{O}_d = \frac{1}{\sigma\sqrt{2\pi}} \exp\left(\frac{-h^2}{2\sigma^2}\right) * \delta^{18}\mathrm{O}_{\mathrm{ice}} \tag{D.40}$$

where the convolution is again denoted by the asterisk ($*$). It is important to notice that the $\delta^{18}\mathrm{O}_{\mathrm{ice}}$ from equation (D.24) is given as a function of age from the climate input data, while here, it has to be given as a function of the depth h. To achieve this, the $\delta^{18}\mathrm{O}_{\mathrm{ice}}$ data are interpolated to the ages obtained from the densification model which correspond to the depths h. Then the calculations are performed for the interpolated data as a function of depth such that the resulting $\delta^{18}\mathrm{O}_d$ data are also given as a function of depth. The final results are interpolated back to the original, uniformly sampled input ages and then transformed to be functions of time.

D.2. Time series properties

D.2.1. Time series plots

Figures D.1 to D.3 show the different input and corresponding model output time series for the two stochastic processes (Gaussian white noise (GWN) and the autoregressive process of order 1 (AR(1) process), figure D.1), the two non-stationary time series of the Rössler and the Lorenz system (figure D.2), and the last millennium reanalysis data (figure D.3).

D.2.2. Evaluating the skewness of the distributions

To test whether the skewness values of the model output time series differ significantly from those of the model input, we created $N_{sk} = 10,000$ surrogate data sets for each

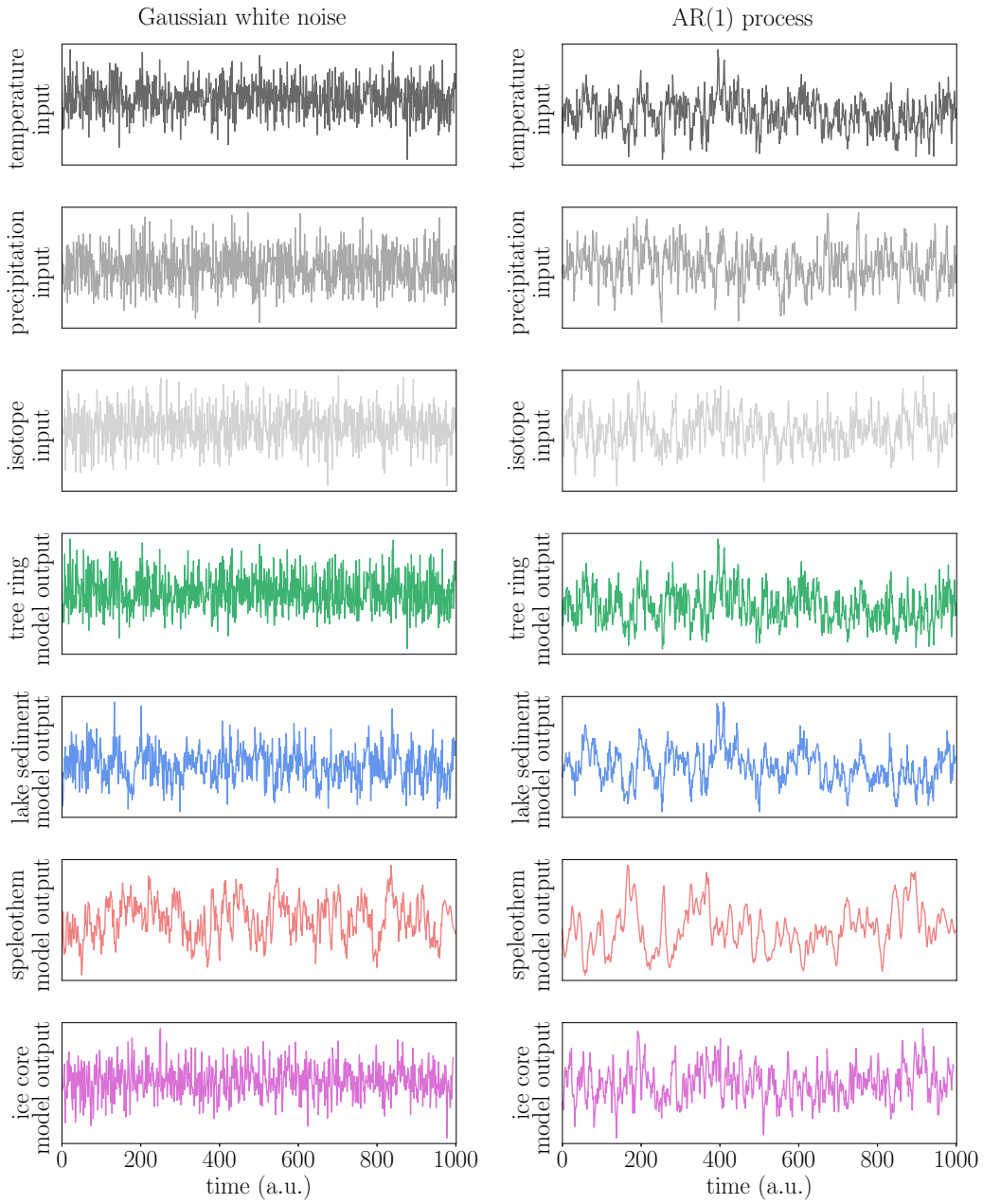

Figure D.1.: Annually resolved input time series for temperature, precipitation and isotopic composition and corresponding model system output time series (top to bottom) for the two stochastic processes (left: GWN, right: AR(1)). Adapted from P3.

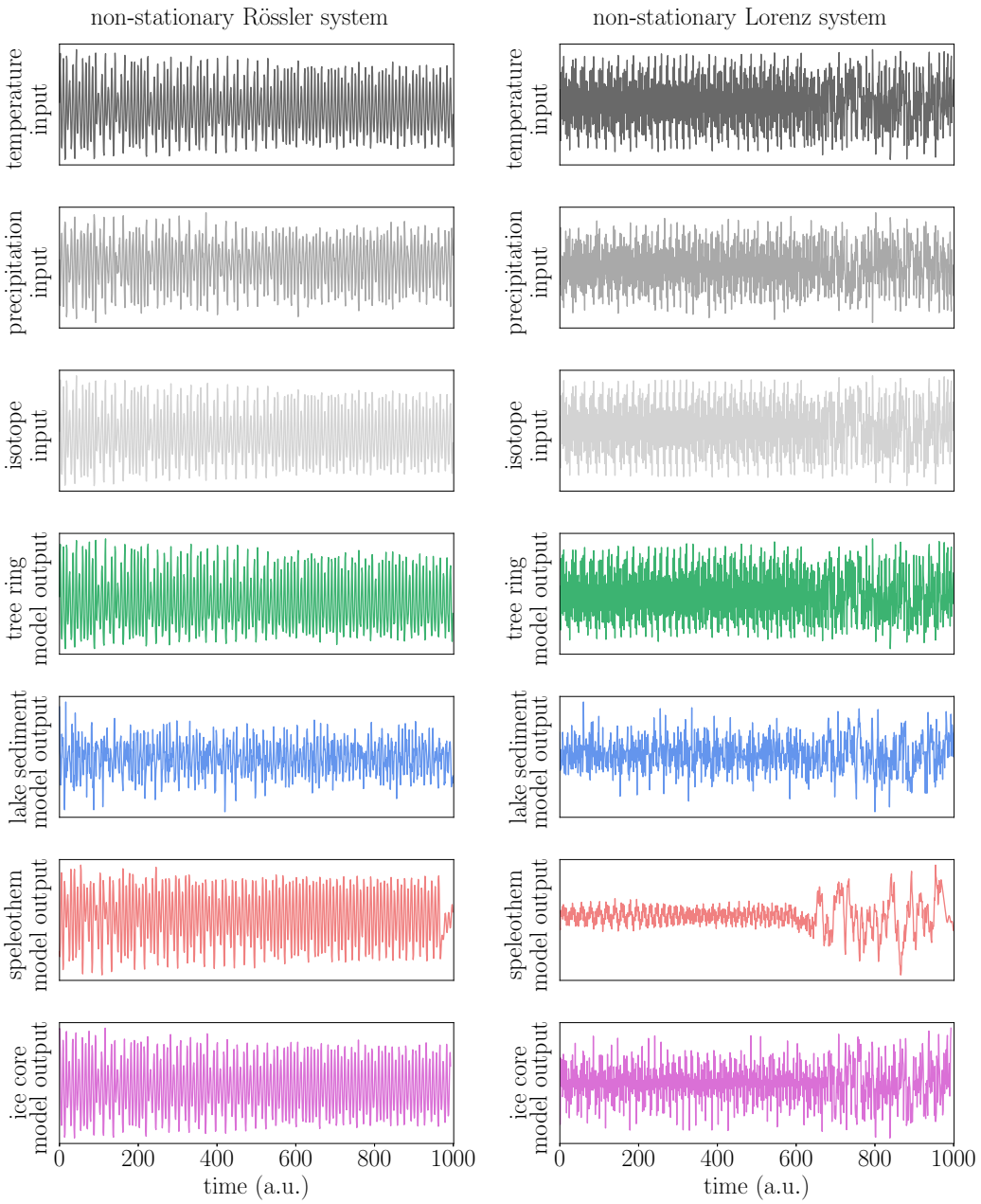

Figure D.2.: Same as in figure D.1 but for the input of the two non-stationary systems (left: Rössler, right: Lorenz). Adapted from P3.

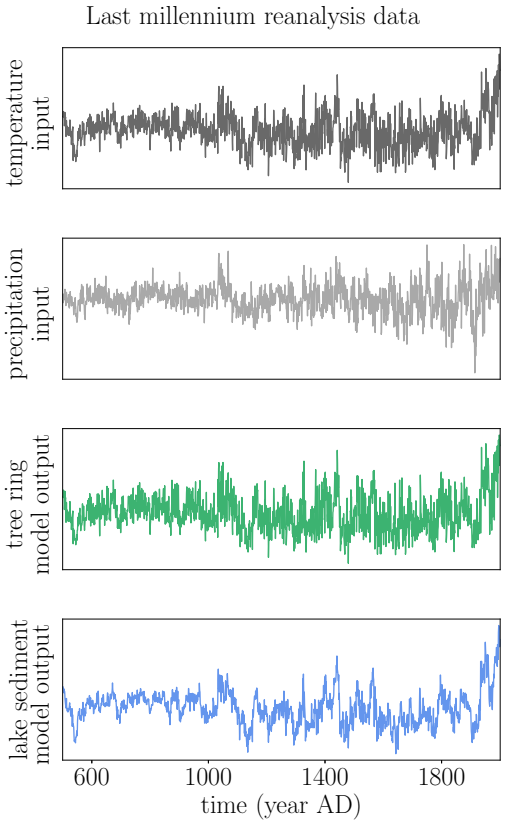

Figure D.3.: Same as in figure D.1 but for the input of the last millennium reanalysis data (Hakim et al., 2016; Tardif et al., 2019). Adapted from P3.

input scenario. For GWN and the AR(1) process this was done according to the descriptions in section 7.3, while for the other cases, we added different realisations of white noise to the corresponding time series. Then, for each surrogate realisation, we calculated the skewness of the distribution and took the 0.5th and 99.5th percentile as confidence bounds. The resulting 99% confidence intervals are $[-0.20, 0.20]$ for GWN, $[-0.29, 0.29]$ for the AR(1) process, $[0.20, 0.23]$ for the non-stationary Rössler system, $[-0.03, 0.00]$ for the non-stationary Lorenz system, $[0.32, 0.34]$ for the last millennium reanalysis temperature, and $[0.00, 0.02]$ for the last millennium reanalysis precipitation. As precipitation was created such that it is proportional to the negative temperature, the corresponding confidence interval is $[-0.23, -0.20]$ for the Rössler system and $[0.00, 0.03]$ for the Lorenz system.

D.3. Speleothem model for Dongge cave

To better understand the discrepancy between the results for Juxtlahuaca cave from chapter 6 where no robust results could be obtained from the data and the many successful characterisations of past climate variability in Asia using recurrence based approaches (e. g. Donges et al., 2015a; Eroglu et al., 2016), we additionally apply the speleothem model with parameters set corresponding to those of Dongge cave which constitutes one of the most studied speleothem data sets (Wang et al., 2005).

Dongge cave is located in southern China (25.3° N, 108.1° E) at an elevation of 680 m. Records of stalagmite DA could be related to the history of the Asian monsoon of the last 9000 years. The proxy values have an average of $-8.00\,‰$ where smaller values mean a stronger monsoon and vice versa. The average temperature in the cave is given as 15.6°C. The mean of the precipitation-weighted isotopic composition of the input is again chosen such that the average of the model output data equals the average of the Dongge cave proxy data. The mean aquifer transit time τ_{gw} highly depends on the local boundary conditions but is usually in the order of a few years (Dee et al., 2015). We here choose to use a mean aquifer transit time of five years. An overview of the climatic boundary conditions and model parameters is given in table D.1.

Table D.1.: Climatic boundary conditions and model parameters for the speleothem $\delta^{18}\mathrm{O}$ model as derived from the Dongge cave data (Wang et al., 2005).

variable	description	value
T_m	mean temperature at site	15.6° C
$\delta^{18}\mathrm{O}_P$	mean isotopic composition of precipitation	$-8.05\,‰$
τ_{gw}	mean aquifer transit time	5 years

Table D.2.: Confidence levels of the areawise significance test for the different input and speleothem model output time series for the Dongge cave setting.

GWN	AR(1)	ROS	LOR
0.978	0.727	0.958	0.992

Table D.3.: Fractions of missed and falsely identified significant points in the speleothem model for the Dongge cave setting with respect to the isotope input.

	GWN	AR(1)	ROS	LOR
missed	0.010	0.000	0.011	0.106
falsely identified	0.001	0.105	0.001	0.289

We perform the same analysis as for the speleothem model with the Juxtlahuaca cave setting, that is, we run the different input time series through the model, analyse the resulting model output time series with the developed analysis framework, and compare the results to the results of the isotope input time series. Table D.2 gives the confidence levels of the areawise significance test for wRNA. Except for the AR(1) process, we observe very high confidence levels.

Figure D.4 shows the results of the wRNA for the isotope input time series and the corresponding speleothem model output time series. In the output, we observe both missed areawise significant points and falsely detected areawise significant points. The areawise significant patches observed for the AR(1) process possibly relate to the low significance level of the test. For the Lorenz input, we observe a very large patch of areawise significant points that is not present within the input. Still, the variability of the network transitivity shows the expected behaviour of higher values before $b_L = 166.5$ and of lower values afterwards.

In analogy to the results from chapter 7, table D.3 displays the fractions of missed and falsely identified significant points confirming, that both types of errors occur for this choice of model parameters and that falsely identified significant points are more pronounced than in the other models. In particular, the fraction of missed significant points is equivalent for the Juxtlahuaca cave and the Dongge cave setting, while for the Dongge cave setting, we identify a smaller fraction of falsely identified significant points. Thus, especially the number of falsely identified significant point seems to respond to local boundary conditions such as the mean aquifer transit time. More systematic studies on the role that this parameter plays for tracking past climate variability in speleothem data with wRNA might reveal which data sets from which caves are particularly suited for studying past climate variability.

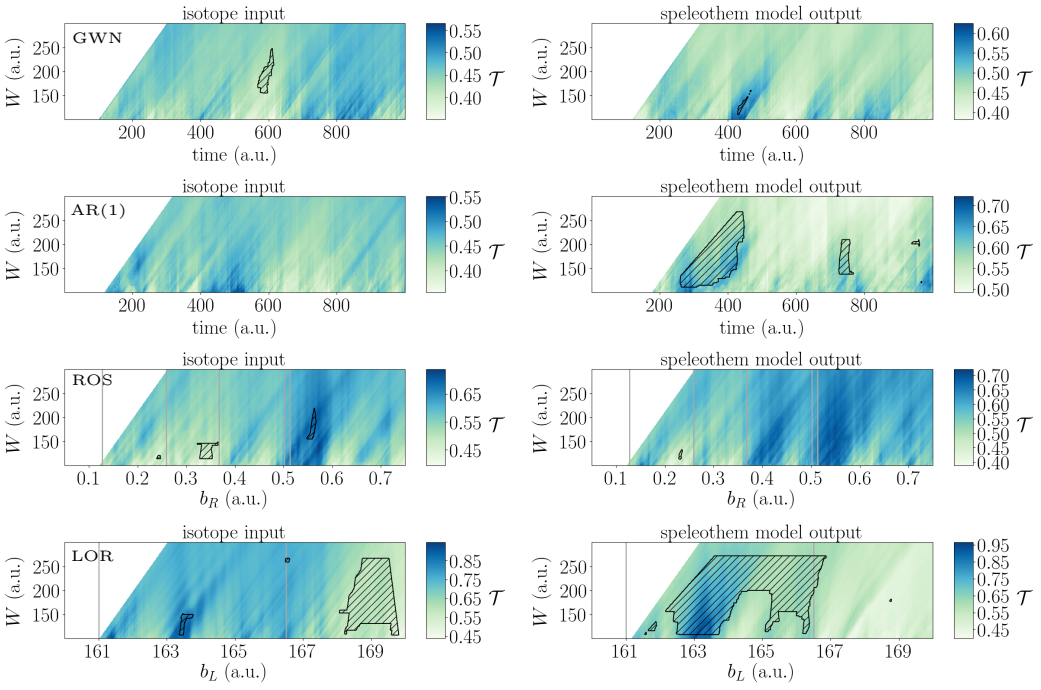

Figure D.4.: Network transitivity (colour-coded) of isotope input and speleothem model output for the Dongge cave setting with areawise significance test (hatched contours) for GWN, the AR(1) process, and the non-stationary Rössler and Lorenz system (top to bottom). The vertical lines denote the transitions described in chapter 7. Adapted from P3.

Code and data availability

Exemplary code for performing windowed recurrence network analysis, windowed scale-specific recurrence network analysis, and the areawise significance test is available at https://gitlab.pik-potsdam.de/lekscha/awsig. The code for the data analysis and modelling presented in this thesis is also available from the author upon request. Please do not hesitate to contact me.

All data used for the analysis is available online and was downloaded from https://atmos.washington.edu/~hakim/lmr/LMRv2/index.html (last millennium reanalysis data), https://www.blogs.uni-mainz.de/fb09climatology/e-canada/ (tree ring width data from eastern Canada), https://www1.ncdc.noaa.gov/pub/data/paleo/paleolimnology/ecuador/pallcacocha_red_intensity.txt (lake sediment data from Laguna Pallcacocha), https://www1.ncdc.noaa.gov/pub/data/paleo/speleothem/northamerica/mexico/juxtlahuaca2012.txt (speleothem data from Juxtlahuaca cave), https://www1.ncdc.noaa.gov/pub/data/paleo/speleothem/china/dongge2005.txt (speleothem data from Dongge cave), and https://www1.ncdc.noaa.gov/pub/data/paleo/icecore/trop/quelccaya/quelccaya2013.txt (ice core data from Quelccaya ice cap).

Bibliography

Abarbanel, H. D. I. (1996a). *Analysis of Observed Chaotic Data*. Springer-Verlag New York. DOI: 10.1007/978-1-4612-0763-4.

Abarbanel, H. D. I. (1996b). Reconstruction of Phase Space. In: *Analysis of Observed Chaotic Data*. Springer New York, pp. 13–23. DOI: 10.1007/978-1-4612-0763-4_2.

Abarbanel, H. D. I., R. Brown, J. J. Sidorowich, and L. S. Tsimring (1993). The analysis of observed chaotic data in physical systems. *Reviews of Modern Physics*, 65 (4), 1331–1392. DOI: 10.1103/revmodphys.65.1331.

Aeyels, D. (1981). Generic Observability of Differentiable Systems. *SIAM Journal on Control and Optimization*, 19 (5), 595–603. DOI: 10.1137/0319037.

Aguirre, L. A. and C. Letellier (2005). Observability of multivariate differential embeddings. *Journal of Physics A: Mathematical and General*, 38 (28), 6311–6326. DOI: 10.1088/0305-4470/38/28/004.

Aguirre, L. A. and C. Letellier (2011). Investigating observability properties from data in nonlinear dynamics. *Phys. Rev. E*, 83, (6), 066209. DOI: 10.1103/PhysRevE.83.066209.

Aguirre, L. A., S. B. Bastos, M. A. Alves, and C. Letellier (2008). Observability of nonlinear dynamics: Normalized results and a time-series approach. *Chaos: An Interdisciplinary Journal of Nonlinear Science*, 18 (1), 013123. DOI: 10.1063/1.2885386.

Albert, R. and A.-L. Barabási (2002). Statistical mechanics of complex networks. *Rev. Mod. Phys.*, 74, (1), 47–97. DOI: 10.1103/RevModPhys.74.47.

Alpaydin, E. (2014). *Introduction to Machine Learning*. Third Edition. The MIT Press.

Atsawawaranunt, K., L. Comas-Bru, S. Amirnezhad Mozhdehi, M. Deininger, S. P. Harrison, A. Baker, M. Boyd, N. Kaushal, S. M. Ahmad, Y. Ait Brahim, M. Arienzo, P. Bajo, K. Braun, Y. Burstyn, S. Chawchai, W. Duan, I. G. Hatvani, J. Hu, Z. Kern, I. Labuhn, M. Lachniet, F. A. Lechleitner, A. Lorrey, C. Pérez-Mejías, R. Pickering, N. Scroxton, and S. W. G. Members (2018). The SISAL database: a global resource to document oxygen and carbon isotope records from speleothems. *Earth System Science Data*, 10 (3), 1687–1713. DOI: 10.5194/essd-10-1687-2018.

Barabási, A.-L. and R. Albert (1999). Emergence of Scaling in Random Networks. *Science*, 286, (5439), 509–512. DOI: 10.1126/science.286.5439.509.

Barrat, A. and M. Weigt (2000). On the properties of small-world network models. *Eur. Phys. J. B*, 13 (3), 547–560. DOI: 10.1007/s100510050067.

Barrio, R. and S. Serrano (2007). A three-parametric study of the Lorenz model. *Physica D: Nonlinear Phenomena*, 229 (1), 43 –51. DOI: 10.1016/j.physd.2007.03.013.

Bianchi, G. G. and I. N. McCave (1999). Holocene periodicity in North Atlantic climate and deep-ocean flow south of Iceland. *Nature*, 397, 515. DOI: 10.1038/17362.

Bird, B. W., M. B. Abbott, M. Vuille, D. T. Rodbell, N. D. Stansell, and M. F. Rosenmeier (2011). A 2,300-year-long annually resolved record of the South American summer monsoon from the Peruvian Andes. *Proceedings of the National Academy of Sciences*, 108 (21), 8583–8588. DOI: 10.1073/pnas.1003719108.

Boccaletti, S., V. Latora, Y. Moreno, M. Chavez, and D.-U. Hwang (2006). Complex networks: Structure and dynamics. *Physics Reports*, 424 (4), 175 –308. DOI: 10.1016/j.physrep.2005.10.009.

Bradley, E. and H. Kantz (2015). Nonlinear time-series analysis revisited. *Chaos: An Interdisciplinary Journal of Nonlinear Science*, 25 (9), 097610. DOI: 10.1063/1.4917289.

Bradley, R. S. (2015a). Chapter 1 - Paleoclimatic Reconstruction. In: *Paleoclimatology (Third Edition)*. Ed. by R. S. Bradley. Third Edition. Academic Press, pp. 1 –11. DOI: 10.1016/B978-0-12-386913-5.00001-6.

Bradley, R. S. (2015b). Chapter 13 - Tree Rings. In: *Paleoclimatology (Third Edition)*. Ed. by R. S. Bradley. Third Edition. Academic Press, pp. 453 –497. DOI: 10.1016/B978-0-12-386913-5.00013-2.

Bradley, R. S. (2015c). Chapter 5 - Ice Cores. In: *Paleoclimatology (Third Edition)*. Ed. by R. S. Bradley. Third Edition. Academic Press, pp. 137 –194. DOI: 10.1016/B978-0-12-386913-5.00005-3.

Bradley, R. S. (2015d). Chapter 8 - Speleothems. In: *Paleoclimatology (Third Edition)*. Ed. by R. S. Bradley. Third Edition. Academic Press, pp. 291 –318. DOI: 10.1016/B978-0-12-386913-5.00008-9.

Bradley, R. S. (2015e). Chapter 9 - Lake Sediments. In: *Paleoclimatology (Third Edition)*. Ed. by R. S. Bradley. Third Edition. Academic Press, pp. 319 –343. DOI: 10.1016/B978-0-12-386913-5.00009-0.

Bradley, R. S. (2015f). *Paleoclimatology (Third Edition)*. Ed. by P. T. Edition). Third Edition. Academic Press. DOI: doi.org/10.1016/C2009-0-18310-1.

Briffa, K. R., P. D. Jones, F. H. Schweingruber, W. Karlén, and S. G. Shiyatov (1996). Tree-ring variables as proxy-climate indicators: Problems with low-frequency signals. In: *Climatic Variations and Forcing Mechanisms of the Last 2000 Years*. Ed. by P. D. Jones, R. S. Bradley, and J. Jouzel. Springer Berlin Heidelberg, pp. 9–41.

Briffa, K. R., P. D. Jones, F. H. Schweingruber, and T. J. Osborn (1998). Influence of volcanic eruptions on Northern Hemisphere summer temperature over the past 600 years. *Nature*, 393 (6684), 450–455. DOI: 10.1038/30943.

Briffa, K., T. Osborn, and F. Schweingruber (2004). Large-scale temperature inferences from tree rings: a review. *Global and Planetary Change*, 40 (1), 11 –26. DOI: 10.1016/S0921-8181(03)00095-X.

Broomhead, D. S. and G. P. King (1986). Extracting qualitative dynamics from experimental data. *Physica D: Nonlinear Phenomena*, 20 (2), 217 –236. DOI: 10.1016/0167-2789(86)90031-X.

Büntgen, U., V. S. Myglan, F. C. Ljungqvist, M. McCormick, N. Di Cosmo, M. Sigl, J. Jungclaus, S. Wagner, P. J. Krusic, J. Esper, J. O. Kaplan, M. A. C. de Vaan, J. Luterbacher, L. Wacker, W. Tegel, and A. V. Kirdyanov (2016). Cooling and societal change during the Late Antique Little Ice Age from 536 to around 660 AD. *Nature Geoscience*, 9, 231. DOI: 10.1038/ngeo2652.

Büntgen, U., W. Tegel, K. Nicolussi, M. McCormick, D. Frank, V. Trouet, J. O. Kaplan, F. Herzig, K.-U. Heussner, H. Wanner, J. Luterbacher, and J. Esper (2011). 2500 Years of European Climate Variability and Human Susceptibility. *Science*, 331 (6017), 578. DOI: 10.1126/science.1197175.

Buzug, T. and G. Pfister (1992). Comparison of algorithms calculating optimal embedding parameters for delay time coordinates. *Physica D: Nonlinear Phenomena*, 58 (1), 127 –137. DOI: 10.1016/0167-2789(92)90104-U.

Cao, L. (1997). Practical method for determining the minimum embedding dimension of a scalar time series. *Physica D: Nonlinear Phenomena*, 110 (1), 43 –50. DOI: 10.1016/S0167-2789(97)00118-8.

Carroll, T. L. (2018). Testing dynamical system variables for reconstruction. *Chaos: An Interdisciplinary Journal of Nonlinear Science*, 28 (10), 103117. DOI: 10.1063/1.5049903.

Casdagli, M., S. Eubank, J. D. Farmer, and J. Gibson (1991). State space reconstruction in the presence of noise. *Physica D*, 51 (1), 52 –98. DOI: 10.1016/0167-2789(91)90222-U.

Chen, Y. and H. Yang (2012). Multiscale recurrence analysis of long-term nonlinear and nonstationary time series. *Chaos, Solitons and Fractals*, 45, 978 –987. DOI: 10.1016/j.chaos.2012.03.013.

Cohen, A. (2003). *Paleolimnology: The History and Evolution of Lake Systems*. Oxford University Press.

Crowley, T. J. (2000). Causes of Climate Change Over the Past 1000 Years. *Science*, 289 (5477), 270–277. DOI: 10.1126/science.289.5477.270.

Cuffey, K. M. and E. J. Steig (1998). Isotopic diffusion in polar firn: implications for interpretation of seasonal climate parameters in ice-core records, with emphasis on central Greenland. *Journal of Glaciology*, 44 (147), 273–284. DOI: 10.3189/S0022143000002616.

De Jonge, C., E. C. Hopmans, C. I. Zell, J.-H. Kim, S. Schouten, and J. S. S. Damsté (2014). Occurrence and abundance of 6-methyl branched glycerol dialkyl glycerol tetraethers in soils: Implications for palaeoclimate reconstruction. *Geochimica et Cosmochimica Acta*, 141, 97 –112. DOI: 10.1016/j.gca.2014.06.013.

Dee, S., J. Emile-Geay, M. N. Evans, A. Allam, E. J. Steig, and D. Thompson (2015). PRYSM: An open-source framework for PRoxY System Modeling, with applications to oxygen-isotope systems. *Journal of Advances in Modeling Earth Systems*, 7 (3), 1220–1247. DOI: 10.1002/2015MS000447.

Dee, S. G., J. M. Russell, C. Morrill, Z. Chen, and A. Neary (2018). PRYSM v2.0: A Proxy System Model for Lacustrine Archives. *Paleoceanography and Paleoclimatology*, 33 (11), 1250–1269. DOI: 10.1029/2018PA003413.

Deng, L. (2014). Multi-scale recurrence analysis of complex temporal-spatial system. In: *Proceedings of the 33rd Chinese Control Conference*, pp. 7383–7387. DOI: 10.1109/ChiCC.2014.6896226.

Dijkstra, H. A. (2013). *Nonlinear Climate Dynamics*. New York: Cambridge University Press.

Donges, J. F., Y. Zou, N. Marwan, and J. Kurths (2009). Complex networks in climate dynamics. *The European Physical Journal Special Topics*, 174 (1), 157–179. DOI: 10.1140/epjst/e2009-01098-2.

Donges, J. F., R. V. Donner, K. Rehfeld, N. Marwan, M. H. Trauth, and J. Kurths (2011a). Identification of dynamical transitions in marine palaeoclimate records by recurrence network analysis. *Nonlinear Processes in Geophysics*, 18 (5), 545–562. DOI: 10.5194/npg-18-545-2011.

Donges, J. F., R. V. Donner, M. H. Trauth, N. Marwan, H.-J. Schellnhuber, and J. Kurths (2011b). Nonlinear detection of paleoclimate-variability transitions possibly related to human evolution. *Proceedings of the National Academy of Sciences*, 108 (51), 20422–20427. DOI: 10.1073/pnas.1117052108.

Donges, J. F., J. Heitzig, R. V. Donner, and J. Kurths (2012). Analytical framework for recurrence network analysis of time series. *Physical Review E*, 85 (4), 046105. DOI: 10.1103/physreve.85.046105.

Donges, J. F., R. V. Donner, N. Marwan, S. F. M. Breitenbach, K. Rehfeld, and J. Kurths (2015a). Non-linear regime shifts in Holocene Asian monsoon variability: potential impacts on cultural change and migratory patterns. *Climate of the Past*, 11 (5), 709–741. DOI: 10.5194/cp-11-709-2015.

Donges, J. F., J. Heitzig, B. Beronov, M. Wiedermann, J. Runge, Q. Y. Feng, L. Tupikina, V. Stolbova, R. V. Donner, and N. Marwan et al. (2015b). Unified functional network and nonlinear time series analysis for complex systems science: The pyunicorn package. *Chaos*, 25 (11), 113101. DOI: 10.1063/1.4934554.

Donner, R. V., Y. Zou, J. F. Donges, N. Marwan, and J. Kurths (2010a). Ambiguities in recurrence-based complex network representations of time series. *Physical Review E*, 81 (1), 015101. DOI: 10.1103/physreve.81.015101.

Donner, R. V, Y. Zou, J. F Donges, N. Marwan, and J. Kurths (2010b). Recurrence networks — a novel paradigm for nonlinear time series analysis. *New Journal of Physics*, 12 (3), 033025. DOI: 10.1088/1367-2630/12/3/033025.

Donner, R. V., M. Small, J. F. Donges, N. Marwan, Y. Zou, R. Xiang, and J. Kurths (2011a). Recurrence-based time series analysis by means of complex network methods. *International Journal of Bifurcation and Chaos*, 21 (04), 1019–1046. DOI: 10.1142/s0218127411029021.

Donner, R. V., J. Heitzig, J. F. Donges, Y. Zou, N. Marwan, and J. Kurths (2011b). The geometry of chaotic dynamics — a complex network perspective. *The European Physical Journal B*, 84 (4), 653–672. DOI: 10.1140/epjb/e2011-10899-1.

Donner, R. V., J. F. Donges, Y. Zou, and J. H. Feldhoff (2015). Complex Network Analysis of Recurrences. In: *Recurrence Quantification Analysis*. Ed. by C. Webber and N. Marwan. Springer International Publishing, pp. 101–163. DOI: 10.1007/978-3-319-07155-8_4.

Eckmann, J.-P. and D. Ruelle (1985). Ergodic theory of chaos and strange attractors. *Rev. Mod. Phys.*, 57, (3), 617–656. DOI: 10.1103/RevModPhys.57.617.

Eckmann, J.-P., S. Kamphorst, and D. Ruelle (1987). Recurrence plots of dynamical systems. *Europhysics Letters*, 5, 973–977.

Elsner, J. B. and A. A. Tsonis (1996). Foundations of SSA. In: *Singular Spectrum Analysis: A New Tool in Time Series Analysis*. Springer US, pp. 39–50. DOI: 10.1007/978-1-4757-2514-8_4.

Erdös, P. and A. Rényi (1959). On random graphs. I. *Publ. Math.*, (6), 290–297.

Eroglu, D., N. Marwan, S. Prasad, and J. Kurths (2014). Finding recurrence networks' threshold adaptively for a specific time series. *Nonlinear Processes in Geophysics*, 21 (6), 1085–1092. DOI: 10.5194/npg-21-1085-2014.

Eroglu, D., F. H. McRobie, I. Ozken, T. Stemler, K.-H. Wyrwoll, S. F. M. Breitenbach, N. Marwan, and J. Kurths (2016). See-saw relationship of the Holocene East Asian-Australian summer monsoon. *Nature Communications*, 7, 12929. DOI: 10.1038/ncomms12929.

Eroglu, D., N. Marwan, M. Stebich, and J. Kurths (2018). Multiplex recurrence networks. *Phys. Rev. E*, 97, (1), 012312. DOI: 10.1103/PhysRevE.97.012312.

Esper, J., P. J. Krusic, F. C. Ljungqvist, J. Luterbacher, M. Carrer, E. Cook, N. K. Davi, C. Hartl-Meier, A. Kirdyanov, O. Konter, V. Myglan, M. Timonen, K. Treydte, V. Trouet, R. Villalba, B. Yang, and U. Büntgen (2016). Ranking of tree-ring based temperature reconstructions of the past millennium. *Quaternary Science Reviews*, 145, 134 –151. DOI: 10.1016/j.quascirev.2016.05.009.

Evans, M., S. Tolwinski-Ward, D. Thompson, and K. Anchukaitis (2013). Applications of proxy system modeling in high resolution paleoclimatology. *Quaternary Science Reviews*, 76, 16 –28. DOI: 10.1016/j.quascirev.2013.05.024.

Farmer, J. D., E. Ott, and J. A. Yorke (1983). The dimension of chaotic attractors. *Physica D: Nonlinear Phenomena*, 7 (1), 153 –180. DOI: 10.1016/0167-2789(83)90125-2.

Feldhoff, J. H., R. V. Donner, J. F. Donges, N. Marwan, and J. Kurths (2012). Geometric detection of coupling directions by means of inter-system recurrence networks. *Physics Letters A*, 376 (46), 3504–3513. DOI: 10.1016/j.physleta.2012.10.008.

Feldhoff, J. H., R. V. Donner, J. F. Donges, N. Marwan, and J. Kurths (2013). Geometric signature of complex synchronisation scenarios. *Europhysics Letters*, 102 (3), 30007. DOI: 10.1209/0295-5075/102/30007.

Flach, M., H. Lange, T. Foken, and M. Hauhs (2016). Recurrence Analysis of Eddy Covariance Fluxes. In: *Recurrence Plots and Their Quantifications: Expanding Horizons*. Ed. by C. L. Webber Jr., C. Ioana, and N. Marwan. Cham: Springer International Publishing, pp. 301–319. DOI: 10.1007/978-3-319-29922-8_16.

Franke, J. G. and R. V. Donner (2017). Dynamical anomalies in terrestrial proxies of North Atlantic climate variability during the last 2 ka. *Climatic Change*, 143 (1), 87–100. DOI: 10.1007/s10584-017-1979-z.

Franke, J. G., J. P. Werner, and R. V. Donner (2017). Reconstructing Late Holocene North Atlantic atmospheric circulation changes using functional paleoclimate networks. *Climate of the Past*, 13 (11), 1593–1608. DOI: 10.5194/cp-13-1593-2017.

Fraser, A. M. and H. L. Swinney (1986). Independent coordinates for strange attractors from mutual information. *Physical Review A*, 33, (2), 1134–1140. DOI: 10.1103/PhysRevA.33.1134.

Fredkin, D. R. and J. A. Rice (1995). Method of false nearest neighbors: A cautionary note. *Phys. Rev. E*, 51, (4), 2950–2954. DOI: 10.1103/PhysRevE.51.2950.

Fritts, H. C. (1976). *Tree rings and climate*. Academic Press. DOI: 10.1016/B978-0-12-268450-0.X5001-0.

Gao, Z.-K., Y. Yang, P. Fang, Y. Zou, C. Xia, and M. Du (2015). Multiscale complex network for analyzing experimental multivariate time series. *Europhysics Letters*, 109, 30005. DOI: 10.1209/0295-5075/109/30005.

Gao, Z.-K., M. Small, and J. Kurths (2016). Complex network analysis of time series. *Europhysics Letters*, 116 (5), 50001. DOI: 10.1209/0295-5075/116/50001.

Garcia, S. P. and J. S. Almeida (2005a). Multivariate phase space reconstruction by nearest neighbor embedding with different time delays. *Phys. Rev. E*, 72, (2), 027205. DOI: 10.1103/PhysRevE.72.027205.

Garcia, S. P. and J. S. Almeida (2005b). Nearest neighbor embedding with different time delays. *Phys. Rev. E*, 71, (3), 037204. DOI: 10.1103/PhysRevE.71.037204.

Gelhar, L. W. and J. L. Wilson (1974). Ground-Water Quality Modeling. *Groundwater*, (12), 399–408. DOI: 10.1111/j.1745-6584.1974.tb03050.x.

Gennaretti, F., D. Arseneault, A. Nicault, L. Perreault, and Y. Bégin (2014). Volcano-induced regime shifts in millennial tree-ring chronologies from northeastern North America. *Proceedings of the National Academy of Sciences*, 111 (28), 10077–10082. DOI: 10.1073/pnas.1324220111.

Gessler, A., J. P. Ferrio, R. Hommel, K. Treydte, R. A. Werner, and R. K. Monson (2014). Stable isotopes in tree rings: towards a mechanistic understanding of isotope fractionation and mixing processes from the leaves to the wood. *Tree Physiology*, 34 (8), 796–818. DOI: 10.1093/treephys/tpu040.

Gibson, J. F., J. D. Farmer, M. Casdagli, and S. Eubank (1992). An Analytic Approach to Practical Phase Space Reconstruction. *Physica*, 57D (1).

Giuliani, A. and C. Manetti (1996). Hidden peculiarities in the potential energy time series of a tripeptide highlighted by a recurrence plot analysis: A molecular dynamics simulation. *Phys. Rev. E*, 53, (6), 6336–6340. DOI: 10.1103/PhysRevE.53.6336.

Gkinis, V., S. Simonsen, S. Buchardt, J. White, and B. Vinther (2014). Water isotope diffusion rates from the NorthGRIP ice core for the last 16,000 years – Glaciological and paleoclimatic implications. *Earth and Planetary Science Letters*, 405, 132 –141. DOI: 10.1016/j.epsl.2014.08.022.

Goswami, B., J. Heitzig, K. Rehfeld, N. Marwan, A. Anoop, S. Prasad, and J. Kurths (2014). Estimation of sedimentary proxy records together with associated uncertainty. *Nonlinear Processes in Geophysics*, 21 (6), 1093–1111. DOI: 10.5194/npg-21-1093-2014.

Goswami, B., N. Boers, A. Rheinwalt, N. Marwan, J. Heitzig, S. F. M. Breitenbach, and J. Kurths (2018). Abrupt transitions in time series with uncertainties. *Nature Communications*, 9, 48. DOI: 10.1038/s41467-017-02456-6.

Grassberger, P. (1983). Generalized dimensions of strange attractors. *Physics Letters A*, 97 (6), 227 –230. DOI: 10.1016/0375-9601(83)90753-3.

Grassberger, P., T. Schreiber, and C. Schaffrath (1991). Nonlinear time sequence analysis. *International Journal of Bifurcation and Chaos*, 1, 521–547. DOI: 10.1142/S0218127491000403.

Hakim, G. J., J. Emile-Geay, E. J. Steig, D. Noone, D. M. Anderson, R. Tardif, N. Steiger, and W. A. Perkins (2016). The last millennium climate reanalysis project: Framework and first results. *Journal of Geophysical Research: Atmospheres*, 121 (12), 6745–6764. DOI: 10.1002/2016JD024751.

Hall, W. D. and H. R. Pruppacher (1976). The Survival of Ice Particles Falling from Cirrus Clouds in Subsaturated Air. *Journal of the Atmospheric Sciences*, 33 (10), 1995–2006. DOI: 10.1175/1520-0469(1976)033<1995:TSOIPF>2.0.CO;2.

Hartmann, D. L. (2016). *Global Physical Climatology (Second Edition)*. Second Edition. Boston: Elsevier. DOI: 10.1016/B978-0-12-328531-7.00021-9.

Hastie, T., R. Tibshirani, and J. Friedman (2001). *The Elements of Statistical Learning*. Springer Series in Statistics. New York, NY, USA: Springer New York Inc.

Hegger, R. and H. Kantz (1999). Improved false nearest neighbor method to detect determinism in time series data. *Phys. Rev. E*, 60, (4), 4970–4973. DOI: 10.1103/PhysRevE.60.4970.

Heitzig, J. (2013). Moving Taylor Bayesian Regression for Nonparametric Multidimensional Function Estimation with Possibly Correlated Errors. *SIAM Journal on Scientific Computing*, 35 (4), A1928–A1950. DOI: 10.1137/12087846X.

Hentschel, H. G. E. and I. Procaccia (1983). The infinite number of generalized dimensions of fractals and strange attractors. *Physica D: Nonlinear Phenomena*, 8 (3), 435 –444. DOI: 10.1016/0167-2789(83)90235-X.

Herron, M. M. and C. C. Langway (1980). Firn Densification: An Empirical Model. *Journal of Glaciology*, 25 (93), 373–385. DOI: 10.3189/S0022143000015239.

Hirata, Y. and K. Aihara (2017). Dimensionless embedding for nonlinear time series analysis. *Phys. Rev. E*, 96, (3), 032219. DOI: 10.1103/PhysRevE.96.032219.

Hochberg, Y. and Y. Benjamini (1990). More powerful procedures for multiple significance testing. *Statistics in medicine*, 9 (7), 811–818.

Holm, S. (1979). A Simple Sequentially Rejective Multiple Test Procedure. *Scandinavian Journal of Statistics*, 6 (2), 65–70.

Huang, J., H. M. van den Dool, and K. P. Georgarakos (1996). Analysis of Model-Calculated Soil Moisture over the United States (1931–1993) and Applications to

Long-Range Temperature Forecasts. *Journal of Climate*, 9 (6), 1350–1362. DOI: 10.1175/1520-0442(1996)009<1350:AOMCSM>2.0.CO;2.

Huang, N. E., Z. Shen, S. R. Long, M. C. Wu, H. H. Shih, Q. Zheng, N. Yen, C. C. Tung, and H. H. Liu (1998). The empirical mode decomposition and the Hilbert spectrum for nonlinear and non-stationary time series analysis. *Proceedings of the Royal Society of London. Series A: Mathematical, Physical and Engineering Sciences*, 454 (1971), 903–995. DOI: 10.1098/rspa.1998.0193.

Huerta, R., C. S. Cruz, J. R. Dorronsoro, and V. López (1995). Local State-Space Reconstruction Using Averaged Scalar Products of the Dynamical-System Flow Vectors. *Europhysics Letters*, 29 (1), 13–18. DOI: 10.1209/0295-5075/29/1/003.

Hughes, M. K. and H. F. Diaz (1994). Was there a 'medieval warm period', and if so, where and when? *Climatic Change*, 26 (2), 109–142. DOI: 10.1007/BF01092410.

Huke, J. P. and D. S. Broomhead (2007). Embedding theorems for non-uniformly sampled dynamical systems. *Nonlinearity*, 20 (9), 2205. DOI: 10.1088/0951-7715/20/9/011.

IPCC (2013). *Climate Change 2013 – The Physical Science Basis: Working Group I Contribution to the Fifth Assessment Report of the Intergovernmental Panel on Climate Change*. Cambridge University Press. DOI: 10.1017/CBO9781107415324.

Jacob, R., K. Harikrishnan, R. Misra, and G. Ambika (2018). Recurrence network measures for hypothesis testing using surrogate data: Application to black hole light curves. *Communications in Nonlinear Science and Numerical Simulation*, 54, 84 –99. DOI: 10.1016/j.cnsns.2017.05.018.

Jacob, R., K. P. Harikrishnan, R. Misra, and G. Ambika (2019). Weighted recurrence networks for the analysis of time-series data. *Proceedings of the Royal Society A: Mathematical, Physical and Engineering Sciences*, 475 (2221), 20180256. DOI: 10.1098/rspa.2018.0256.

Jacob, R., K. Harikrishnan, R. Misra, and G. Ambika (2016). Characterization of chaotic attractors under noise: A recurrence network perspective. *Communications in Nonlinear Science and Numerical Simulation*, 41, 32 –47. DOI: 10.1016/j.cnsns.2016.04.028.

Jaeger, H. and H. Haas (2004). Harnessing Nonlinearity: Predicting Chaotic Systems and Saving Energy in Wireless Communication. *Science*, 304 (5667), 78–80. DOI: 10.1126/science.1091277.

Johnsen, S. J., H. B. Clausen, K. M. Cuffey, G. Hoffmann, J. Schwander, and T. Creyts (2000). Diffusion of stable isotopes in polar firn and ice : the isotope effect in firn diffusion. *Physics of Ice Core Records*, 159, 121–140. DOI: 10.7916/D8KW5D4X.

Jouzel, J. (2013). A brief history of ice core science over the last 50 yr. *Climate of the Past*, 9 (6), 2525–2547. DOI: 10.5194/cp-9-2525-2013.

Judd, K. and A. Mees (1998). Embedding as a modeling problem. *Physica D: Nonlinear Phenomena*, 120, 273 –286. DOI: 10.1016/S0167-2789(98)00089-X.

Kantz, H. and T. Schreiber (2004). *Nonlinear time series analysis*. 2nd ed. Cambridge University Press.

Kennel, M. B. and H. D. I. Abarbanel (2002). False neighbors and false strands: A reliable minimum embedding dimension algorithm. *Phys. Rev. E*, 66, (2), 026209. DOI: 10.1103/PhysRevE.66.026209.

Kennel, M. B., R. Brown, and H. D. I. Abarbanel (1992). Determining embedding dimension for phase-space reconstruction using a geometrical construction. *Physical Review A*, 45, (6), 3403–3411. DOI: 10.1103/PhysRevA.45.3403.

Kraemer, K. H., R. V. Donner, J. Heitzig, and N. Marwan (2018). Recurrence threshold selection for obtaining robust recurrence characteristics in different embedding dimensions. *Chaos: An Interdisciplinary Journal of Nonlinear Science*, 28 (8), 085720. DOI: 10.1063/1.5024914.

Kugiumtzis, D (1996). State space reconstruction parameters in the analysis of chaotic time series — the role of the time window length. *Physica D: Nonlinear Phenomena*, 95 (1), 13 –28. DOI: 10.1016/0167-2789(96)00054-1.

Lacasa, L., A. Nuñez, É. Roldán, J. M. R. Parrondo, and B. Luque (2012). Time series irreversibility: a visibility graph approach. *The European Physical Journal B*, 85 (6), 217. DOI: 10.1140/epjb/e2012-20809-8.

Lachniet, M. S., J. P. Bernal, Y. Asmerom, V. Polyak, and D. Piperno (2012). A 2400 yr Mesoamerican rainfall reconstruction links climate and cultural change. *Geology*, 40 (3), 259–262. DOI: 10.1130/g32471.1.

Lachniet, M. S., Y. Asmerom, V. Polyak, and J. P. Bernal (2017). Two millennia of Mesoamerican monsoon variability driven by Pacific and Atlantic synergistic forcing. *Quaternary Science Reviews*, 155, 100 –113. DOI: 10.1016/j.quascirev.2016.11.012.

Lange, H. and S. Boese (2015). Recurrence Quantification and Recurrence Network Analysis of Global Photosynthetic Activity. In: *Recurrence Quantification Analysis: Theory and Best Practices*. Ed. by C. L. Webber Jr. and N. Marwan. Cham: Springer International Publishing, pp. 349–374. DOI: 10.1007/978-3-319-07155-8_12.

Lange, H., S. Sippel, and O. A. Rosso (2018). Nonlinear dynamics of river runoff elucidated by horizontal visibility graphs. *Chaos: An Interdisciplinary Journal of Nonlinear Science*, 28 (7), 075520. DOI: 10.1063/1.5026491.

Lechleitner, F. A., S. Amirnezhad-Mozhdehi, A. Columbu, L. Comas-Bru, I. Labuhn, C. Pérez-Mejías, and K. Rehfeld (2018). The Potential of Speleothems from Western Europe as Recorders of Regional Climate: A Critical Assessment of the SISAL Database. *Quaternary*, 1 (3), DOI: 10.3390/quat1030030.

Letellier, C., J. Maquet, L. L. Sceller, G. Gouesbet, and L. A. Aguirre (1998). On the non-equivalence of observables in phase-space reconstructions from recorded time series. *Journal of Physics A: Mathematical and General*, 31 (39), 7913–7927. DOI: 10.1088/0305-4470/31/39/008.

Letellier, C., L. A. Aguirre, and J. Maquet (2005). Relation between observability and differential embeddings for nonlinear dynamics. *Phys. Rev. E*, 71, (6), 066213. DOI: 10.1103/PhysRevE.71.066213.

Liebert, W. and H. Schuster (1989). Proper choice of the time delay for the analysis of chaotic time series. *Physics Letters A*, 142, 107 –111. DOI: 10.1016/0375-9601(89)90169-2.

Liebert, W., K. Pawelzik, and H. G. Schuster (1991). Optimal Embeddings of Chaotic Attractors from Topological Considerations. *Europhysics Letters*, 14 (6), 521–526. DOI: 10.1209/0295-5075/14/6/004.

Lorenz, E. N. (1963). Deterministic Nonperiodic Flow. *Journal of the Atmospheric Sciences*, 20 (2), 130–141. DOI: 10.1175/1520-0469(1963)020<0130:dnf>2.0.co;2.

Løvsletten, O. and M. Rypdal (2016). Statistics of Regional Surface Temperatures after 1900: Long-Range versus Short-Range Dependence and Significance of Warming Trends. *Journal of Climate*, 29 (11), 4057–4068. DOI: 10.1175/JCLI-D-15-0437.1.

Lu, Z., B. R. Hunt, and E. Ott (2018). Attractor reconstruction by machine learning. *Chaos: An Interdisciplinary Journal of Nonlinear Science*, 28 (6), 061104. DOI: 10.1063/1.5039508.

Lucarini, V., R. Blender, C. Herbert, F. Ragone, S. Pascale, and J. Wouters (2014). Mathematical and physical ideas for climate science. *Reviews of Geophysics*, 52 (4), 809–859. DOI: 10.1002/2013RG000446.

Luterbacher, J., J. P. Werner, J. E. Smerdon, L. Fernández-Donado, F. J. González-Rouco, D. Barriopedro, F. C. Ljungqvist, U. Büntgen, E. Zorita, S. Wagner, J. Esper, D. McCarroll, A. Toreti, D. Frank, J. H. Jungclaus, M. Barriendos, C. Bertolin, O. Bothe, R. Brázdil, D. Camuffo, P. Dobrovolný, M. Gagen, E. García-Bustamante, Q. Ge, J. J. Gómez-Navarro, J. Guiot, Z. Hao, G. C. Hegerl, K. Holmgren, V. V. Klimenko, J. Martín-Chivelet, C. Pfister, N. Roberts, A. Schindler, A. Schurer, O. Solomina, L. von Gunten, E. Wahl, H. Wanner, O. Wetter, E. Xoplaki, N. Yuan, D. Zanchettin, H. Zhang, and C. Zerefos (2016). European summer temperatures since Roman times. *Environmental Research Letters*, 11 (2), 024001. DOI: 10.1088/1748-9326/11/2/024001.

Mañé, R. (1981). On the dimension of the compact invariant sets of certain non-linear maps. *Lecture Notes in Mathematics, Berlin Springer Verlag*, 898, 230. DOI: 10.1007/BFb0091916.

Mann, M. E. (2007). PALEOCLIMATE RECONSTRUCTION | The Last Millennium. In: *Encyclopedia of Quaternary Science*. Ed. by S. A. Elias. Oxford: Elsevier, pp. 1993 –2002. DOI: 10.1016/B0-44-452747-8/00031-4.

Mann, M. E., Z. Zhang, S. Rutherford, R. S. Bradley, M. K. Hughes, D. Shindell, C. Ammann, G. Faluvegi, and F. Ni (2009). Global Signatures and Dynamical Origins of the Little Ice Age and Medieval Climate Anomaly. *Science*, 326 (5957), 1256–1260. DOI: 10.1126/science.1177303.

Maraun, D., J. Kurths, and M. Holschneider (2007). Nonstationary Gaussian processes in wavelet domain: Synthesis, estimation, and significance testing. *Phys. Rev. E*, 75, (1), 016707. DOI: 10.1103/PhysRevE.75.016707.

Marwan, N., N. Wessel, U. Meyerfeldt, A. Schirdewan, and J. Kurths (2002). Recurrence-plot-based measures of complexity and their application to heart-rate-variability data. *Phys. Rev. E*, 66, (2), 026702. DOI: 10.1103/PhysRevE.66.026702.

Marwan, N., M. H. Trauth, M. Vuille, and J. Kurths (2003). Comparing modern and Pleistocene ENSO-like influences in NW Argentina using nonlinear time series

analysis methods. *Climate Dynamics*, 21 (3-4), 317–326. DOI: 10.1007/s00382-003-0335-3.

Marwan, N., M. C. Romano, M. Thiel, and J. Kurths (2007). Recurrence plots for the analysis of complex systems. *Physics Reports*, 438 (5-6), 237–329. DOI: 10.1016/j.physrep.2006.11.001.

Marwan, N., J. F. Donges, Y. Zou, R. V. Donner, and J. Kurths (2009). Complex network approach for recurrence analysis of time series. *Physics Letters A*, 373 (46), 4246–4254. DOI: 10.1016/j.physleta.2009.09.042.

Miller, R. G. J. (1981). *Simultaneous Statistical Inference*. 2nd. Springer-Verlag New York. DOI: 10.1007/978-1-4613-8122-8.

Mindlin, G. M. and R. Gilmore (1992). Topological analysis and synthesis of chaotic time series. *Physica D: Nonlinear Phenomena*, 58 (1), 229 –242. DOI: 10.1016/0167-2789(92)90111-Y.

Moy, C. M., G. O. Seltzer, D. T. Rodbell, and D. M. Anderson (2002). Variability of El Niño/Southern Oscillation activity at millennial timescales during the Holocene epoch. *Nature*, 420, 162. DOI: 10.1038/nature01194.

Neukom, R., L. A. Barboza, M. P. Erb, F. Shi, J. Emile-Geay, M. N. Evans, J. Franke, D. S. Kaufman, L. Lücke, K. Rehfeld, A. Schurer, F. Zhu, S. Brönnimann, G. J. Hakim, B. J. Henley, F. C. Ljungqvist, N. McKay, V. Valler, L. von Gunten, and P. A.G.E. S. 2k Consortium (2019). Consistent multidecadal variability in global temperature reconstructions and simulations over the Common Era. *Nature Geoscience*, 12 (8), 643–649. DOI: 10.1038/s41561-019-0400-0.

Newman, M. (2003). The Structure and Function of Complex Networks. *SIAM Review*, 45 (2), 167–256. DOI: 10.1137/S003614450342480.

Newman, M. (2010). *Networks: An Introduction*. Oxford University Press, Inc.

Newman, M. E. J. (2001). Scientific collaboration networks. I. Network construction and fundamental results. *Phys. Rev. E*, 64, (1), 016131. DOI: 10.1103/PhysRevE.64.016131.

Novello, V. F., M. Vuille, F. W. Cruz, N. M. Stríis, M. S. de Paula, R. L. Edwards, H. Cheng, I. Karmann, P. F. Jaqueto, and R. I. F. Trindade et al. (2016). Centennial-scale solar forcing of the South American Monsoon System recorded in stalagmites. *Scientific Reports*, 6, 24762. DOI: 10.1038/srep24762.

Oster, J. L., S. F. Warken, N. Sekhon, M. M. Arienzo, and M. Lachniet (2019). Speleothem Paleoclimatology for the Caribbean, Central America, and North America. *Quaternary*, 2 (1), DOI: 10.3390/quat2010005.

Østvand, L., T. Nilsen, K. Rypdal, D. Divine, and M. Rypdal (2014). Long-range memory in internal and forced dynamics of millennium-long climate model simulations. *Earth System Dynamics*, 5 (2), 295–308. DOI: 10.5194/esd-5-295-2014.

Packard, N. H., J. P. Crutchfield, J. D. Farmer, and R. S. Shaw (1980). Geometry from a Time Series. *Physical Review Letters*, 45 (9), 712–716. DOI: 10.1103/physrevlett.45.712.

PAGES2k-Consortium (2013). Continental-scale temperature variability during the past two millennia. *Nature Geoscience*, 6, 339. DOI: 10.1038/ngeo1797.

PAGES2k-Consortium (2017). A global multiproxy database for temperature reconstructions of the Common Era. *Scientific Data*, 4, 170088. DOI: 10.1038/sdata.2017.88.

Partin, J. W., T. M. Quinn, C.-C. Shen, J. Emile-Geay, F. W. Taylor, C. R. Maupin, K. Lin, C. S. Jackson, J. L. Banner, D. J. Sinclair, and C.-A. Huh (2013). Multidecadal rainfall variability in South Pacific Convergence Zone as revealed by stalagmite geochemistry. *Geology*, 41 (11), 1143–1146. DOI: 10.1130/G34718.1.

Pathak, J., Z. Lu, B. R. Hunt, M. Girvan, and E. Ott (2017). Using machine learning to replicate chaotic attractors and calculate Lyapunov exponents from data. *Chaos: An Interdisciplinary Journal of Nonlinear Science*, 27 (12), 121102. DOI: 10.1063/1.5010300.

Pecora, L. M., L. Moniz, J. Nichols, and T. L. Carroll (2007). A unified approach to attractor reconstruction. *Chaos: An Interdisciplinary Journal of Nonlinear Science*, 17 (1), 013110. DOI: 10.1063/1.2430294.

Pesin, Y. B. (1977). Characteristic Lyapunov exponents and smooth ergodic theory. *Russian Mathematical Surveys*, 32 (4), 55–114. DOI: 10.1070/rm1977v032n04abeh001639.

Poincaré, H. (1890). Sur la probleme des trois corps et les équations de la dynamique. *Acta Mathematica*, 13, 1–271.

Poland, D. (1993). Cooperative catalysis and chemical chaos: a chemical model for the Lorenz equations. *Physica D: Nonlinear Phenomena*, 65 (1), 86 –99. DOI: 10.1016/0167-2789(93)90006-M.

Portes, L. L., R. N. Benda, H. Ugrinowitsch, and L. A. Aguirre (2014). Impact of the recorded variable on recurrence quantification analysis of flows. *Physics Letters A*, 378 (32), 2382 –2388. DOI: 10.1016/j.physleta.2014.06.014.

Portes, L. L., A. N. Montanari, D. C. Correa, M. Small, and L. A. Aguirre (2019). The reliability of recurrence network analysis is influenced by the observability properties of the recorded time series. *Chaos: An Interdisciplinary Journal of Nonlinear Science*, 29 (8), 083101. DOI: 10.1063/1.5093197.

Radebach, A., R. V. Donner, J. Runge, J. F. Donges, and J. Kurths (2013). Disentangling different types of El Niño episodes by evolving climate network analysis. *Phys. Rev. E*, 88, (5), 052807. DOI: 10.1103/PhysRevE.88.052807.

Rehfeld, K. and J. Kurths (2014). Similarity estimators for irregular and age-uncertain time series. *Climate of the Past*, 10 (1), 107–122. DOI: 10.5194/cp-10-107-2014.

Rehfeld, K., N. Marwan, J. Heitzig, and J. Kurths (2011). Comparison of correlation analysis techniques for irregularly sampled time series. *Nonlinear Processes in Geophysics*, 18 (3), 389–404. DOI: 10.5194/npg-18-389-2011.

Rice, J. A. (2007). *Mathematical statistics and data analysis*. 3rd. Belmont, CA: Thomson/Brooks/Cole.

Rosenstein, M. T., J. J. Collins, and C. J. De Luca (1994). Reconstruction expansion as a geometry-based framework for choosing proper delay times. *Physica D: Nonlinear Phenomena*, 73 (1), 82 –98. DOI: 10.1016/0167-2789(94)90226-7.

Rössler, O. (1976). An equation for continuous chaos. *Physics Letters A*, 57 (5), 397 –398. DOI: 10.1016/0375-9601(76)90101-8.

Ruddiman, W. F. (2001). *Earth's Climate: Past and Future*. W. H. Freeman.

Runge, J., S. Bathiany, E. Bollt, G. Camps-Valls, D. Coumou, E. Deyle, C. Glymour, M. Kretschmer, M. D. Mahecha, J. Muñoz Marí, E. H. van Nes, J. Peters, R. Quax, M. Reichstein, M. Scheffer, B. Schölkopf, P. Spirtes, G. Sugihara, J. Sun, K. Zhang, and J. Zscheischler (2019). Inferring causation from time series in Earth system sciences. *Nature Communications*, 10 (1), 2553. DOI: 10.1038/s41467-019-10105-3.

Russell, J. M., E. C. Hopmans, S. E. Loomis, J. Liang, and J. S. S. Damsté (2018). Distributions of 5- and 6-methyl branched glycerol dialkyl glycerol tetraethers (brGDGTs) in East African lake sediment: Effects of temperature, pH, and new lacustrine paleotemperature calibrations. *Organic Geochemistry*, 117, 56 –69. DOI: 10.1016/j.orggeochem.2017.12.003.

Saltzman, B. (1962). Finite Amplitude Free Convection as an Initial Value Problem — I. *Journal of the Atmospheric Sciences*, 19 (4), 329–341. DOI: 10.1175/1520-0469(1962)019<0329:FAFCAA>2.0.CO;2.

Sauer, T. (1995). Interspike interval embedding of chaotic signals. *Chaos: An Interdisciplinary Journal of Nonlinear Science*, 5 (1), 127–132. DOI: 10.1063/1.166094.

Sauer, T., J. A. Yorke, and M. Casdagli (1991). Embedology. *Journal of Statistical Physics*, 65 (3), 579–616. DOI: 10.1007/BF01053745.

Sauer, T. (1994). Reconstruction of dynamical systems from interspike intervals. *Phys. Rev. Lett.*, 72, (24), 3811–3814. DOI: 10.1103/PhysRevLett.72.3811.

Scharnweber, T., K.-U. Heußner, M. Smiljanic, I. Heinrich, M. van der Maaten-Theunissen, E. van der Maaten, T. Struwe, A. Buras, and M. Wilmking (2019). Removing the no-analogue bias in modern accelerated tree growth leads to stronger medieval drought. *Scientific Reports*, 9 (1), 2509. DOI: 10.1038/s41598-019-39040-5.

Schneider, S. H. and M. D. Mastrandrea (2007). Paleoclimate relevance to global warming. In: *Encyclopedia of Quaternary Science*. Ed. by S. A. Elias. Oxford: Elsevier, pp. 2010 –2020. DOI: 10.1016/B0-44-452747-8/00020-X.

Schreiber, T. (1999). Interdisciplinary application of nonlinear time series methods. *Physics Reports*, 308 (1), 1 –64. DOI: 10.1016/S0370-1573(98)00035-0.

Schreiber, T. and A. Schmitz (1996). Improved Surrogate Data for Nonlinearity Tests. *Phys. Rev. Lett.*, 77, (4), 635–638. DOI: 10.1103/PhysRevLett.77.635.

Schreiber, T. and A. Schmitz (2000). Surrogate time series. *Physica D: Nonlinear Phenomena*, 142 (3), 346 –382. DOI: 10.1016/S0167-2789(00)00043-9.

Shannon, C. E. and W. Weaver (1949). *The Mathematical Theory of Communication*. University of Illinois Press.

Sigl, M., M. Winstrup, J. R. McConnell, K. C. Welten, G. Plunkett, F. Ludlow, U. Büntgen, M. Caffee, N. Chellman, D. Dahl-Jensen, H. Fischer, S. Kipfstuhl, C. Kostick, O. J. Maselli, F. Mekhaldi, R. Mulvaney, R. Muscheler, D. R. Pasteris, J. R. Pilcher, M. Salzer, S. Schüpbach, J. P. Steffensen, B. M. Vinther, and T. E. Woodruff (2015). Timing and climate forcing of volcanic eruptions for the past 2,500 years. *Nature*, 523, 543. DOI: 10.1038/nature14565.

Smith, S. W. (2003). *Digital Signal Processing*. Newnes. DOI: 10.1016/B978-0-7506-7444-7.X5036-5.

Sparrow, C. (1982). *The Lorenz Equations: Bifurcations, Chaos, and Strange Attractors*. New York: Springer. DOI: 10.1007/978-1-4612-5767-7.

St. George, S. (2014). An overview of tree-ring width records across the Northern Hemisphere. *Quaternary Science Reviews*, 95, 132 –150. DOI: 10.1016/j.quascirev.2014.04.029.

St. George, S. and J. Esper (2019). Concord and discord among Northern Hemisphere paleotemperature reconstructions from tree rings. *Quaternary Science Reviews*, 203, 278 –281. DOI: 10.1016/j.quascirev.2018.11.013.

Takens, F. (1980). Detecting strange attractors in turbulence. In: *Lecture Notes in Mathematics*. Springer Science and Business Media, pp. 366–381. DOI: 10.1007/bfb0091924.

Tardif, R., G. J. Hakim, W. A. Perkins, K. A. Horlick, M. P. Erb, J. Emile-Geay, D. M. Anderson, E. J. Steig, and D. Noone (2019). Last Millennium Reanalysis with an expanded proxy database and seasonal proxy modeling. *Climate of the Past*, 15 (4), 1251–1273. DOI: 10.5194/cp-15-1251-2019.

Theiler, J. (1986). Spurious dimension from correlation algorithms applied to limited time-series data. *Phys. Rev. A*, 34, (3), 2427–2432. DOI: 10.1103/PhysRevA.34.2427.

Theiler, J., S. Eubank, A. Longtin, B. Galdrikian, and J. D. Farmer (1992). Testing for nonlinearity in time series: the method of surrogate data. *Physica D: Nonlinear Phenomena*, 58 (1), 77 –94. DOI: 10.1016/0167-2789(92)90102-S.

Thiel, M., M. C. Romano, J. Kurths, M. Rolfs, and R. Kliegl (2006). Twin surrogates to test for complex synchronisation. *Europhysics Letters (EPL)*, 75 (4), 535–541. DOI: 10.1209/epl/i2006-10147-0.

Thompson, L. G., M. E. Davis, E. Mosley-Thompson, P.-N. Lin, K. A. Henderson, and T. A. Mashiotta (2005). Tropical ice core records: evidence for asynchronous glaciation on Milankovitch timescales. *Journal of Quaternary Science*, 20 (7-8), 723–733. DOI: 10.1002/jqs.972.

Thompson, L. G., E. Mosley-Thompson, M. E. Davis, V. S. Zagorodnov, I. M. Howat, V. N. Mikhalenko, and P.-N. Lin (2013). Annually Resolved Ice Core Records of Tropical Climate Variability over the Past ∼1800 Years. *Science*, 340 (6135), 945–950. DOI: 10.1126/science.1234210.

Tolwinski-Ward, S. E., M. N. Evans, M. K. Hughes, and K. J. Anchukaitis (2011). An efficient forward model of the climate controls on interannual variation in tree-ring width. *Climate Dynamics*, 36 (11), 2419–2439. DOI: 10.1007/s00382-010-0945-5.

Tolwinski-Ward, S. E., K. J. Anchukaitis, and M. N. Evans (2013). Bayesian parameter estimation and interpretation for an intermediate model of tree-ring width. *Climate of the Past*, 9 (4), 1481–1493. DOI: 10.5194/cp-9-1481-2013.

Torrence, C. and G. P. Compo (1998). A Practical Guide to Wavelet Analysis. *Bulletin of the American Meteorological Society*, 79 (1), 61–78. DOI: 10.1175/1520-0477(1998)079<0061:APGTWA>2.0.CO;2.

Trauth, M. H. (2013). TURBO2: A MATLAB simulation to study the effects of bioturbation on paleoceanographic time series. *Computers & Geosciences*, 61, 1–10. DOI: 10.1016/j.cageo.2013.05.003.

Trauth, M. H., A. Asrat, W. Duesing, V. Foerster, K. H. Kraemer, N. Marwan, M. A. Maslin, and F. Schaebitz (2019). Classifying past climate change in the Chew Bahir basin, southern Ethiopia, using recurrence quantification analysis. *Climate Dynamics*, DOI: 10.1007/s00382-019-04641-3.

Tsonis, A. A., K. L. Swanson, and P. J. Roebber (2006). What Do Networks Have to Do with Climate? *Bulletin of the American Meteorological Society*, 87 (5), 585–596. DOI: 10.1175/BAMS-87-5-585.

Vaganov, E. A., M. K. Hughes, and A. V. Shashkin (2006). *Growth Dynamics of Conifer Tree Rings*. 1st ed. Springer-Verlag Berlin Heidelberg. DOI: 10.1007/3-540-31298-6.

Villalba, R., M. Grosjean, and T. Kiefer (2009). Long-term multi-proxy climate reconstructions and dynamics in South America (LOTRED-SA): State of the art and perspectives. *Palaeogeography, Palaeoclimatology, Palaeoecology*, 281 (3-4), 175—179. DOI: 10.1016/j.palaeo.2009.08.007.

Vimeux, F., P. Ginot, M. Schwikowski, M. Vuille, G. Hoffmann, L. G. Thompson, and U. Schotterer (2009). Climate variability during the last 1000 years inferred from Andean ice cores: A review of methodology and recent results. *Palaeogeography, Palaeoclimatology, Palaeoecology*, 281 (3-4), 229—241. DOI: 10.1016/j.palaeo.2008.03.054.

Vlachos, I. and D. Kugiumtzis (2009). State Space Reconstruction from Multiple Time Series. In: *Topics on Chaotic Systems*, pp. 378–387. DOI: 10.1142/9789814271349_0043.

von Storch, H. and F. W. Zwiers (1999). *Statistical Analysis in Climate Research*. Cambridge University Press. DOI: 10.1017/CBO9780511612336.

Vuille, M., R. S. Bradley, R. Healy, M. Werner, D. R. Hardy, L. G. Thompson, and F. Keimig (2003). Modeling δ18O in precipitation over the tropical Americas: 2. Simulation of the stable isotope signal in Andean ice cores. *Journal of Geophysical Research: Atmospheres*, 108 (D6), DOI: 10.1029/2001JD002039.

Vuille, M., S. J. Burns, B. L. Taylor, F. W. Cruz, B. W. Bird, M. B. Abbott, L. C. Kanner, H. Cheng, and V. F. Novello (2012). A review of the South American monsoon history as recorded in stable isotopic proxies over the past two millennia. *Climate of the Past*, 8 (4), 1309–1321. DOI: 10.5194/cp-8-1309-2012.

Wackerbarth, A., D. Scholz, J. Fohlmeister, and A. Mangini (2010). Modelling the δ^{18}O value of cave drip water and speleothem calcite. *Earth and Planetary Science Letters*, 299 (3), 387 –397. DOI: 10.1016/j.epsl.2010.09.019.

Wang, Y., H. Cheng, R. L. Edwards, Y. He, X. Kong, Z. An, J Wu, M. J. Kelly, C. A. Dykoski, and X. Li (2005). The Holocene Asian Monsoon: Links to Solar Changes and North Atlantic Climate. *Science*, 308 (5723), 854–857. DOI: 10.1126/science.1106296.

Watts, D. J. and S. H. Strogatz (1998). Collective dynamics of 'small-world' networks. *Nature*, 393 (6684), 440–442. DOI: 10.1038/30918.

Webber, C. L. and J. P. Zbilut (1994). Dynamical assessment of physiological systems and states using recurrence plot strategies. *Journal of Applied Physiology*, 76 (2), 965–973. DOI: 10.1152/jappl.1994.76.2.965.

Weijers, J. W., S. Schouten, J. C. van den Donker, E. C. Hopmans, and J. S. S. Damsté (2007). Environmental controls on bacterial tetraether membrane lipid distribution in soils. *Geochimica et Cosmochimica Acta*, 71 (3), 703 –713. DOI: 10.1016/j.gca.2006.10.003.

Welch, P. (1967). The use of fast Fourier transform for the estimation of power spectra: A method based on time averaging over short, modified periodograms. *IEEE Transactions on Audio and Electroacoustics*, 15 (2), 70–73. DOI: 10.1109/TAU.1967.1161901.

Westfall, P. H. and S. S. Young (1993). *Resampling-based multiple testing: Examples and methods for p-value adjustment*. Vol. 279. John Wiley & Sons.

Whitney, H. (1936). Differentiable Manifolds. *Annals of Mathematics*, 37 (3), 645–680. DOI: 10.2307/1968482.

Wiedermann, M., A. Radebach, J. F. Donges, J. Kurths, and R. V. Donner (2016). A climate network-based index to discriminate different types of El Niño and La Niña. *Geophysical Research Letters*, 43 (13), 7176–7185. DOI: 10.1002/2016GL069119.

Wiedermann, M., J. F. Donges, J. Kurths, and R. V. Donner (2017). Mapping and discrimination of networks in the complexity-entropy plane. *Phys. Rev. E*, 96, (4), 042304. DOI: 10.1103/PhysRevE.96.042304.

Wong, C. I. and D. O. Breecker (2015). Advancements in the use of speleothems as climate archives. *Quaternary Science Reviews*, 127, 1 –18. DOI: 10.1016/j.quascirev.2015.07.019.

Xiang, R., J. Zhang, X. Xu, and M. Small (2012). Multiscale characterization of recurrence-based phase space networks constructed from time series. *Chaos*, 22 (1), 013107. DOI: 10.1063/1.3673789.

Xu, X., J. Zhang, and M. Small (2008). Superfamily phenomena and motifs of networks induced from time series. *Proceedings of the National Academy of Sciences*, 105 (50), 19601—19605. DOI: 10.1073/pnas.0806082105.

Yarleque, C., M. Vuille, D. R. Hardy, O. E. Timm, J. De la Cruz, H. Ramos, and A. Rabatel (2018). Projections of the future disappearance of the Quelccaya Ice Cap in the Central Andes. *Scientific reports*, 8 (1), 15564–15564. DOI: 10.1038/s41598-018-33698-z.

Yi, G., J. Wang, H. Bian, C. Han, B. Deng, X. Wei, and H. Li (2013). Multiscale order recurrence quantification analysis of EEG signals evoked by manual acupuncture in healthy subjects. *Cognitive Neurodynamics*, 7 (1), 79–88. DOI: 10.1007/s11571-012-9221-1.

Yin, Y. and P. Shang (2016). Multiscale recurrence plot and recurrence quantification analysis for financial time series. *Nonlinear Dynamics*, 85 (4), 2309–2352. DOI: 10.1007/s11071-016-2830-1.

Zhang, R., Y. Zou, J. Zhou, Z. Gao, and S. Guan (2017). Visibility graph analysis for re-sampled time series from auto-regressive stochastic processes. *Communications*

in Nonlinear Science and Numerical Simulation, 42, 396 –403. DOI: 10.1016/j.cnsns.2016.04.031.

Zolitschka, B. and D. Enters (2009). Lacustrine Sediments. In: *Encyclopedia of Paleoclimatology and Ancient Environments*. Ed. by V. Gornitz. Springer Netherlands, pp. 486–488. DOI: 10.1007/978-1-4020-4411-3_120.

Zou, Y., R. V. Donner, N. Marwan, J. F. Donges, and J. Kurths (2019). Complex network approaches to nonlinear time series analysis. *Physics Reports*, 787, 1 –97. DOI: 10.1016/j.physrep.2018.10.005.

Zumbahlen, H. (2008). CHAPTER 8 - Analog Filters. In: *Linear Circuit Design Handbook*. Ed. by H. Zumbahlen. Newnes. DOI: 10.1016/B978-0-7506-8703-4.00008-0.

Selbständigkeitserklärung

Ich erkläre, dass ich die Dissertation selbständig und nur unter Verwendung der von mir gemäß § 7 Abs. 3 der Promotionsordnung der Mathematisch-Naturwissenschaftlichen Fakultät, veröffentlicht im Amtlichen Mitteilungsblatt der Humboldt-Universität zu Berlin Nr. 42/2018 am 11.07.2018 angegebenen Hilfsmittel angefertigt habe.

Ich habe mich nicht anderwärts um einen Doktorgrad im Promotionsfach Physik beworben und besitze keinen Doktorgrad im Promotionsfach Physik.

Die Promotionsordnung der Mathematisch-Naturwissenschaftlichen Fakultät, veröffentlicht im Amtlichen Mitteilungsblatt der Humboldt-Universität zu Berlin Nr. 42/2018 am 11.07.2018, habe ich zur Kenntnis genommen.

Berlin, den 12. August 2019

Jaqueline Lekscha